Universitat Politècnica de Catalunya
Departament de Física

Population Synthesis Studies of the White Dwarfs of the Galactic Disk and Halo

by

Elena-Ruxandra Cojocaru

A thesis submitted for the degree of Doctor of Philosophy

Advisors:
Santiago Torres Gil
Enrique García–Berro Montilla

Castelldefels, September 2016

Dedicated to my teachers

Over there, the old magister, in his shabby, tattered coat,
Draws an endless calculation whose result remains remote,
And he buttons up his old gown trembling in the winter freeze,
Stuffs his neck into the collar, plugs the cotton in his ears;
There he is, gaunt, bent and hunched, but for better or for worse,
He's the undisputed master of the boundless universe
For the past merges the future right below his thinking brows,
Same as Atlas on his shoulder held the sky's immensity,
Such he poises on one number both world and eternity.

Mihai Eminescu - "First Letter",
translated by Ştefan Ichim

Acknowledgments

I knew I wanted to become a Physicist even before turning 14 and managed to stubbornly hold on to that idea ever since. In my third year of college I read a good book on Computational Physics written by N. J. Giordano and H. Nakanishi, from which I especially liked the chapter on Monte Carlo methods (true story) and thought that that would be a nice field to work in. Some months later, while visiting the planetarium in Torun, Poland, I decided that I should apply my new found interest in Computational Physics to Astrophysics. And that was that. Some years later, these fated (or maybe just random) decisions brought me to the door of Dr. Santiago Torres, who had become my supervisor during the Master just because the person who initially was supposed to fulfill this role could not. I told Santi that I was considering pursuing a PhD in Computational Astrophysics and two months later he arranged an interview with Prof. Enrique García-Berro. The following autumn I finally started my PhD and here I am. I cannot say it has been an easy road, I have been frustrated and plagued by apocalyptic visions many a time, but in the end it turned out far better than I could have expected. I know that I owe this mostly to my supervisors. The two of them make a great team, and as any good parents, they complement and compensate each other. I thank them for giving me the change to pursue my doctoral studies (with a grant!!), for introducing me to white dwarfs which are a fun subject, for sending me on several very fulfilling trips abroad and for taking me to two White Dwarf Workshops (an experience I would recommend to any student working on this topic). I also thank them for being patient and understanding, for giving me direction and cohesion (Heaven knows I needed it), and for teaching me many many things.

Two years into my PhD, I was offered to opportunity to go to China. I must now confess that I was more than skeptical about the idea, but... I was wrong! In the end it was one of the best experiences of my life. I owe it mostly to Dr. Alberto Rebassa-Mansergas, who was the one that made my short stay at the Kavli Institute possible. If I could add a third supervisor to my thesis, it would undoubtedly be him. I am sure that he will oversee many PhD students throughout his career and they will be lucky to have him. I have great respect and appreciation for Alberto and I am grateful for all our collaborations ever since. I would also like to thank some people I met while in China: Nahiely – for making me feel welcome from the very first moment – Yohai – for being my dear friend, and my office-mates, Yang, Mao-Sheng and Beibei – with whom I had lots of fun.

My next collaboration took me to Pittsburgh, in the US. This was possible thanks to Dr. Carles Badenes, who was an excellent host. I have to apologize him for not finishing (yet) the work we started there, however I hope it will soon see the light

of day. Even so, many of the things that I learned while in Pittsburgh have been useful in writting this thesis so, once again, thank you! I would also like to express my deep gratitude to Dr. Walter Goldburg and his late wife, Helen, for receiving me into their home during the time I spent in Pittsburgh. Prof. Goldburg was nothing short of an inspiration to me and I have enjoyed the many hours spent talking with him. Last but not least, from my American adventure I would also like to thank Lori Neu and Héctor, for being my friends, then and ever since.

And, believe it or not, I was lucky enough to even get to spend a week in Israel, visiting the Technion. Although short, I really enjoyed my time there and would like to thank my host, Dr. Hagai Perets, to whom I also owe some apologies, for yet another (currently) unfinished project.

PhDs are not only about writing articles or doing science, they have a truly dark side, know as paperwork. In this, I (and everybody else in my Department) have been very lucky, to have benefited from the help of our secretaries, Ana Ortega, Alicia Sanchez and Roser Pons, which are all great professionals. And I would also like to acknowledge the work of two modern day superheroes, Toni Castillo and Jordi Lino, who have saved both me and procyon (my computer) from the depths of despair on numerous occasions.

We have a wonderful department, filled with great people: Cesca – who taught me Fluid Mechanics – Jordi Mazon – who managed to make me believe that writing a PhD thesis in a decent amount of time was not an impossible feat – Enric, Pilar, Jordi Gutiérrez, Pere, Ricard, David, Arcadi, Joan Soler – I think I have shared teaching duties with almost all of you – and Dani Crespo, the head of our Department. I would also like to acknowledge my fellow PhD students, with whom I have shared many things during these four years here: Estel – who almost adopted me – Gabriela – who accompanied me in my Astrophysical joys and woes – Anna – who watered my plants like they where her babies – Milad – who makes the best black tea ever – Charlie – who is such a kind person – Isa – the author of my favorite cooling tracks – Fuqiang – who taught me how to count in Chinese – Araceli – with whom I went to the Gym – Judit – from whom I inherited the binary code – Fran – who will forever be a PhD student in my heart – Enrique and Siddharth – with whom I spent my last year in the office – and the people that have been with us for a shorter (but still enjoyable) time: Mitra, Joan Brahamcha, Joel, Coco and María.

I don't know if you can tell everything about a person from looking at his or her friends, but I know that I have great friends. In Spain I met several wonderfull people: Jose, Ernest, Xavi, Edgar, Laura R. and Celia – sois todos magníficos y espero veros a todos antes de irme de Barcelona. And my life-long friends from back home are simply amazing, they have made 3,000 km and at times 10,000 km seem much less than it had any right to: Lauri, Juli, Elena, Cătă, TC, Ana, Alex, Adriana, Oana, Cezar, Magda, Silvia - vă iubesc pe absolut toţi!

I would like to thank my family for their constant support – my parents, who taught me right from wrong and then always allowed me to choose – and my sister,

who has manned the fort ever since I decided to go gallivanting about the world. I would also like to thank the person that has been by my side, holding my hand and weathering my Balkanic personality for six years now, Joan Polo.

I have dedicated this thesis to my teachers. I have had so many, I have been so lucky. They have all shaped me into who I am today, but I will mention just three more names: Jordi Aguilar, who was my boss when I worked as in intern at FME during my Master studies, a job where I learned a lot and that I really enjoyed, mostly thanks to his help and guidance. Dr. Mona Mihăilescu, the professor with whom I did my undergraduate project, the person who truly introduced me to research and who has been a great support ever since. And my highschool Mathematics teacher, Mr. Mihai Bălună, one of the people I respect most in this world and also the person who I believe has had the greatest influence over my way of thinking, especially when it comes to science.

As a Spanish joke says "errar es rumano" and I am very Romanian, so if I have forgotten somebody, I am truly sorry, but please do not hold it against me. I know that a PhD experience is very much influenced by the people you meet and interact with. If anybody else decides to embark on such an adventure, I wish them to be at least as fortunate as I was.

The work presented in this thesis has been funded by the Spanish Ministry of Economy and Competitiveness (MINECO) through the FPI grant BES-2012-053448 and the mobility grants EEBB-I-14-08602 and EEBB-I-15-10054.

Contents

Outline and research target

White dwarfs are fossil stars that can encode valuable information about the formation, evolution and other properties of the different Galactic stellar populations. They are the direct descendants of main-sequence stars with masses ranging from $\sim 0.8\,M_{\odot}$ to $\sim 10\,M_{\odot}$, which means that over 95% of the stars in our Galaxy will eventually become white dwarfs. This fact, correlated with the excellent quality of modern white dwarf cooling models, clearly marks their potential as cosmic clocks for estimating the ages of Galactic stellar populations, as well as place white dwarfs as privileged objects in understanding several actual astrophysical problems.

Stellar population synthesis methods (Tinsley, 1968) use theoretical evolutionary sequences to reproduce luminosities, temperatures and other parameters building up to a synthetic population that can be readily compared to an observed sample of stars. Such techniques are perfect for the study of the different white dwarf populations in our Galaxy and their strength has only grown in recent years, fueled both by improved evolutionary sequences and detailed cooling tracks and also by the ever growing samples of white dwarfs identified through modern survey missions. In particular, the work presented in this thesis uses an updated population synthesis code based on previous versions of the code from our group (García-Berro et al., 1999; Torres et al., 2002; García-Berro et al., 2004; Torres et al., 2005; Camacho et al., 2014). Our synthetic population code, based on Monte Carlo statistical techniques, has been extensively used in the study of the disk (García-Berro et al., 1999; Torres et al., 2001; Torres & García-Berro, 2016) and halo (Torres et al., 2002; García-Berro et al., 2004) single white-dwarf population, white dwarf plus main sequence stars (Camacho et al., 2014) , as well as open clusters such as NGC 6791 (García-Berro et al., 2010; García-Berro et al., 2011) or globular clusters, as 47 Tuc (García-Berro et al., 2014).

In this thesis we investigate different properties of single and binary white dwarf populations in the Galactic disk and halo. We first study the effect of progenitor metallicity on the thin disk white dwarf luminosity function. Stellar metallicity is an important parameter in computing both main-sequence evolutionary sequences and white dwarf cooling tracks. At the same, studies of the metallicity distribution function for the Galactic disk have shown that both high and low-metallicity stars can be found throughout the entire mass range, although a clear dependence between

age and metallicity has yet to be proven and more recent findings actually show little correlation. With this in mind, we test two different age-metallicity relations, one assuming a Gaussian distribution of metallicity around the Solar value, the other one a decreasing relation between age and metallicity. We take into account the influence of metallicity on both main sequence lifetimes and white dwarf stellar parameters. Finally, we compute the theoretical white dwarf luminosity function applying the observational selection criteria of two different surveys, the Sloan Digital Sky Survey (SDSS) and the Supercosmos Sky Survey (SSS).

Next, we compute the white dwarf luminosity, mass and cumulative age functions derived from a sample of DA white dwarfs obtained from the LAMOST Spectroscopic Survey of the Galactic anti-center (LSS-GAC). We also derive the local space density and the formation rate for DA white dwarf. Given that both the observed mass distribution obtained from this sample and that derived from the local sample of white dwarfs present an apparent excess of massive white dwarfs, we investigate the possibility of accounting for this excess by reproducing the white dwarf population of the thin disk under different sets of initial assumptions, accounting also for selection criteria and observational biases.

Another issue that we investigate is the robustness of the halo white dwarf luminosity function employing different models for the initial mass function, density profile and stellar formation history. We also analyze if the white dwarf luminosity function can be used as a means to discriminate the role played by residual hydrogen burning in the atmospheres of low-mass white dwarfs. This process is known to become a significant source of energy for white dwarfs descending from very low-metallicity progenitors, such as those that characterize the Galactic halo population.

Lastly, we simulate the white dwarf-main sequence (WD+MS) binary population of the Galactic disk and compare it to the parameter distributions from the largest and most recent WD+MS catalog derived from the SDSS (Rebassa-Mansergas et al., 2016b). We not only reproduce the selection criteria, but we also account for spectroscopic completeness, observational errors and other biases that affect the sample. We use the observed population as a benchmark for constraining several important physical quantities specific to binary evolution, such as the initial mass ratio distribution and also the common envelope parametrization.

This thesis is based on three published papers, Cojocaru et al. (2014), Rebassa-Mansergas et al. (2015) and Cojocaru et al. (2015) and another work in preparation.

List of Figures

List of Tables

Chapter 1

Introduction: white dwarfs as galactic probes

1.1 The discovery of white dwarfs and early theoretical progress

The first white dwarf star ever discovered was 40 Eridani B, observed in 1783 by W. Herschel as part of a white dwarf-main sequence binary in a triple star system (Herschel, 1785). Next, Sirius B and Procyon B were discovered as unseen companions of much brighter main sequence stars in binary systems (Bessel, 1844).

Nearly a century later, it became evident that these objects were at the very least peculiar. In 1914, 40 Eridani B was determined to be of spectral type A0, which first seemed to be at odds with its dim apparent magnitude. When Russell (1914) released one of the first representation of a Hertzsprung-Russell (HR) diagram, containing over 200 objects, it was already apparent that 40 Eridani B was located in a completely different region in the diagram, in the lower left corner, as a consequence of its low luminosity and high temperature.

Soon after, in 1915, spectral measurements of Sirius B (Adams, 1915) showed it to be a hot, blue-white star, similar to 40 Eridani B, rather than cool and red as expected. In fact, using a temperature of $8,000\,\mathrm{K}$ based on an F0 spectral type (which he himself stated as a lower limit estimate) and a mass of $0.85\,M_{\odot}$ obtained from its orbital motion, Eddington (1926) computed that the radius of Sirius B was only three times that of our Earth, thus implying a very large density ($\sim 6 \times 10^4$ g/cm^3) and surface gravity ($\sim 3 \times 10^7$ cm/s^2). As a comment, present-day estimates of the temperature of Sirius B provide a value of $\sim 25,000$ K (Liebert et al., 2005b), yielding a much smaller radius of $0.0084\,R_{\odot}$ (Holberg et al., 1998) and an ever higher average density ($\sim 2.4 \times 10^6$ g/cm^3) and surface gravity ($\sim 4 \times 10^8$ cm/s^2).

These findings were initially considered suspicious, but soon came to be accepted, as more such objects were discovered. The term "white dwarf" was coined by Luyten

(1922), being later popularized by A. S. Eddington. By the 1950s, over a hundred white dwarfs were known (Luyten, 1950). By 1999, over 2,000 had been discovered (McCook & Sion, 1999) and, to date, the Sloan Digital Sky Survey (SDSS) has found over 19,000 white dwarf stars (Kleinman et al., 2013).

However, the enigma posed by the high density found for white dwarfs could not be unraveled immediately, not until the further development of quantum mechanics. Thus, white dwarfs became one of the first tests for quantum theory and proof for Pauli's exclusion principle: degenerate electrons being the source for internal pressure that holds a white dwarf together, preventing gravitational collapse (Fowler, 1926). Further studies by Anderson (1929), Chandrasekhar (1931), and Chandrasekhar (1933) provided an inverse relationship between white dwarf radius and mass, $R \sim M^{-1/3}$. This relation results in the existence of a limiting mass for non-rotating white dwarfs, known as the Chandrasekhar mass ($M_{\rm Ch} \approx 1.4 M_{\odot}$), at which gravitational forces surpass degenerate electron pressure and the star becomes unstable.

It was Mestel (1952) who presented the first accurate white dwarf cooling model, in which the white dwarf consists of an isothermal core of electron-degenerate matter (which represents more than 99% of the mass), surrounded by a very thin atmosphere composed of hydrogen and/or helium. The stored residual heat within the core is slowly released through a flux regulated by the atmospheric layers. Mestel's model was a good enough approximation for white dwarfs of intermediate luminosities ($L \sim 10^{-3}\, L_{\odot}$). Despite the fact that it required many improvements (see Section 1.2.4), it could be applied to a wide range of white dwarf temperatures.

Later that decade, Schmidt (1959) was the first to recognize that the coolest white dwarfs could help to constraint the age and stellar formation rate of the Galaxy, although the low number of detected white dwarfs at that time severely limited the effort. In the same way, Greenstein (1971) suggested that there is a discrepancy between the number of cool white dwarfs that were detected as compared to theoretical expectations. The Mestel cooling law predicts that the number of white dwarfs should rise monotonically as luminosity decreases. However, today we know that the scarcity of very cool white dwarfs is due to the finite age of the Galaxy, clearly indicating the potential of white dwarfs as cosmic clocks.

During the 80's the Palomar-Green Survey (Fleming et al., 1986) was used to cull a magnitude-limited sample of hot white dwarfs from which the hot end of the first estimate of the full white dwarf luminosity function (that is, the number density of white dwarfs as a function of their luminosity) was constructed (Winget et al., 1987; Liebert et al., 1988). The cooler white dwarfs that were used to compute the peak and cut-off for this luminosity function came from the Luyten Half-Second proper motioncatalog and the number counts were corrected for completeness corrected using the Schmidt's $1/V_{\rm max}$ estimator (Schmidt, 1968, 1975). After this, the white dwarf luminosity function (see also Section 1.5) proved to be a successful tool for the study of many of the properties of our Galaxy. In particular, white dwarfs have been

employed to estimate the ages of a variety of Galactic stellar populations, such as the Galactic disk (Winget et al., 1987; García-Berro et al., 1988) and halo (Mochkovitch et al., 1990; Isern et al., 1998) or the system of Galactic globular (Kalirai et al., 2001; Hansen et al., 2002, 2013) and open clusters – e.g., García-Berro et al. 2010 or Jeffery et al. 2011 – as well as its star formation history (Noh & Scalo, 1990; Diaz-Pinto et al., 1994; Isern et al., 1995).

1.2 General properties of white dwarfs

1.2.1 White dwarfs and stellar evolution

White dwarfs are the final evolutionary stage of low- and intermediate-mass main-sequence stars with masses up to $10 \pm 2\,M_{\odot}$ (Ritossa et al., 1999; Siess, 2007). For a lower limit to the progenitor mass, considering a 13.8 Gyr age for the universe (Planck Collaboration et al., in press 2016), it is easy to show that only single main-sequence stars with masses larger than $0.8M_{\odot}$ have had enough time to become white dwarfs, with a lower white dwarf mass limit of roughly $0.5M_{\odot}$ (for a more precise analysis of main-sequence lifetimes, one must also take into account stellar metallicity). However, when considering mass transfer in close-binary systems (see Section 1.3), this limit drops considerably, up to extremely low mass (ELM) white dwarfs, with masses $M_{\rm WD} < 0.25M_{\odot}$.

As previously mentioned, the generally accepted upper mass limit for non-rotating stable white dwarfs is the Chandrasekar mass, $M_{\rm Ch} =\sim 1.4M_{\odot}$. But, when considering rotating white dwarfs, the maximum mass value can increase to $1.48M_{\odot}$ for uniformly rotating stars (Anand, 1968). However, this limit depends on the distribution of angular momentum within the star and other issues related to the dynamical stability (Durisen, 1975). In this sense, some theoretical works claim that overluminous (peculiar) supernovae type Ia can be used to set a $\sim 2.58M_{\odot}$ upper mass limit to Super-Chandrasekar white dwarfs with very strong magnetic fields that accrete mass from their binary companions (Das & Mukhopadhyay, 2013).

From the evolutionary viewpoint, the progenitor of a typical (hydrogen-rich atmosphere, carbon-oxygen core) white dwarf star goes through a series of stages. First of all, the main sequence phase, in which central hydrogen is burned. The duration of this phase, that can be of the order of a few Gyr, is intimately related to the progenitor mass and metallicity. Afterwards, a red giant phase in which helium is burned in the core of the star, building the carbon-oxygen core of the future white dwarf. Once the helium core is practically exhausted, the star moves on to the asymptothic giant branch (AGB), which is characterized by unstable helium burning in the shell which leads to recurrent thermal instabilities (pulses). During this phase the mass of the core increases significantly, and most of the remaining hydrogen envelope is ejected through strong mas-loss episodes. A hydrogen envelope of $\sim 10^{-3}\,M_{\odot}$ is left, and the star forms a planetary nebulae. The central nucleus of the planetary

nebula is characterized by high luminosities and high effective temperatures. When the hydrogen envelope becomes smaller than $\sim 10^{-4}\,M_{\odot}$, nuclear energy generation practically ceases, surface luminosity rapidly decreases and the star begins its cooling process (slow radiation of stored gravothermal energy) as a white dwarf – for a more extended description, see Althaus et al. (2010a).

As later explained in Section 1.2.3, some white dwarf stars are hydrogen deficient, having nearly completely lost their outer hydrogen envelope. This is usually explained through the "born-again" scenario, which consists in the occurrence of one last, very late, helium thermal pulse, after hydrogen burning has almost ceased, as the star leaves the AGB and enters the cooling phase (Fujimoto, 1977; Iben et al., 1983; Althaus et al., 2005b). As a result, almost all the remaining hydrogen envelope is violently burned in an outward-expanding convection zone fueled by the helium flash (Herwig et al., 1999; Miller Bertolami et al., 2006).

1.2.2 The white dwarf mass distribution

The single white dwarf mass distribution (Liebert et al., 2005a; Kepler et al., 2007) can provide us with hints about white dwarf formation channels, core compositions and evolution. This distribution has three striking features (see Figure 1.1). The first and most obvious is the clear peak at $\sim 0.6\,M_{\odot}$ (Kepler et al., 2007), indicating that typical, carbon-oxygen white dwarfs cluster within a relatively narrow mass range, from 0.45 to $1.1\,M_{\odot}$.

The next noticeable feature of the mass distribution is a long tail extending towards high mass values. These are the descendants of more massive main sequence stars, with masses up to $8-10\,M_{\odot}$, which, due to the exponentially decreasing shape of the initial mass function (Kroupa, 2001), are far less numerous. The extreme region of this tail ($M_{\rm WD} > 1.1\,M_{\odot}$) is populated by white dwarfs with oxygen-neon (ONe) cores.

Lastly, one can also notice that the mass distribution also extends towards lower white dwarf mass values, up to $0.2-0.3\,M_{\odot}$, consisting of helium (He) core white dwarfs ($M_{\rm WD} < 0.45\,M_{\odot}$). It is unlikely that such low mass white dwarfs come from single stellar evolution, because that would need exceedingly large ages, incompatible with overall age estimates for stellar populations. Thus, most likely, such objects are the product of binary evolution. This is even more apparent when considering the mass distribution of white dwarfs that are part of post-common envelope binaries (PCEBs), where a secondary peak located at $\sim 0.4\,M_{\odot}$ can be clearly observed (Rebassa-Mansergas et al., 2011).

1.2.3 White dwarf atmospheres and spectroscopic classification

White dwarf atmospheres can be roughly divided into two categories: hydrogen-rich or hydrogen-deficient (helium dominated). Observations show that the vast

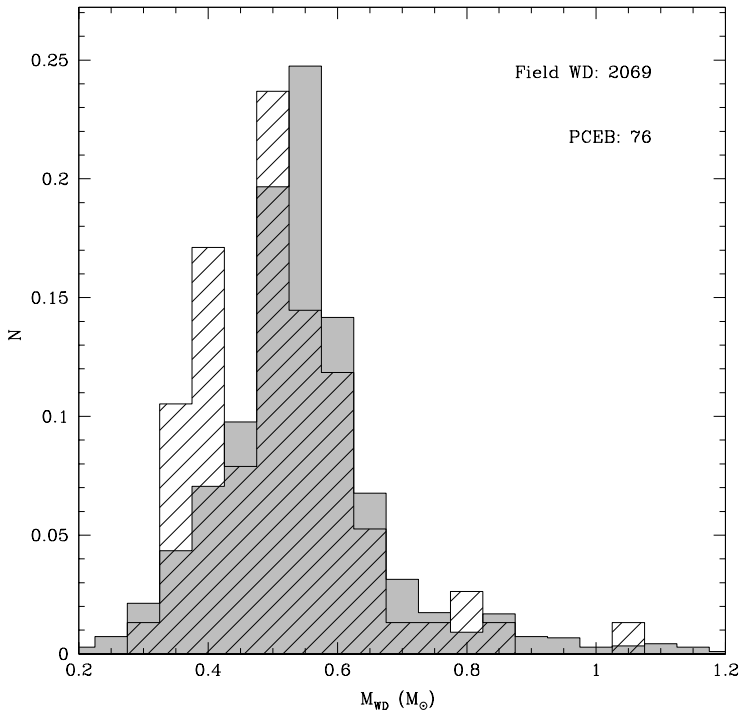

Figure 1.1: Normalized observational white dwarf mass distributions from Rebassa-Mansergas et al. (2011) for field white dwarfs – gray histogram – and for post common envelope binaries (PCEBs) – dashed histogram.

majority – $\sim$ 85% (Kleinman et al., 2013) – of white dwarfs have hydrogen atmospheres, of which $\sim$ 70% have pure hydrogen atmospheres (Koester et al., 2014). The reason for this is the strong gravitational field of white dwarfs. For this reason heavier elements sink to the bottom of the thin, but very opaque, visible layers. In the case of helium atmospheres, the outer hydrogen envelope has been lost, revealing the inner helium buffer. Still, more than one fourth of white dwarf stars show trace metals in their atmospheres. For hot white dwarfs, this can originate from the progenitor star in cases where gravitational levitation exceeds gravitational settling (Chayer et al., 1994; Barstow et al., 2003), or it can be a sign of binarity (heavy elements accreted from a companion during Roche love overflow or wind capture) or, for cool single white dwarfs, it can be attributed to contamination from the interstellar medium – namely gas, dust, and material accreted from disrupted asteroids or rocky planetesimals. For a detailed discussion of this issue see, e.g. Koester et al. (2005), Jura (2008), Dufour et al. (2010), and Farihi et al. (2010).

Sion et al. (1983) devised the current classification system of white dwarfs according to their spectral features. This classification is illustrated in Table 1.1 –

Primary class	Atmospheric and spectral characteristics, $T_{\rm eff}$ range
DA	H-rich; only Balmer lines, no He I or metals present
DB	H-deficient; He I (neutral) lines, no H; $11,000 - 30,000$ K
DO	H-deficient; strong He II (ionized) lines, He I or H present; $45,000 - 200,000$ K
DZ	Only metal lines, no H or He present; $< 11,000$ K
DQ	Carbon features (either atomic or molecular); $< 11,000$ K
DC	Continuous spectrum, no lines deeper than 5%; $< 11,000$ K
DX	Unclasifiable spectrum
Extended classes	
DAB	Mixed H-He; strong He I lines, weak H
DAO	Mixed H-He; H present, He II weak
DAZ	H-rich, metals present
DBZ	H-deficient, metals present
Additional symbols	
P	Magnetic white dwarfs with detectable polarization
H	Magnetic white dwarfs with no detectable polarization
E	Emission lines present
d	Debris disk
V	Optical symbol for variable stars
PEC	Spectral peculiarities

Table 1.1: Spectral classification system for white dwarf atmospheric content and spectral characteristics, including also effective temperature ranges; compiled from Sion et al. (1983); McCook & Sion (1999); Althaus et al. (2010a)

compiled from Sion et al. (1983), McCook & Sion (1999) and Althaus et al. (2010a) – which includes primary and extended spectral types for white dwarfs, along with some additional feature markers. All white dwarf spectral classes start with the uppercase letter D, which stands for degenerate star, followed by one or more letters. The first letter indicates the main spectral features and the following symbols indicate weaker features (extended spectral types) and/or additional attributes. Pure hydrogen atmosphere white dwarfs are DA type, whereas those with pure helium atmosphere are DB type for effective temperatures larger than $11,000$ K. Below this limit, helium-dominated atmosphere white dwarfs are divided between classes DC, DQ and DZ. The letter Z stands for trace metals detected in the spectrum, thus also resulting the extended classes DAZ and DBZ.

White dwarfs can be observed within a broad range of luminosities, from $10^{-5}\,L_{\odot}$ to $10^{3}\,L_{\odot}$ (Althaus et al., 2010a), and effective temperatures, from $4,000$ to $200,000$ K (Werner & Rauch, 2015). Although there is no strict correspondence between white dwarf spectra and effective temperature, interesting correlations exist, such as the

so called "DB gap" between 30,000 and 45,000 K and the "non-DA gap" between 5,000 and 6,000 K (Bergeron et al., 1997). The word "gap" here should not be interpreted as a complete lack of, but rather a relative scarcity of DB or non-DA objects in these ranges (Eisenstein et al., 2006b), especially given that Kleinman et al. (2013) do find several DB white dwarfs with effective temperatures above 30,000 K. They also showed that relatively hot ($T_{\rm eff} > 10,000$ K) DA and DB white dwarfs have a noticeably different distribution, with DBs mostly clustering between $12,000 - 18,000$ K whereas the number of DA white dwarfs just steadily decreases with temperature. Also, Tremblay & Bergeron (2008) showed that there is a relative increase in the ratio of non-DA over DA white dwarfs in the $6,000 - 10,000$ K range. These correlations can be seen as empiric arguments in favor of spectral evolution, given that the surface composition of the white dwarf may vary during its evolution as a result of convection, accretion, mass-loss episodes, radiative levitation, and gravitational settling (Althaus et al., 2010a).

Generally, stellar parameters (effective temperature, surface gravity, chemical abundances) are obtained either from spectroscopic or photometric measurements. This is done by comparing the observed and synthetic spectra. Such theoretical spectra are computed from a white dwarf model atmosphere by introducing a set of input element abundances, an effective temperature value and a s urface gravity. The model atmosphere is constructed based on a series of physical assumptions:

1) Homogeneous plane parallel layers. This is equivalent to considering the depth of the atmosphere to be much smaller than the radius of the star. Thus all matter quantities depend only on the height in radial direction.
2) Hydrostatic equilibrium, so the gradient of the gas pressure is in equilibrium with the gravitational attraction.
3) Radiative and convective equilibrium. This means that no energy is either produced or lost within the atmosphere. Thus, it only is transported from within the interior towards the atmosphere.
4) Local thermodynamic equilibrium (LTE). Equivalently, matter in each layer is considered to be in thermal equilibrium state corresponding to the local temperature of that layer. This assumption is not valid for hot and very hot stars, where non-LTE modelling being required for these cases, see Koester (2010) for further details.

1.2.4 Internal structure and cooling

A typical white dwarf star can be imagined as a stratified object, consisting of a dense core and two outer layers. The core contains most of the mass of the star and is usually composed of carbon and oxygen (CO), the end-products of He burning

(triple-α reaction). It is surrounded by a thin ($0.01\,M_{\odot}$) He-rich buffer and an even thinner outer H-rich envelope ($\sim 10^{-4}\,M_{\odot}$). The outer layers, although very thin, are very opaque, being crucial in regulating the release of gravothermal energy, and thus govern white dwarf cooling.

White dwarf cooling is a well understood and relatively simple process, which in a first approximation can be described by the Mestel law (Mestel, 1952). This model is based on the assumption that the core is an ideal fully degenerate gas, surrounded by a non-degenerate opaque radiative envelope. These assumptions are reasonable and, moreover, they are representative of the behavior of actual white dwarfs at intermediate luminosities. Better results can be obtained using modified Mestel cooling models, that take into account Coulomb interactions and Debye cooling (Shaviv & Kovetz, 1976), crystallization and chemical differentiation upon crystallization (Mochkovitch, 1983; Isern et al., 1997), or convection and mixing episodes (Fontaine et al., 2001). However, modern cooling sequences must tackle other sensitive issues. Among them are crucial the simultaneous treatment of thermal and hydrostatic evolution, implementing additional energy sources and sinks apart from thermal energy, non-isothermal treatment of the core (especially for hot white dwarfs), changes in chemical composition of the star during evolution due to convective mixing, radiative diffusion processes, residual nuclear reactions, and accretion – we refer to Althaus et al. (2010a) for an in depth discussion of all these issues.

The level of accuracy and sophistication of currently available cooling sequences has considerably improved during the last decade, and modern evolutionary sequences include a detailed treatment of atmospheres (Rohrmann et al., 2012), as well as an accurate treatment of all the sinks and sources of energy in the deep interior of white dwarfs (Isern et al., 1997, 2000). Here we mention neutrino emission, ^{22}Ne diffusion in the liquid phase (Isern et al., 1991; Althaus et al., 2010b), and phase separation of the carbon-oxygen binary mixture upon crystallization (Segretain et al., 1994). The high level of detail involved in modern cooling sequences is also worht emphasizing. Additionally, it should be also mentioned the excellent agreement between currently available cooling tracks computed using different stellar evolutionary codes, which is even better than that found when comparing between different main-sequence evolutionary sequences – for a detailed discussion on this topic, see Salaris et al. 2013, and for a practical example, see Cojocaru et al. 2014).

1.2.5 Metallicity

In astronomical terms metallicity (Z) refers to the fraction of a the mass of a star that is composed by elements other than hydrogen or helium, generalized as "metals". Thus, in terms of spectroscopy, the composition of a star can be defined by three parameters, X (the fraction of hydrogen), Y (the fraction of helium) and Z (the fraction of metals). In many cases, the overall metallicity cannot be measured directly, however observers can measure the iron-content of the star from iron emis-

sion lines, then employ models to estimate the total metallicity. The iron content of the star, [Fe/H], is defined relative to the Solar value as follows:

$$[\mathrm{Fe/H}] = \log_{10}\left(\frac{\mathrm{N_{Fe}}}{\mathrm{N_H}}\right)_{\mathrm{star}} - \log_{10}\left(\frac{\mathrm{N_{Fe}}}{\mathrm{N_H}}\right)_{\odot} \tag{1.1}$$

where N_{Fe} and N_{H} are the number of iron and hydrogen atoms per volume unit. This concept can be related to that of metallicity (Z) through the following equation (Tantalo & Chiosi, 2004):

$$[\mathrm{Fe/H}] = \log_{10}\left(\frac{\mathrm{Z_{star}}}{\mathrm{Z_{\odot}}}\right) - \log_{10}\left(\frac{\mathrm{X_{star}}}{\mathrm{X_{\odot}}}\right) - \Gamma \tag{1.2}$$

where the enhancement parameter Γ is assumed to be 0 for solar-scaled mixture. Besides, the second term is usually two orders of magnitude smaller than the first and hence negligible in a first approximation, the relationship can be simplified to:

$$Z = Z_{\odot} 10^{[\mathrm{Fe/H}]} \tag{1.3}$$

Our Sun has a metallicity $Z_{\odot} = 0.0134$ (Asplund et al., 2009) and $[\mathrm{Fe/H}]_{\odot} = 0$, whereas metal-poor stars have lower Z values and negative [Fe/H] and metal-rich stars have higher Z values and positive [Fe/H]. Several studies of main-sequence stars in both galactic and globular clusters have shown that metal-rich stars tend to be younger when compared to metal-poor stars (Carroll & Ostlie, 2007), thus suggesting the existence of an age-metallicity relationship (AMR). The classical works of Twarog (1980) and Meusinger et al. (1991) found a descending AMR as a function of the age for the galactic disk in the Solar vicinity. However, modern studies show an overall lack of correlation between age and metallicity and a large scatter (Casagrande et al., 2011; Haywood et al., 2013; Bergemann et al., 2014; Rebassa-Mansergas et al., in press 2016).

As previously discussed in Section 1.2.3, most white dwarf atmospheres do not have spectroscopic features of metals, because heavier elements sink below the atmosphere due to gravitational settling in a relatively short time span as compared to the lifetime of the star (for $T_{\mathrm{WD}} < 25,000\,\mathrm{K}$). Given the high opacity of the atmosphere, only the photosphere can be probed spectroscopically and the bulk metal content is difficult to measure. Because of this, it is hard to infer the progenitor metallicity directly from the white dwarf. However, when the white dwarf is a member of a white dwarf-main sequence binary, the white dwarf can provide accurate age estimates and the metallicity of the companion main sequence star can be measured, offering a new way to probe the AMR (Zhao et al., 2011; Rebassa-Mansergas et al., in press 2016).

Progenitor metallicity is a factor of paramount importance in white dwarf cooling. As shown by Isern et al. (1991), García-Berro et al. (2010) and Althaus et al. (2010b), the evolution of white dwarfs with high-metallicity progenitors is strongly modified by the energy released from ^{22}Ne sedimentation, which significantly delays their

cooling. Also, for white dwarfs with progenitors with low and very low metallicity, residual hydrogen burning can play an important role at $\sim 10^7 - 10^9$ yr in the cooling phase, whereas for white dwarfs resulting from Solar metallicity progenitors this process is almost negligible (Renedo et al., 2010; Miller Bertolami et al., 2013).

1.3 White dwarfs in binary systems

As previously explained in Section 1.2.2, white dwarfs with masses below $0.45\,M_{\odot}$ are thought to be helium-core white dwarfs, originating from progenitors that did not go through the core helium burning phase before losing their envelope (Althaus et al., 2001). Although Han et al. (1994) presents an alternative scenario to the formation of helium core white dwarfs from Population I progenitors that could eject their envelopes already on the first red giant branch, it is widely accepted today that helium-core white dwarfs are most likely the product of binary evolution, rather than being originated by single stellar evolution. This is due to the very long evolutionary timescales in the context of single stellar evolution (Laughlin et al., 1997). Also, there is now abundant evidence of low-mass white dwarfs that are found in close binary systems (Marsh et al., 1995; Liebert et al., 2005a; Rebassa-Mansergas et al., 2011), originating from a progenitor that has lost its envelope due to the interaction with a companion, most likely through common envelope evolution. On the other hand, several recent papers (Giammichele et al., 2012; Limoges et al., 2015; Rebassa-Mansergas et al., 2015) have reported a secondary peak in the (single) white dwarf mass distribution locate at higher masses ($0.8 - 1\,M_{\odot}$), and it has been suggested that this slight overabundance of high mass white dwarfs might originate from double degenerate mergers.

In wide binaries the white dwarf can form much in the same way as it would in single stellar evolution. This property can be exploited to determine the relation between the mass of the white dwarf and that of its progenitor star, which is called the initial-final mass relation (IFMR). The IMFR can also be obtained, for instance, in a semi-empirical way by using open star clusters, which allow to measure both the total age and the metallicity of the binary system present in the cluster (Williams et al., 2004; Kalirai et al., 2005). The stellar parameters (effective temperatures and surface gravities) of the white dwarfs are measured, then the white dwarf masses and cooling ages are inferred using white dwarf cooling tracks. Provided that the members of the binary system are coeval, the corresponding main-sequence lifetimes are obtained by subtracting the cooling time from the cluster age. Finally, the progenitor masses are computed by employing evolutionary models for main-sequence stars. Recent determinations of the IFMR are those of Catalán et al. (2008), Williams et al. (2009), Gesicki et al. (2014) (for the Galactic bulge) and Cummings et al. (2016).

By contrast, in close binaries at least one common envelope episode takes place. A common envelope (Paczynski, 1976; Iben & Livio, 1993; Webbink, 2008) event oc-

curs when the orbital separation between the two components of the binary quickly decreases when one of the stars expands rapidly. Mass transfer is initiated when the donor star fills it Roche lobe and overflows it, causing the orbit to further shrink, starting a process of dynamically unstable mass transfer. If the accretor cannot accept all the overflowing material, a common envelope is formed, engulfing the two components of the pair , that is both the core of the donor and the accreting star. As the binary spirals-in, its orbital energy (although other sources and sinks can be considered) is deposited in the envelope, leading to its expansion due to heating and eventually to its ejection or to a merger event. If the envelope is expelled, the remaining binary will have a significantly reduced orbital separation. This entire process is not very well understood, thus a simple parametrization is usually employed, and the free parameters are tuned to match observations. For an in depth discussion of the common envelope phase, we refer to Ivanova et al. (2013).

White dwarfs in close binaries are of great observational and theoretical interest. In particular, binaries consisting of a white dwarf with an M dwarf companion are relatively numerous and encode important information about the underlying properties of the galaxies or the subtleties of binary evolution (see Chapter 6), while binaries composed by a white dwarf and a F/G/K main sequence star or of two white dwarfs are candidates for the single and, respectively, double degenerate progenitor scenarios for type Ia supernovae – see Maoz et al. (2014) for a recent review.

1.4 The white dwarf populations in our Galaxy

Within the cold dark matter paradigm (Davis et al., 1985), the formation of the Milky Way can be understood as the result of hierarchical accretion (Kauffmann & Haehnelt, 2000), a process of continuous clustering and merging over billions of years that has determined the current shape and structure of our Galaxy. Consequently, different Galactic components can be identified, having formed at different stages of the accretion process. To keep this picture as simple as possible – see Haywood (2014); Bland-Hawthorn & Gerhard (2016) for a more complete description – most of the stellar mass in the Milky Way resides in a double (thin and thick) disk structure, with a bulge and bar at its center, surrounded by an extended dark spherical halo, also populated by globular clusters. As fossil stars, white dwarfs can be used to unravel important properties of the distinct Galactic populations. In this work we will focus on white dwarfs in the context of the Galactic disk and halo.

To obtain useful information from the different populations of white dwarfs, three conditions must be fulfilled. First, accurate observational data is needed. With the advent of large-scale automatic surveys, like the Sloan Digital Sky survey (Gunn et al., 1998) or the SuperCOSMOS Sky Survey (Rowell & Hambly, 2011), to cite just two representative examples, the sample of white dwarfs with reliable and accurate measurements of their astronomical properties has largely increased, thus allowing

for detailed comparisons with theoretical models. The second important ingredient to obtain useful information from the observed populations of Galactic white dwarfs is a set of accurate evolutionary cooling sequences (see Section 1.2.4). Finally, a tool to model the ensemble properties of these populations is also needed. For this, the best choice is a Monte Carlo simulator, a technique which is frequently used to model the different Galactic stellar populations, such as the Galactic disk white dwarfs, compensating for the poor statistics of the old observational samples at times (García-Berro et al., 1999, 2004) and allowing one to study the effects of biases and of the sample selection procedures (Geijo et al., 2006; Torres et al., 2007). The population synthesis code used in this thesis is described in more detail in Chapter 2.

1.4.1 Disk White Dwarfs

The Galactic disk can be separated into two populations, the thin and the thick disks (Gilmore & Reid, 1983). The thin disk has a smaller scale height $z_{\rm thin} = 300 \pm 50$ pc, a slightly larger scale length $R_{\rm thin} = 2.6 \pm 0.5$ kpc and contains most of the mass, $M_{\rm thin} = 4 \pm 1 \times 10^{10}\, M_{\odot}$, whilst the thick disk has $z_{\rm thick} = 900 \pm 180$ pc, $R_{\rm thick} = 2.0 \pm 0.2$ kpc and $M_{\rm thick} = 8 \pm 3 \times 10^{9}\, M_{\odot}$ – see Bland-Hawthorn & Gerhard (2016) and references therein. The thick disk is not only older and has a higher scale height when compared to the thin disk, but it also presents a different chemical signature (Bensby, 2014), that suggests a distinct origin. In terms of metallicity, it has been shown that thick disk stars have decreasing metallicity with increasing distance to the Galactic plan (Ivezić et al., 2008; Munn et al., 2004) and overall enhanced value of [α/Fe] (Haywood et al., 2015).

In the last decade, the increasing number of white dwarfs detected in magnitude- and proper motion-limited samples has led to increasingly accurate determinations of the disk white dwarf luminosity function (see Section 1.5). Harris et al. (2006) computed a white dwarf luminosity function for both the Galactic disk and halo from a large (over 6,000 stars) sample culled from the SDSS DR4 (Eisenstein et al., 2006a) with an overall completeness of $\sim 70\%$. The resulting function for the disk (see Figure 1.2) shows a smooth ascending bright branch with almost constant slope, and a steep drop-off at $M_{\rm bol} = 15.4$. De Gennaro et al. (2008) used the same sample to compute an observational luminosity function exclusively for disk DA white dwarfs, based on over 3,300 spectroscopically confirmed white dwarfs and with an overall completeness of $\sim 50\%$. Using data from the SuperCosmos Sky Survey (SSS) (Hambly et al., 2001) and Rowell & Hambly (2011) computed the white dwarf luminosity functions for the Galactic thin and thick disk population and also for the Galactic halo (see Section 1.4 and Fig.1.2), using a magnitude- and proper motion-limited sample consisting in total of $\sim 10,000$ white dwarfs with an overall completeness of $\sim 50\%$. This work also confirmed the position of the disk white dwarf luminosity function downturn near $M_{\rm bol} = 15.75$. Rowell (2013) used an algorithm for inverting the white dwarf luminosity function from the SSS sample to obtain an

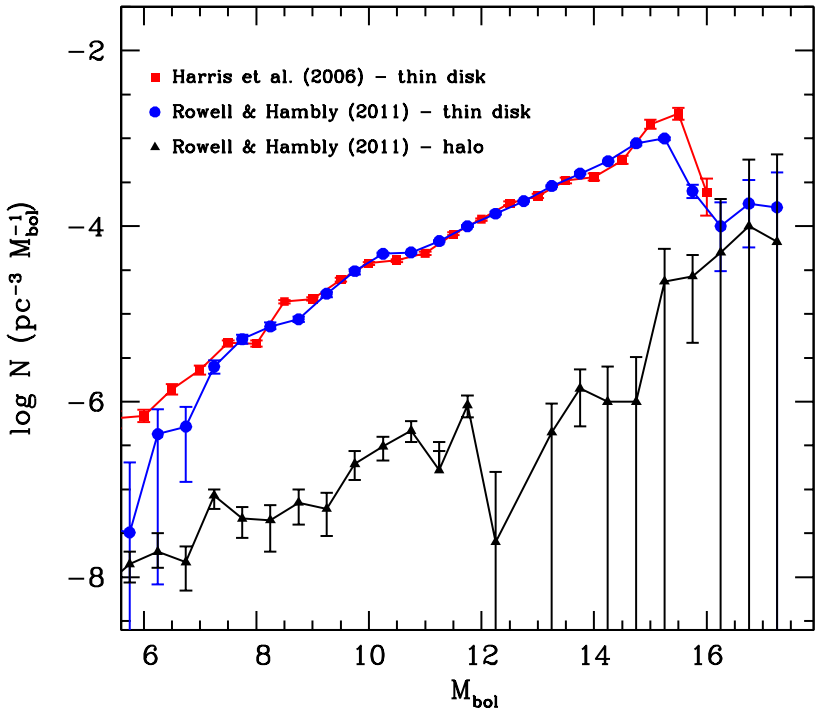

Figure 1.2: Observational white dwarf luminosity function for the thin disk of Harris et al. (2006) (red line and squares) and of Rowell & Hambly (2011) (blue line and circles). Also shown is a preliminary halo white dwarf luminosity function from Rowell & Hambly (2011) (black line and triangles).

estimate of the local star formation rate, finding a bimodal behavior, with broad peaks at $2-3$ Gyr and $7-9$ Gyr ago. Rebassa-Mansergas et al. (2015) presented a new DA white dwarf luminosity function identified in the LAMOST (Large Sky Area Multi-Object Fiber Spectroscopic Telescope) Spectroscopic Survey of the Galactic anticenter (LSS-GAC), see Liu et al. (2014), following a well-defined set of selection criteria in order to properly account for observational biases. However, Gentile Fusillo et al. (2015) showed that the white dwarf luminosity function obtained from this survey cannot be extended past the downturn due to the high incompleteness in the faintest bins.

Recently, several high-completeness volume-limited samples of white dwarfs in the close vicinity of the sun have been released (Sion et al., 2009; Giammichele et al., 2012; Holberg et al., 2015; Limoges et al., 2015). Sion et al. (2009) showed that virtually all the members of the 20 pc local white dwarf sample belong to the Galactic thin disk. Tremblay et al. (2014) derived the local star formation history using the 20 pc sample from Giammichele et al. (2012) and found evidence for an

enhancement of star formation in the past 5 Gyr, leading to an increase of the space density of white dwarfs of a factor of ~ 2.5. Sion et al. (2014) showed that for volume-limited samples, completeness is actually a function of distance, from $\sim 100\%$ at 13 pc to $\sim 60\%$ at 25 pc. Limoges et al. (2015) extended the local sample of white dwarfs to 40 pc, with almost 500 objects and claiming over 66% completeness. Torres & García-Berro (2016) simulated this 40 pc sample and estimated the overall completeness to be good, $\sim 80\%$, however also they also showed that for $M_{\rm bol} > 16$ completeness drops to 20%.

Finally, we mention that the ensemble properties of the population of Galactic disk white dwarfs have also been used to test theoretical scenarios and theories that cannot be probed yet in terrestrial laboratories. These include, for instance, testing alternative theories of gravitation, which result in a hypothetical variation of the gravitational constant (Garcia-Berro et al., 1995), setting constraints on the mass of weakly interacting particles like axions (Isern et al., 2008), or constraining the properties of the so-called dark forces (Dreiner et al., 2013). Additionally, the population of white dwarfs has also been used to derive interesting constraints on the local star-formation history (Noh & Scalo, 1990; Diaz-Pinto et al., 1994; Rowell, 2013).

1.4.2 Halo White Dwarfs

The stellar halo of the Milky Way consists of a structure of spherically distributed, high-velocity and low-metallicity stars, with large random motions and rotating slowly, which add up to about 1% of the Galaxy's total stellar mass (Bland-Hawthorn & Gerhard, 2016). The halo is considered to be the oldest Galactic component, and originally was thought to have formed when the Galaxy first collapsed (Eggen et al., 1962). However modern surveys show that the stellar halo has a complex structure with multiple components, and continues to accrete matter from smaller tidally disrupted galaxies (Ibata et al., 1997; Belokurov et al., 2006; Schlaufman et al., 2009), findings that are consistent with hierarchical galaxy formation models, as previously mentioned.

The population of white dwarfs in the Galactic stellar halo has been the subject of increased interest since the first observational and theoretical studies came to light (Mochkovitch et al., 1990; Liebert et al., 1989). Perhaps, one of the most important reasons for this interest in halo white dwarfs is their possible contribution to the dark matter content of our Galaxy; see, for instance, Kawaler (1996); Oppenheimer et al. (2001); Pauli et al. (2003) for observational works, and Torres et al. (2002); García-Berro et al. (2004) for theoretical studies. However, because of very low space densities and the intrinsic faintness of the population of white dwarfs in the Galactic spheroid, their detection has proven to be a difficult endeavor. Moreover, as opposed to what occurs with main-sequence stars, which can be classified according to their metallicity, the atmospheres of white dwarfs are devoid of metals. This

is because of their high surface gravities and long evolutionary timescales, which allow gravitational diffusion to be very efficient at settling the metals resulting from previous evolutionary history at the base of the partially degenerate envelope. All these physical processes make halo white dwarfs indistinguishable from disk white dwarfs. Hence, the only observational method for detecting white dwarfs belonging to the Galactic spheroid, which is not hampered by relevant technical difficulties, relies on identifying them on the basis of large proper motions, as radial velocities cannot be accurately determined. This is because of the large surface gravity, which translates into a sizable gravitational redshift of the spectral features that cannot be neglected, and it is difficult to measure. Additionally, the absence of spectral lines at the very low luminosities of the coldest halo white dwarfs also prevents an accurate characterization of the faintest members of this population. All this, in turn, considerably reduces the size of the observational sample, since at present large volumes cannot be probed, and we are limited to studying nearby halo white dwarfs.

Nevertheless, recent observational attempts to empirically determine the luminosity function of halo white dwarfs have been successful, and we now have a reliable sample of halo white dwarfs (Harris et al., 2006; Rowell & Hambly, 2011) to which the theoretical works can be compared. Comparing the results of the theoretical models with the available observed sample of halo white dwarfs is an important task (see Chapter 5), especially given that recently accurate cooling tracks for white dwarfs with very low-metallicity progenitors have become available (Miller Bertolami et al., 2013; Althaus et al., 2015). Finally, these kind of works are also of crucial importance to pave the road to future studies of the large population of halo white dwarfs, which the European astrometric mission Gaia will unveil in coming years (Torres et al., 2005).

1.5 The white dwarf luminosity function

The white dwarf luminosity function is a powerful astrophysical tool for exploring and constraining the properties of Galactic populations. It encloses information on star formation and extinction rates (Liebert et al., 2005a; Hu et al., 2007), it has been used to set constraints on the mass of local baryonic matter (Kawaler, 1996; Torres et al., 2002; Pauli et al., 2003; García-Berro et al., 2004), having also been successfully employed to obtain age estimates – starting with the classical works of Winget et al. (1987), García-Berro et al. (1988), and Mochkovitch et al. (1990) – and to explore the kinematics (Sion et al., 2009, 2014) of different stellar populations.

The white dwarf luminosity function is defined as the number of white dwarfs per cubic parsec as a function of unit luminosity (or bolometric magnitude). In particular, the white dwarf luminosity function of the the Galactic disk has been well studied (see Section 1.4.1 for details), drawing a clear picture on its shape and

underlying implications. Beginning with a bright and hot end at small bolometric magnitudes, the white dwarf luminosity function increases monotonically with decreasing luminosity, maintaining a nearly constant slope (which is intimately related to the white dwarf cooling mechanism), and upon reaching $M_{\rm bol} \sim 15$ it shows an abrupt downturn. This drop-off is a consequence of the finite age of the Galactic disk and is thus essential in age estimations. In fact, Fontaine et al. (2001) successfully coined the term "white dwarf cosmochronology" in a review focused on the importance of white dwarfs as cosmic clocks.

For the purpose of theoretical modeling, the white dwarf luminosity function can be mathematically formulated as follows – see the recent review García-Berro & Oswalt (2016) and references therein:

$$n(L) \propto \int_{M_{\rm i}}^{M_{\rm s}} \Psi(M)\phi\left(T - t_{\rm cool}(L,M) - t_{\rm MS}(M)\right)\tau_{\rm cool(L,M)}dM \tag{1.4}$$

where L is the luminosity, M is the mass of the white dwarf progenitor star, T is the age of the population under study, $t_{\rm cool}$ is the cooling time necessary to reach luminosity L for a white dwarf coming from a progenitor of mass M, $t_{\rm MS}$ is the main-sequence lifetime of the progenitor of mass M, Ψ is the initial mass function, ϕ is the star formation rate, $M_{\rm s} \simeq 10\,M_{\odot}$ is the maximum mass for a progenitor star to form a white dwarf, and $M_{\rm mi}$ is obtained from the following equation:

$$T = t_{\rm cool}(L, M_{\rm i}) + t_{\rm MS}(M_{\rm i}) \tag{1.5}$$

In order to obtain the white dwarf luminosity function, one must begin with a well-defined sample of white dwarfs. In this sense, three approaches exist. Magnitude-limited samples use color index criteria to identify likely white dwarf candidates, however they are biased towards identifying luminous stars up to larger distances as compared to intrinsically fainter stars. Proper motion-limited samples can isolate nearby white dwarfs based on their low luminosity, specific colors and high proper motions. However, they undercount distant fast-moving objects and also nearby slow-moving objects. Lastly, volume limited samples, which try to identify all white dwarfs within a certain distance from the Sun, offer potentially the most straightforward way to compute the white dwarf luminosity function. Unfortunately, these samples tend to be quite small and can also suffer from contamination of low main-sequence stars and sub-dwarfs. Currently available magnitude- and proper motion-limited samples can be quite large, however they require a weighting scheme in order to correct for the previously mentioned biases.

One such weighting scheme is known as Schmidt's estimator or the $1/V_{\rm max}$ method, introduced by Schmidt (1968) and generalized by Felten (1976). This estimator has been proven to be unbiased (Felten, 1976) if certain statistical conditions are fulfilled. Takeuchi et al. (2000) has shown that to obtain a good estimate of the luminosity function, the sample used should be both complete and homogeneous,

which again leads to the conclusion that to obtain a reliable white dwarf luminosity function, a well-understood observational sample is required. Also, the $1/V_{\rm max}$ method is known to underestimate the white dwarf density for moderately high luminosities, thus recovering the correct slope only for $\log(L/L_{\odot}) \gtrsim -2.2$. Equally important is that the position of the cut-off is sensitive to how data is binned, being more accurate for finer binning, but always located at larger luminosities (Geijo et al., 2006). Moreover, in the case of the Galactic disk, given that stars are not spherically distributed, an additionally correction must be implemented, taking into account the specific scale height of the disk (see Section 1.4.1). In Annex A we describe the standard procedure for using the $1/V_{\rm max}$ estimator and discuss in more detail the advantages and drawbacks that this method entails.

In summary, the quality of the resulting white dwarf luminosity function can be affected by many aspects related to the underlying white dwarf sample, such as sample size, completeness or contamination with other type of objects, for example unresolved double degenerates. We further discuss this topic and present the most relevant observational work done on the white dwarf luminosity function for the Galactic disk and halo in Sections 1.4.1 and 1.4.2. On the other hand, in a recent review by García-Berro & Oswalt (2016), the authors sum up what is currently necessary to substantially improve the observational white dwarf luminosity function. In particular, larger samples of white dwarfs (one or two order of magnitudes more than currently available ones), precise parallaxes and proper motions, high quality photometry at least up to $g \sim 21$ mag, higher resolution spectroscopic identifications, improved atmospheric models for very cool white dwarfs, improved spectral evolutionary models, a better treatment and understanding of selection effects and a quantification of the effects of unresolved binaries and high mass white dwarfs are needed.

Chapter 2

The population synthesis code

2.1 Basic principles

Stellar population synthesis is a general modeling procedure that consists of applying a wide set of laws, properties and models that, with the aid of several numerical methods and statistic tools, allows us to generate an artificial population of stars that can be directly compared with an observed sample. This not only implies using detailed models for each individual object, rather than ensemble properties, in order to follow its evolution. It also requires adequate modeling of stellar positions and kinematics, knowledge of the population formation history and chemical evolution, and last but not least, a good grasp of all the biases that affect the observed data. The population synthesis method has been employed in a wide series of contexts, from full Galaxy simulations (Robin et al., 2003), to more specific planetary formation scenarios (Ida & Lin, 2004; Benz et al., 2014) or the study of pre-main-sequence stars (Kroupa, 1995).

The work presented in this thesis uses an updated population synthesis code based on previous well known works (García-Berro et al., 1999; Torres et al., 2002; García-Berro et al., 2004; Torres et al., 2005; Camacho et al., 2014). The code has become a reference model in the simulation of the population of white dwarfs in a wide range of situations such as the study of the disk (García-Berro et al., 1999; Torres et al., 2001; Torres & García-Berro, 2016) and halo (Torres et al., 2002; García-Berro et al., 2004) single white-dwarf population, white dwarf plus main sequence stars (Camacho et al., 2014), as well as open clusters such as NGC 6791 (García-Berro et al., 2010; García-Berro et al., 2011) or globular clusters, like 47 Tuc (García-Berro et al., 2014). The code, based on Monte Carlo techniques, was designed to reproduce the white dwarf population either stemming from single stellar evolution or from binaries.

Fig. 2.1 shows a simplified flow-chart representation of the code, that highlights the key modules. These are, sampling the input parameters, single and binary stellar

evolution, the interpolation module for obtaining the white dwarf stellar parameters, the Galactic model that provides positions and kinematics and the filtering module that reproduces observational biases, helping in culling the final sample.

Any Monte Carlo code has at its very core the idea of repeated random sampling, being its main ingredient the pseudo-random number generator. We use the algorithm from James (1990), which produces a uniform probability density between $(0, 1)$ with a repetition period of over 10^{18}, which is virtually infinite for practical simulations. The next important step is using adequate probability distribution functions for sampling the stellar properties, i.e. generating the statistical properties of data from known distributions, that is used to obtain the initial characteristics (mass, time of birth, initial position, kinematics,...) of every star that will form part of the initial synthetic population. These distribution functions are crucial inputs that define each particular population. When Gaussian probability functions were needed, we used the Box-Muller algorithm as described in Press et al. (1986).

In order to achieve an statistical significance of the sample we require a large number of Monte Carlo realizations, typically of the order of $\sim 10^4$. We usually generate $50-100$ independent simulations and then expand this number using bootstrap techniques. For each quantity of interest, we present the ensemble average of the different Monte Carlo realizations, as well as the corresponding standard deviation.

2.2 Building the sample

For each Monte Carlo realization, we begin by sampling zero-age main sequence (ZAMS) stellar masses, M, using the initial mass function (IMF) of Kroupa (2001) and (Kroupa & Weidner, 2003), a composite power-law with a steeper slope for more massive stars:

$$\xi(M) = \begin{cases} M^{-1.3}, & 0.08 \leq M/M_{\odot} \leq 0.5 \\ M^{-2.3}, & 0.5 \leq M/M_{\odot} \leq 1.0 \\ M^{-2.7}, & M/M_{\odot} \geq 1.0 \end{cases} \tag{2.1}$$

This is a standard choice, in particular considering the alleged universal character of the IMF (Bastian et al., 2010).

Next, we use a star formation history (SFH) law to generate the moment at which each star is born and also assign a metallicity which can either be constant or sampled from an age-metallicity relation (AMR). After that, according to an assumed binary fraction ($f_{\rm bin}$), we decide if this is an individual star or it is the primary of a binary pair. It then follows either single (see Section 2.2.1) or binary stellar evolution (see Section 2.2.2). If the single star becomes a white dwarf or if one of the two components of the present-day binary is a white dwarf, we proceed to compute the stellar parameters and photometric magnitudes as described in Section 2.4.

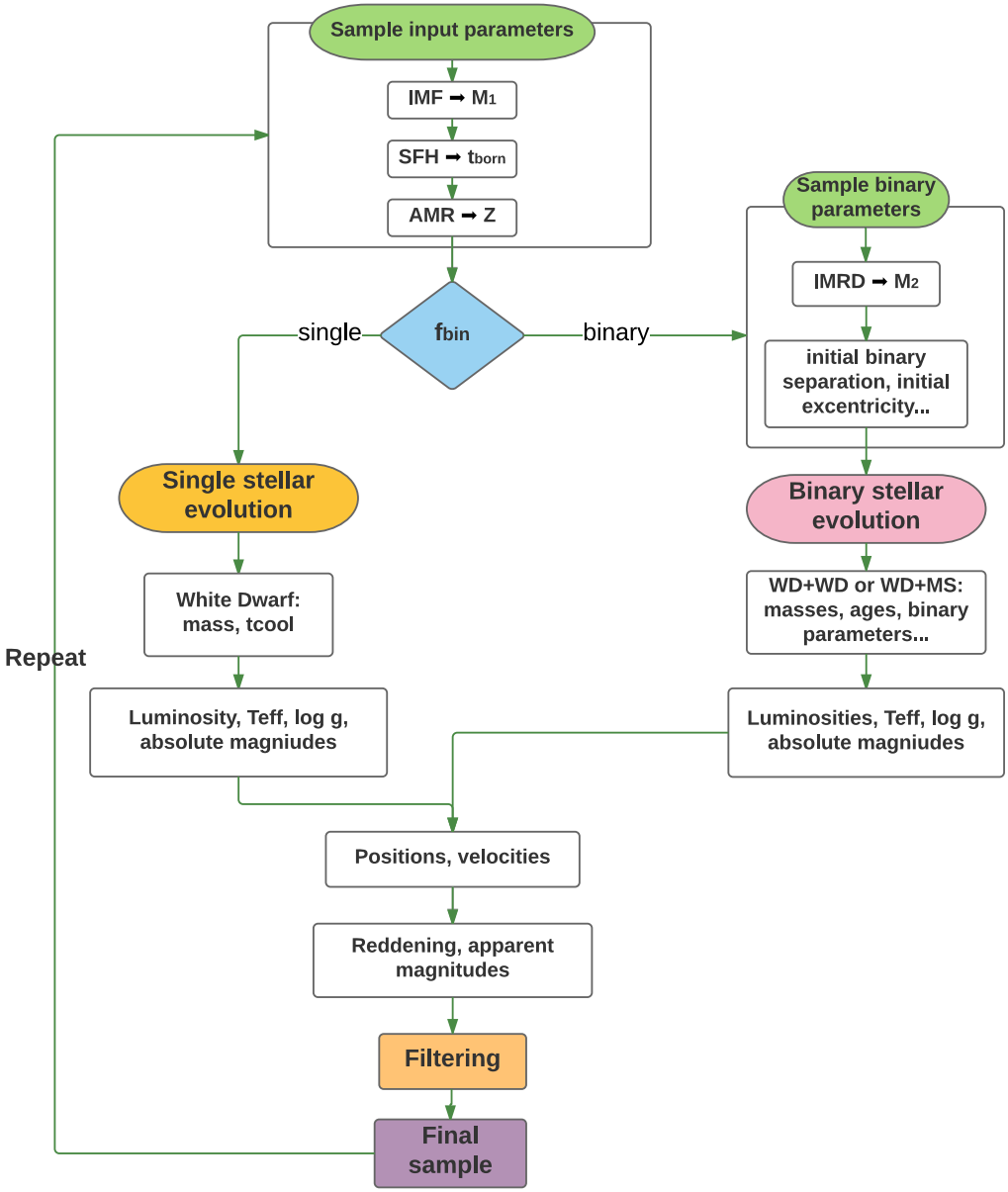

Figure 2.1: A simplified flowchart representation of the population synthesis code. The acronyms used in this diagram are: IMF initial mass function, SFH star formation history, AMR age metallicity relation, $f_{\rm bin}$ binary fraction, IMRD initial mass ratio distribution, WD white dwarf, MS main sequence, M_1 progenitor/initial primary mass, M_2 initial secondary mass, $t_{\rm born}$ age at which the star is formed, Z progenitor metallicity, $t_{\rm cool}$ white dwarf cooling time, $T_{\rm eff}$ effective temperature, and g surface gravity.

2.2.1 Simulating the single white dwarf population

Once the ZAMS mass, M, and the metallicity of the synthetic stars are known, evolutionary sequences to compute the main-sequence lifetimes, $t_{\rm MS}$, can be used. The evolutionary ages of the progenitors were typically interpolated in the BaSTI database for the appropriate metallicity (Pietrinferni et al., 2004), that covers progenitor masses from 0.5 to 10 $M_{\odot}$ and metallicities between $Z = 0.0001$ and $Z = 0.04$. Using the population age, T, we can easily evaluate which of those stars had time to become white dwarfs. If that is the case the cooling age is simply given by $t_{\rm cool} = T - t_{\rm MS} - t_{\rm born}$. After that, we use an initial-to-final mass relation (IFMR) to obtain the white dwarf mass, $M_{\rm WD}$. For this we typically employ the relation from Catalán et al. (2008):

$$M_{\rm WD} = \begin{cases} 0.096M + 0.429 & M/M_{\odot} \leq 2.7 \\ 0.137M + 0.3183 & 2.7 \leq M/M_{\odot} \leq 6.0 \\ 0.1057M + 0.5061 & M/M_{\odot} > 6.0 \end{cases} \tag{2.2}$$

Next, we compute present time stellar parameters (luminosity, $T_{\rm eff}$, $\log g$) using cooling tracks adequate for the white dwarf mass and progenitor metallicity. Our standard choices for the cooling tracks for Solar metallicity and hydrogen-rich atmospheres are the following. For carbon-oxygen white dwarfs ($0.45 < M_{\rm WD} < 1.1\,M_{\odot}$) we use the evolutionary calculations of Renedo et al. (2010), for oxygen-neon core white dwarfs ($M_{\rm WD} > 1.1\,M_{\odot}$) we employ those of Althaus et al. (2005a); Althaus et al. (2007) and for helium core white dwarfs($M_{\rm WD} < 0.45\,M_{\odot}$) we use the cooling tracks from Serenelli et al. (2001). In Chapter 3 we explore the influence of metallicity on the disk white dwarf luminosity function, using a tridimensional interpolation scheme based on the white dwarf mass, cooling time and progenitor metallicity. In Chapter 5, we study the halo white dwarf luminosity function using a self-consistent model (main sequence lifetimes, IFMR, cooling tracks) for very low metallicities.

2.2.2 Simulating white dwarfs in binaries

In part of this work, we will focus on reproducing the population of white dwarf-main sequence binaries with M dwarf companions. In this section will give details which are relevant to reproduce the properties of this specific population, although the code can be employed to explore other type of outcomes, such as double-degenerate pairs or binaries formed by a white dwarf and an F/G/K main-sequence star.

If the synthetic star is part of a binary system we obtain the ZAMS mass of the secondary star according to an initial mass ratio distribution (IMRD). In Chapter 6 we explore several models for this distribution. The initial separation of the binary is chosen from a logarithmically flat distribution (Davis et al., 2008):

$$\Phi(a) = 0.07863a^{-1},\ 3 \leq a/R_{\odot} \leq 10^6 \tag{2.3}$$

and the initial eccentricity from a linear thermal distribution (Heggie, 1975):

$$\Phi(e) \sim 2e,\ 0 \leq e \leq 0.9 \tag{2.4}$$

If the primary star has had time to become a white dwarf, then the system can evolve through two different pathways. In the first of them, the binary evolves without mass transfer interactions as a detached system and the primary star evolves into a white dwarf that subsequently cools down. In this case, the mass of the white dwarf is also calculated using the initial-to-final mass relation from Hurley et al. (2002), which results from the evolution algorithm and consists basically of a competition between core-mass growth and envelope mass-loss. The second pathway involves mass transfer and the evolution of the binary is computed using the BSE package of Hurley et al. (2002), following the parameter assumptions detailed in Camacho et al. (2014). These are conservative evolution on the main sequence, mass-loss on the giant branch and beyond following the prescription from Kudritzki & Reimers (1978) with an efficiency $\eta = 0.5$, but no enhanced mass loss ($B_{\rm W} = 0$), tidal evolution, circularization and synchronization, angular momentum losses due to magnetic braking and gravitational radiation assuming disruptive magnetic braking (Schreiber et al., 2010).

If the system evolves through the common envelope (CE) phase we follow the α-formalism as described in Tout et al. (1997), with $\alpha_{\rm CE}$ being the efficiency in converting orbital energy into kinetic energy to eject the envelope:

$$E_{\rm bind} = \alpha_{\rm CE} \Delta E_{\rm orb} \tag{2.5}$$

This implementation also takes into account the $\alpha_{\rm int}$ parameter, first presented in Han et al. (1995), describing the fraction of the internal energy used to eject the envelope:

$$E_{\rm bind} = \int_{M_{\rm core}}^{M_{\rm donor}} \left(-\frac{GM(r)}{r} + \alpha_{\rm int} U_{\rm int} \right) {\rm d}m \tag{2.6}$$

We use up-to-date cooling tracks to compute the luminosities, temperatures, surface gravities and the photometric magnitudes in the Johnson-Cousins $UBVRI$ system for both the main sequence and white dwarf components. For the main sequence companion, we employ the new evolutionary tracks from Baraffe et al. (2015), which cover a mass range from 0.07 to 0.5 $M_{\odot}$, and for the white dwarf primary we follow the cooling tracks discussed in Section 2.2.1.

2.3 Galactic model

With the purpose of accounting for stellar positions and velocities, we employ a Galactic model, designed to reproduce stellar densities and kinematics for the thin

and thick disk and the stellar halo. We then proceed to allocate a position and a set of velocities, according to stellar density and kinematic model adequate for the Galactic stellar population to which the star is assumed to belong to. If we are generating a fixed number of stars in each iteration, we have the option to perform this step only for stars that have become white dwarfs (as shown in Fig. 2.1), because simulating stellar densities is a costly process in terms of computational time, especially if rejection sampling is used. However, if we decide to impose a limit on the local stellar mass density, we need to provide positions for every simulated ZAMS star or binary pair. In one of our typical Monte Carlo simulations, we generate stars up to several kpc (usually up to 5 kpc) and densities are normalized up to 200 pc from the Sun. When the local density of the test sample reaches that of the observed local value, we stop generating artificial stars in the current Monte Carlo realization. For the thin disk this density is $\rho_{\rm thin} = 0.094\, M_{\odot}/pc^3$ (Holmberg & Flynn, 2000), and for the thick disk is $\rho_{\rm thick} = 0.085\rho_{thin}$ (Reid, 2005)).

2.3.1 The thin and thick disks

For the thin and thick disk, the positions of stars are randomly generated within a spherical region centered in the Sun with a radius R, generally adopted to be 5 kpc. For the local density of stars, a double exponential distribution is used, with a constant Galactic scale height, H, and a constant scale length, L (see Fig. 2.2 for an example). The election in scale height and scale length must be made in accordance to the characteristics of the thin or thick disk populations, as explained in more detail in Section 1.4. However, a more detailed treatment of spatial densities can be given, taking into account the positions of the observational plates used to obtain the reference sample. Such a detailed treatment is presented in Chapter 6.

Velocities are obtained following the procedure from (García-Berro et al., 1999), being sampled from normal laws:

$$\begin{aligned} n(u) &\sim e^{-(u-u_0')/\sigma_u^2}, \\ n(v) &\sim e^{-(v-v_0')/\sigma_v^2}, \\ n(w) &\sim e^{-(w-w_0')/\sigma_w^2}, \end{aligned} \tag{2.7}$$

where (u_0', v_0', w_0') are derived from the peculiar velocity of the Sun, $(u_{\odot} = 11.10, v_{\odot} = 12.24, w_{\odot} = 7.25)$ (Schönrich et al., 2010), and taking into account the differential rotation of the Galaxy (Ogorodnikov, 1965). The velocity dispersions $(\sigma_u, \sigma_v, \sigma_w)$ (expressed in km/s) and the lag velocity v_0 depend on the scale height (H, expressed

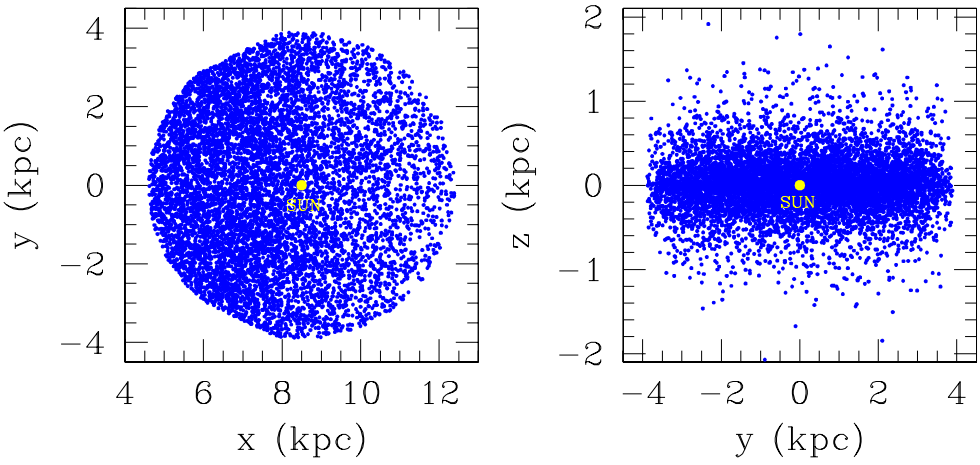

Figure 2.2: Projections of the spatial distribution of the synthetic sample, according to a double exponential disk density model. The location of the Sun is represented by a yellow circle.

Disk	u'_0	v'_0	w'_0	σ_u	σ_v	σ_w
Thin	-8.62	-20.04	-7.10	32.4	23.0	18.1
Thick	-11.0	-42.0	-12.0	50.0	56.0	34.0

Table 2.1: Mean motions relative to the Sun and velocity dispersion tensor from Rowell & Hambly (2011) (and references therein), for the thin and thick disk populations

in kpc) through a dispersion law (Mihalas & Binney, 1981):

$$\begin{gathered} u_0 = 0, \\ v_0 = -\sigma_u^2/120, \\ w_0 = 0, \end{gathered} \qquad \begin{gathered} \sigma_u = \sigma_w\sqrt{2}, \\ \sigma_v = \sigma_u\sqrt{0.32 + 1.67 \cdot 10^{-5}\sigma_u^2}, \\ \sigma_w = \sqrt{\frac{H}{6.25 \cdot 10^{-4}}}, \end{gathered} \tag{2.8}$$

This approach is used in Chapters 3 and 4. In Chapter 6, we use constant values for (u'_0, v'_0, w'_0) and $(\sigma_u, \sigma_v, \sigma_w)$, as shown in Table 2.1.

2.3.2 The Galactic stellar halo

To reproduce the halo stellar population, we use the isothermal sphere density model:

$$\rho(r) \propto \frac{a^2 + R_\odot^2}{a^2 + r^2}, \tag{2.9}$$

where $a \approx 5\,\mathrm{kpc}$ is the core radius, and $R_\odot = 8.5\,\mathrm{kpc}$ is the galactocentric distance of the Sun. Of course, other density models can be used, and this possibility is explored in Chapter 5. The velocities of the simulated halo stars were randomly drawn from normal distributions (Binney & Tremaine, 1987):

$$f(v_r, v_t) = \frac{1}{(2\pi)^{3/2}} \frac{1}{\sigma_r \sigma_t^2} \exp\left[-\frac{1}{2}\left(\frac{v_r^2}{\sigma_r^2} + \frac{v_t^2}{\sigma_t^2}\right)\right], \tag{2.10}$$

where σ_r and σ_t are the radial and the tangential velocity dispersions, respectively, which can be related using the following expression:

$$\sigma_t^2 = \frac{V_\mathrm{c}^2}{2} + \left[1 - \frac{r^2}{a^2 + r^2}\right]\sigma_r^2 + \frac{r}{2}\frac{\mathrm{d}(\sigma_r^2)}{\mathrm{d}r}, \tag{2.11}$$

which, to a first approximation, leads to $\sigma_r = \sigma_t = V_\mathrm{c}/\sqrt{2}$. The velocity dispersions σ_r and σ_t are those determined by Markovic & Sommer-Larsen (1997). For the calculations reported here, we adopted a circular velocity $V_\mathrm{c} = 220\,\mathrm{km/s}$. From these velocities, we obtained the heliocentric velocities of each simulated star by adding the velocity of the local standard of rest (LSR) $v_\mathrm{LSR} = -220\,\mathrm{km/s}$, and the peculiar velocity of the Sun.

2.4 Computing photometric magnitudes

Evolutionary sequences and white dwarf cooling tracks typically provide photometric magnitudes in the Johnson-Cousins $UBVRI$ system. When required, we convert these to the *ugriz* color system, necessary for comparing to observational samples obtained from the SDSS or LAMOST (see Chapter 4) surveys. In these cases, we use the transformations described in Jordi et al. (2006). In Chapters 3 and 5, we also compared to samples from the SSS, which uses the photographic b_J, r_59F and i_N bands, and for this we use the color transformations described in Xu et al. (2007).

When necessary, reddening was computed taking into account the position of the object. In Chapter 4, this was done using a 3D Galactic extinction map from Chen et al. (2014) and the extinction coefficients of Yuan et al. (2013). In Chapters 6, we used the results of Hakkila et al. (1997) and updated coefficients from Schlafly et al. (2010).

Chapter 3

The effects of metallicity on the Galactic disk population of white dwarfs

3.1 Introduction

Cosmic age determinations are usually obtained by employing models and evolutionary tracks for stars with Solar metallicity, which is the median value for the metallicity distribution function (MDF) of the Galactic disk. However, the entire span of this distribution function is many times neglected. Over the years, photometric studies of main sequence stars have resulted in the release of large catalogs (Twarog, 1980; Olsen, 1983; Strömgren, 1987; Nordström et al., 2004; Haywood, 2008). In most occasions these catalogs contain one parameter for metallicity and no detailed element abundances. Perhaps, one of the most important results of these surveys is that high-metallicity stars are present throughout the entire mass range and that the MDF depends on the stellar age. Even if the peak value for the metallicity remains approximately at Solar values, young stars have a much narrower distribution than old stars, which suggests that a correct sampling should be denser for younger stars (Casagrande et al., 2011). The rather symmetric shape of the MDF is explained through the natural process of star migration (Sellwood & Binney, 2002), in which high-metallicity stars migrate from the inner disk and low-metallicity stars do so from the outer disk. Additionally, it is believed that old stars probably play a more significant role in this situation, given that they clearly contribute to the lower metallicity wing of the MDF (Casagrande et al., 2011). This may have important consequences. On the one hand, recent studies have shown that high values of the metallicity imply slower evolutionary rates for moderately cool white dwarfs due to the sedimentation of ^{22}Ne (Isern et al., 1991; García-Berro et al., 2010; Althaus et al., 2010b). Moreover, metallicity modifies the lifetime of white dwarf progenitors, and

there is not yet a consensus of whether the initial final mass relationship is modified – for a preliminary discussion see Isern et al. (2005). Obviously, these effects may affect the age determination of the Galactic disk obtained using the faint downturn of the white dwarf luminosity function. The ultimate goal of this work is to assess how the evolution of the metallicity of the Galactic disk affects the shape of the white dwarf luminosity function.

To accomplish this aim, we employ two metallicity laws. The first of them is a metallicity law with a median corresponding to the Solar value and a dispersion around it (Casagrande et al., 2011), whereas the second one is the classical age-metallicity relationship of Twarog (1980). The chapter is organized as follows. In Section 3.2, we explain the most basic features of our population synthesis code, while we describe the two most recent and reliable observational samples with which we compare our simulated data in Section 3.3. We then discuss the selection criteria employed to cull a representative sample of white dwarfs from these surveys. Section 3.4 is devoted to explaining in depth the results of our Monte Carlo simulations and to thoroughly compare our population synthesis results with the observational data. Finally, we review our most relevant findings, discuss their significance, and summarize our conclusions in Section 3.5.

3.2 Input parameters, evolutionary sequences and cooling tracks

The population synthesis code is extensively described in Chapter 2, so here we will limit ourselves to presenting the specifics inputs related to simulating the white dwarf population in the Galactic thin disk. The local density of stars in the thin disk is described by a double exponential distribution with a scale height 250 pc and a scale length of 3.5 kpc. The time at which each synthetic star was born was sampled according to a constant star formation rate, and we adopted a disk age of 9.5 Gyr, except otherwise stated. The mass of each star follows the standard initial mass function of Kroupa (2001) and Kroupa & Weidner (2003). Velocities were randomly obtained following the prescription from Section 2.3.1. The evolutionary ages of the progenitors were interpolated in the BaSTI database for the appropriate metallicity (Pietrinferni et al., 2004). Given the age of the Galaxy and the age, metallicity, and mass of the progenitor star, we know which synthetic stars have had time to become white dwarfs, and for these, we derive their mass using the initial-final mass relationship of Catalán et al. (2008).

In our reference calculations we used the evolutionary calculations of Renedo et al. (2010) for carbon-oxygen white dwarfs with hydrogen-rich atmospheres, and those of Benvenuto & Althaus (1997) for hydrogen-deficient envelopes, while we used those of Althaus et al. (2007) and Althaus et al. (2005a) for white dwarfs with oxygen-neon cores. However, to assess the effects of the different cooling tracks in the

white dwarf luminosity function in additional sets of calculations, we also employed the cooling tracks of Fontaine et al. (2001) and of the BaSTI project (Salaris et al., 2010) for carbon-oxygen white dwarfs with pure hydrogen atmospheres and those of Fontaine et al. (2001) and Bergeron et al. (2011) for white dwarfs with helium dominated atmospheres. We convert $UBVRI$ colors to the $ugriz$ color system when we compare to the SDSS sample, using the transformations described in Jordi et al. (2006). To compare with the sample of white dwarfs of the SSS, we used the color transformations described in Xu et al. (2007).

For each of the models studied below, we generated 50 independent Monte Carlo simulations (with different initial seeds), and for each of these Monte Carlo realizations, we increased the number of simulated Monte Carlo realizations to 10^4 using bootstrap techniques. Using this procedure, we ensure convergence in all the final values of the relevant quantities. In what follows for each quantity of interest, we present the ensemble average of the different Monte Carlo realizations, as well as the corresponding standard deviation. Following all these steps, we were able to produce a synthetic population of disk white dwarfs, which, by definition, is complete. To this population, a series of filters, which take the observational cuts into account, must be applied. We describe these filters in Section 3.3.

3.3 The observational samples

The two most recent, complete, and reliable samples of disk white dwarfs are those obtained from the SDSS and from the SSS. In this section, we describe them separately, placing special emphasis on the observational cuts employed to derive the corresponding luminosity functions. In our population synthesis study, we closely follow the prescriptions employed to obtain the observed samples with the ultimate goal of producing theoretical white dwarf populations that are as realistic as possible for both the white dwarf sample of the SDSS and for that of the SSS, since this is crucial to derive white dwarf luminosity functions that can be compared to the observational data in a meaningful way.

The SDSS surveyed $5,282\,\mathrm{deg}^2$ of high-latitude sky in five bandpasses $ugriz$ – see Fukugita et al. (1996), Gunn et al. (1998), and Gunn et al. (2006) for additional details – and, besides quasars and galaxies, obtained many spectra of white dwarfs and other blue stars. Using the SDSS Data Release 4, Eisenstein et al. (2006a) presented a catalog of 9,316 spectroscopically confirmed white dwarfs. The catalog contains both hydrogen-rich (DA) and hydrogen-deficient (non-DA) white dwarfs. From it, Harris et al. (2006) used photometric distances, USNO proper motions, and the $1/V_{\mathrm{max}}$ method (Schmidt, 1968) and derived a white dwarf luminosity function. In particular, to obtain this luminosity function, they considered all stars brighter than $g < 19.5$. To discriminate between main sequence stars and white dwarfs they

employed the reduced proper motion,

$$H_g = g + \log \mu + 5 = M_g + 5 \log V_{\rm tan} - 3.379, \tag{3.1}$$

where μ is the proper motion and $V_{\rm tan}$ is the tangential velocity. Specifically, they required that all objects contributing to the white dwarf luminosity function should be below and blueward the reduced proper motion corresponding to $V_{\rm tan} = 20\,{\rm km\,s^{-1}}$ in the reduced proper motion-color diagram. Additionally, they only selected white dwarfs with $15 < g < 19.5$, and proper motions $\mu > 0.02''$ yr^{-1}. The resulting sample contains about 7,000 white dwarfs. Later on, De Gennaro et al. (2008), who used 3,358 white dwarfs, presented an improved white dwarf luminosity function, in which only spectroscopically confirmed DA white dwarfs were employed. To obtain this luminosity function, they adopted $V_{\rm tan} > 30\,{\rm km\,s^{-1}}$. However, given that this luminosity function does not present a cut-off, as the luminosity function of Harris et al. (2006) does, we do not use it.

The other large observational sample of disk white dwarfs is that obtained from the SSS (Rowell & Hambly, 2011). The SSS is an advanced photographic plate-digitizing machine. The plates were taken with the UK Schmidt telescope (UKST), the ESO Schmidt telescope, and the Palomar Schmidt telescope, and the resulting catalogs have been compiled by digitizing several generations of photographic Schmidt plates. The photometric system of this survey is less well known than that of the SDSS and has three passbands, $b_{\rm J}$, $r_{\rm 59F}$, and $i_{\rm N}$ – see Hambly et al. (2001) for details. Using the data of several generations of these plates, Rowell & Hambly (2011) constructed a catalog of about 10,000 white dwarfs with magnitudes down to $r_{\rm 59F} \sim 19.75$ and proper motions as low as $\mu \sim 0.05''$ yr^{-1}, which covers nearly three quarters of the sky. The observational selection criteria adopted to derive the corresponding white dwarf luminosity function are the following. First, the proper motion cut depends on the $b_{\rm J}$ magnitude,

$$\mu > 5\left(\sigma_\mu^{\rm max}(b_{\rm J}) + 0.002\right). \tag{3.2}$$

In this expression, σ_μ is the standard deviation in the proper motion measurements, which means that the measured proper motion is 5σ larger than the error at a given $b_{\rm J}$. Additionally, there is a magnitude cut $12 < r_{\rm 59F} < 19.75$, whereas they also imposed a cut in the reduced proper motion diagram, by adopting $V_{\rm tan} > 30\,{\rm km\,s^{-1}}$.

3.4 Results

Before assessing the role of the adopted metallicity law, it is convenient to check whether or not other aspects can mask its impact on the white dwarf luminosity function. For instance, the ratio of white dwarfs with hydrogen-deficient atmospheres to those with hydrogen-rich ones depends on the effective temperature, and this could possibly influence the shape of the white dwarf luminosity function. Hence,

we first check if this could mask the effects of the adopted metallicity law. This is done in Section 3.4.1. The same can be said about the adopted theoretical white dwarf cooling sequences. Quite obviously, the adopted white dwarf cooling tracks also influence the precise shape of the luminosity function. Consequently, we also explore and quantify this possibility in Section 3.4.2. Finally, we analyze the effects of the adopted metallicity law in Section 3.4.3. We emphasize that all the luminosity functions presented in this section have been computed adopting a constant star formation rate.

3.4.1 The fraction of non-DA white dwarfs

To begin with, we discuss the role of the ratio of the number of white dwarfs with hydrogen-deficient atmospheres to the total number of white dwarfs, including those with hydrogen-rich atmospheres. Most white dwarf stars have hydrogen-dominated atmospheres, constituting the group of so-called DA white dwarfs. However, hydrogen-deficient white dwarfs, known as non-DA stars, represent between 15% and 25% of the total white dwarf population of the Galaxy (Fontaine et al., 2001). In our attempt to properly analyze factors that might potentially influence the shape of the white dwarf luminosity function and given that the most recent luminosity functions incorporate both DA and non-DA white dwarfs, we first try to reproduce the observed ratio of non-DA to the total number of white dwarfs. For this set of simulations, we adopt the cooling sequences of our reference model and the evolutionary ages of white dwarf progenitors of Solar metallicity. That is, we assumed that all synthetic stars have Solar metallicity.

The observed ratio of non-DA white dwarfs as a function of the bolometric magnitude is shown in all three panels of Fig. 3.1 using a dotted line. The observational data has been compiled from Krzesinski et al. (2009) for hot white dwarfs – namely, those with effective temperatures larger than $T_{\rm eff} \simeq 25,000$ K – and De Gennaro et al. (2008) and references therein for cooler white dwarfs. The upper panel of Fig. 3.1 shows the ratio of the number of non-DA white dwarfs as a function of the bolometric magnitude when all synthetic white dwarfs of an otherwise typical Monte Carlo realization are considered – that is, for a complete sample – as a solid line. This simulation was computed assuming that 20% of white dwarfs at birth have atmospheres devoid of hydrogen, while the lower two panels show the same distribution when the cuts of Harris et al. (2006) and Rowell & Hambly (2011) are applied to the complete sample, respectively. Thus, these two last Monte Carlo realizations incorporate the biases introduced by the selection criteria. As can be seen in general, our theoretical results are in excellent agreement with the observational data, except at very high luminosities – namely for $M_{\rm bol} \lesssim 2.0$ – for which the non-DA ratio predicted by our simulations for the complete sample is considerably smaller (~ 0.5) than the observed one (~ 1.0). We note, however, that the number density of white dwarfs is very small at these bolometric magnitudes and, hence, this ratio presents

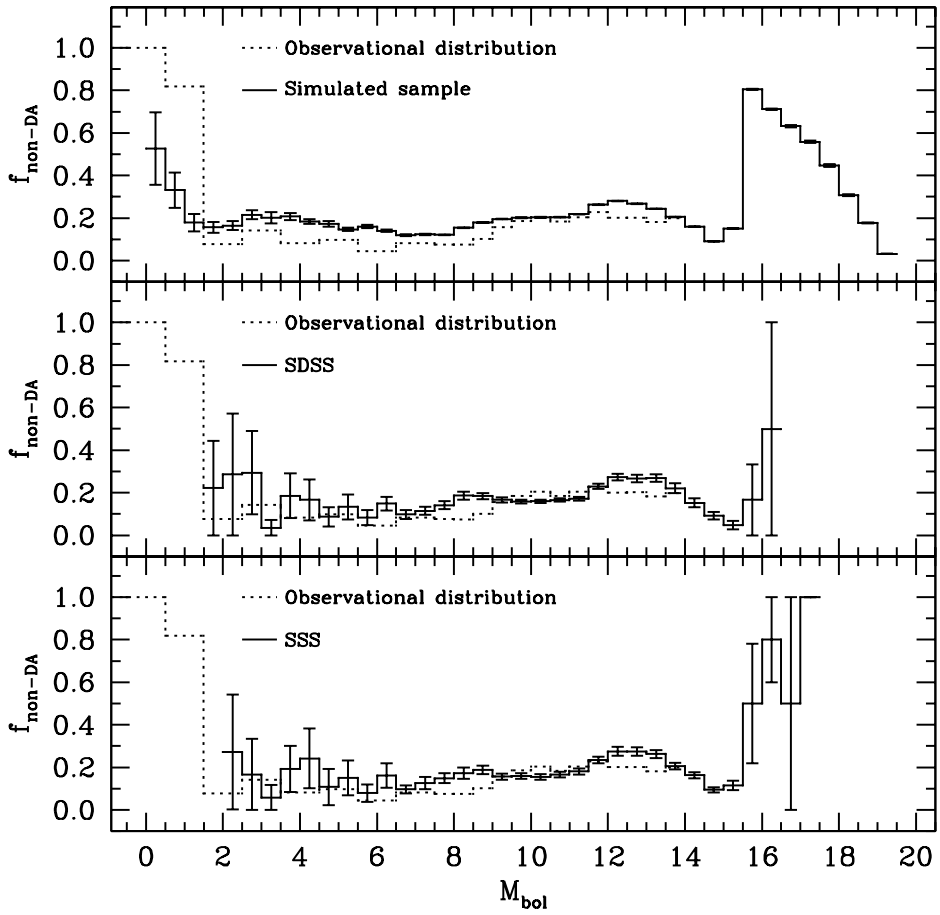

Figure 3.1: Distribution of the ratio of non-DA to the total number of white dwarfs as a function of the bolometric magnitude. The solid line represents the simulated sample, whereas the dotted line corresponds to the observational data. See text for additional details.

large fluctuations, depending on the specific Monte Carlo realization chosen. It is worth noting that the effects of the selection criteria for this range of bolometric magnitudes is important as well, as the ratio of non-DA white dwarfs turns out to be ~ 0.5 for the complete sample. This ratio drops to ~ 0.0 for the two restricted samples, although the statistical fluctuations are very large. Another interesting aspect of the theoretical results that is also worth commenting is that at very low luminosities, our population synthesis calculations predict a noticeable increase of the ratio of non-DA to DA white dwarfs for the complete sample, which agrees with what is found for the local sample of white dwarfs (see Giammichele et al., 2012, and references therein). This is evident as well for the sample of white dwarfs in which

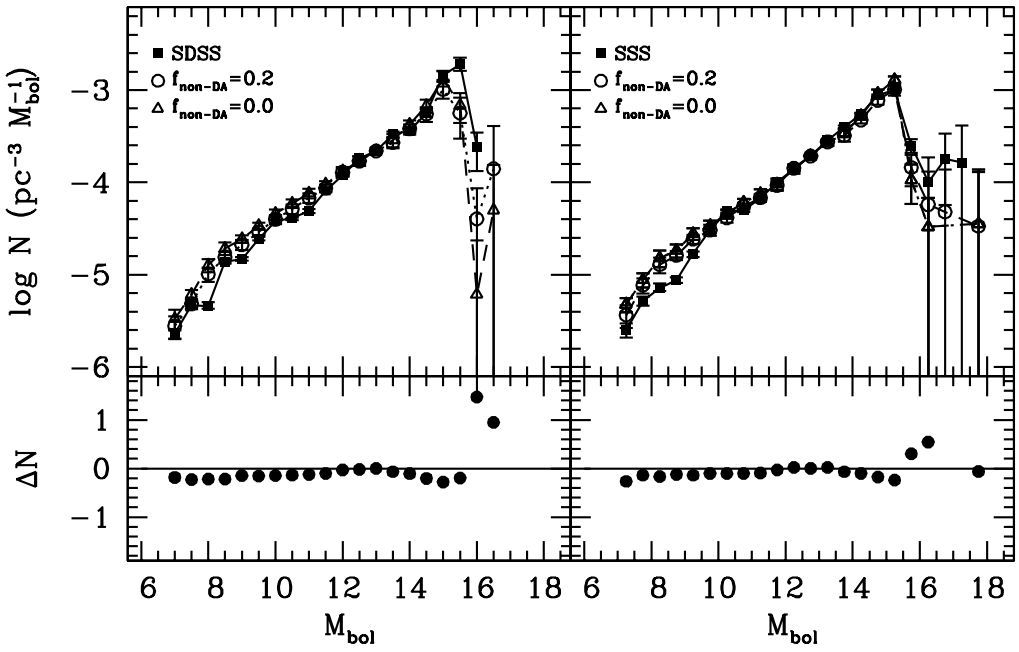

Figure 3.2: Simulated white dwarf luminosity function for a pure DA white dwarf population (open triangles) and for a population in which a canonical fraction of 20% of non-DA white dwarfs (open circles) is adopted. Both luminosity functions are compared with the observational white dwarf luminosity function (solid squares) of Harris et al. (2006) (left top panel) and Rowell & Hambly (2011) (right top panel). In the bottom panels, we show the residuals between the synthetic luminosity functions.

the selection criteria of Rowell & Hambly (2011) are used. If the selection criteria of Harris et al. (2006) are employed, the ratio of non-DA white dwarfs does not show such a marked increase because very few low luminosity white dwarfs are found when this set of criteria is adopted. We elaborate on this below when discussing the white dwarf luminosity function.

Once established that the adopted 20% ratio of non-DA white dwarfs at birth results in a credible distribution for all luminosities, we test the actual impact of this ratio on the white dwarf luminosity function. To this end we compute an additional set of Monte Carlo simulations for which we adopt $f_{\rm non-DA} = 0.0$ and we compare the corresponding luminosity function with that obtained using $f_{\rm non-DA} = 0.2$. The result of this exercise is shown in Fig. 3.2. In the top panels of this figure the luminosity functions obtained when $f_{\rm non-DA} = 0.0$ and $f_{\rm non-DA} = 0.2$ are compared, while the observed luminosity functions of Harris et al. (2006) and Rowell & Hambly (2011) are also displayed in the respective panels. Obviously, to produce these luminosity functions, the corresponding selection criteria have been used. The

bottom panels of this figure display the residuals between both theoretical luminosity functions, which help in assessing the differences between both simulations, as defined as

$$\Delta N = 2\frac{N_{f_{\rm DB}=0.2} - N_{f_{\rm DB}=0}}{N_{f_{\rm DB}=0.2} + N_{f_{\rm DB}=0}}. \tag{3.3}$$

As can be seen in the bottom panels of Fig. 3.2, the effect of the adopted non-DA ratio on the simulated white dwarf luminosity functions is minimal, except for bolometric magnitudes larger than $M_{\rm bol} \simeq 15$. For the bins with bolometric magnitudes larger than this value, the differences are noticeable in both cases, and the luminosity function in which $f_{\rm non-DA} = 0.2$ is in better agreement with the observational one. In particular, when $f_{\rm non-DA} = 0.2$, is adopted the number density of low-luminosity white dwarfs increases, as should be expected, given that white dwarfs with hydrogen-defficient atmospheres cool faster. Actually, the number density of white dwarfs for the luminosity functions computed with $f_{\rm non-DA} = 0.0$ is consistent with zero, since for these bins we obtain at most only one object per bin in all Monte Carlo realizations. We thus conclude that the hot branch of the white dwarf luminosity function is almost insensitive to the adopted ratio of non-DA white dwarfs and that the effects of this ratio concentrate in the poorly determined bins with the lowest luminosities.

3.4.2 The effects of the adopted cooling tracks

We now discuss which set of cooling sequences best reproduces the shape of the observed white dwarf luminosity function. To this end in Fig. 3.3, we compare various sets of evolutionary cooling sequences with the two most recent and reliable observational white dwarf luminosity functions, namely that of Harris et al. (2006) and that of Rowell & Hambly (2011). The data shown in this figure corresponds to the ensemble average of several single independent Monte Carlo realizations, as described before, with the inputs described in Section 3.2. In the top panels of this figure, we display the results of such comparison when the luminosity functions obtained using the cooling tracks of Fontaine et al. (2001) are compared to those obtained using our reference model, as done in Section 3.2, whereas a comparison of the results obtained when the cooling sequences of Salaris et al. (2010) and those obtained when the cooling tracks of Renedo et al. (2010) are used is performed in the bottom panels. In each panel, we also show the residuals between both theoretical simulations. As we did previously for all the calculations shown in this figure, we adopted a constant metallicity equal to the Solar value.

Figure 3.3 demonstrates that all three sets of cooling sequences match the bright branch of both observational white dwarf luminosity functions very well and that there are not appreciable differences between all three luminosity functions at high luminosities. This agreement is even better when the white dwarf luminosity function

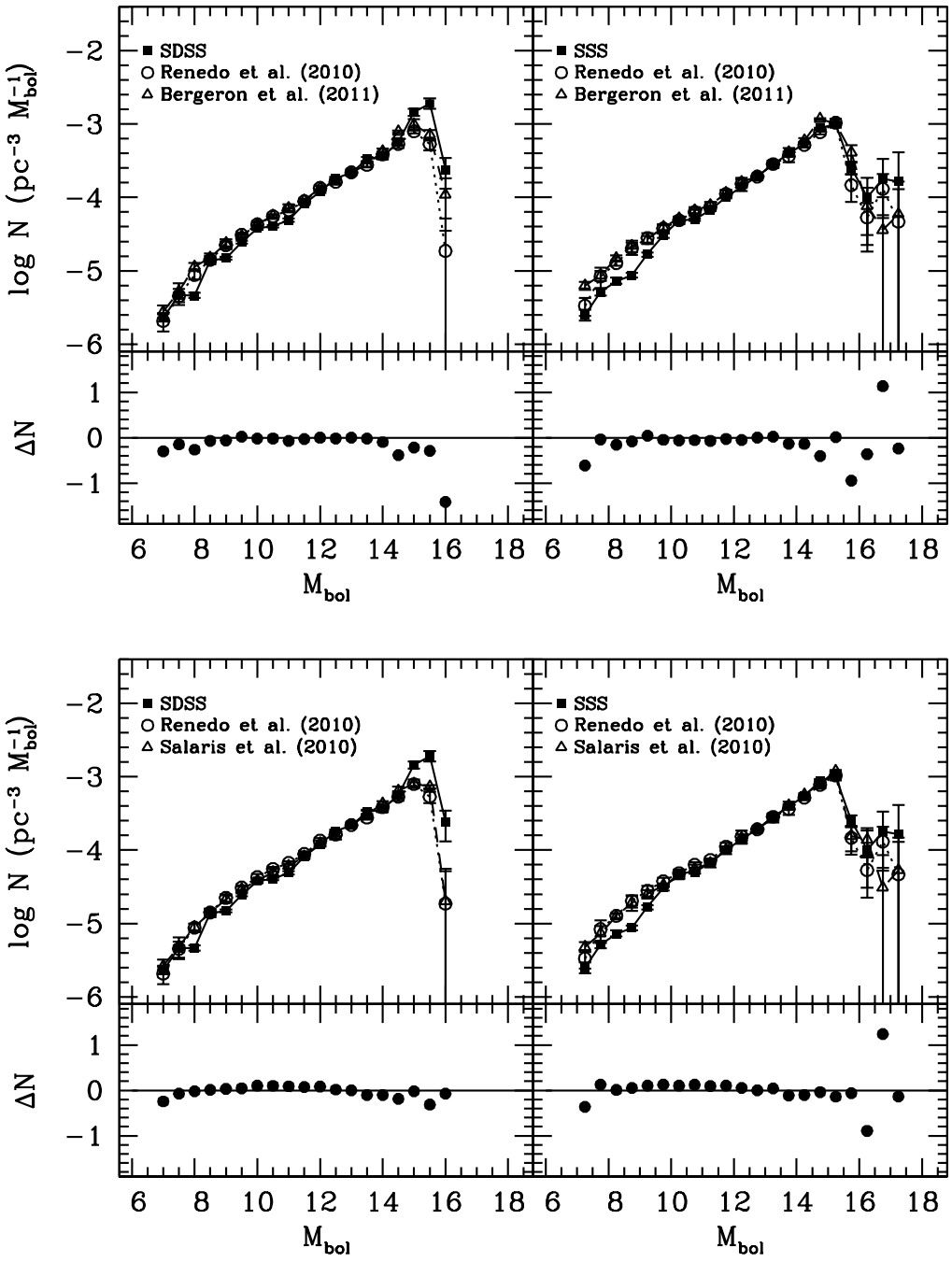

Figure 3.3: Simulated white dwarf luminosity functions computed using our reference model (open circles) compared to those obtained using the cooling sequences of Fontaine et al. (2001) (top panels, open triangles) and Salaris et al. (2010) (bottom panels, also open triangles). Also shown are the observational white dwarf luminosity function (solid squares) of Harris et al. (2006) (left panels) and Rowell & Hambly (2011) (right panels). The synthetic white dwarf luminosity functions have been normalized to the observational point with minimum error bars.

of Rowell & Hambly (2011) is adopted, as the location of the maximum of the white dwarf luminosity function is nicely fit by all three sets of cooling tracks. Now, we turn our attention to the cool branch of the white dwarf luminosity function and the shape of its drop-off. Again, all three sets of cooling sequences are in excellent agreement with the observational data, although we emphasize that selection effects may play a key role at these very low luminosities and both the Monte Carlo simulated sample and the real ones suffer from poor statistics. Nevertheless, we note that all three sets of calculations reproduce the downturn at very faint magnitudes of the luminosity function obtained from the SSS, which is not present in the luminosity function of Harris et al. (2006) because of the sample selection procedures. Given these results, there are no objective reasons for discarding any set of evolutionary sequences, and hence for here on, we adopt the cooling sequences of our fiducial model, which is based on the theoretical cooling sequences of Renedo et al. (2010).

3.4.3 The influence of the metallicity law

Metallicity is known to have a considerable influence in age estimations obtained when the turn-off of main sequence stars of stellar clusters is employed to derive the corresponding age. Hence, it is natural to wonder whether or not the age derived from the drop-off of the disk white dwarf luminosity function depends on the adopted age-metallicity relationship. To perform this analysis, we adopted two different metallicity laws. The first one is the classical metallicity law of Twarog (1980), which predicts that the metallicity of white dwarf progenitor stars monotonically increases from zero at very early ages of our Galaxy to Solar metallicity for the current age of the Galactic disk. Specifically, the metallicities of the individual synthetic stars are randomly drawn by following a Gaussian distribution centered in $F(t)$, where $F(t)$ is a polynomial fit of the results presented in Fig. 1 of Bravo et al. (1993) with a dispersion $\sigma = 0.1$. Our second age-metallicity relationship is based on the observational data compiled by the Geneva-Conpenhague survey (Casagrande et al., 2011). This recent study predicts that the metallicity of the Galactic disk is constant with time but has a sizable dispersion. We note that this distribution of metallicities has been confirmed by the recent results of Duran et al. (2013). Thus, for the same age, white dwarf progenitors span a broad range of metallicities. In particular, for each synthetic star, we randomly drawn its metallicity, Z, from a Gaussian distribution centered in the solar metallicity, $Z_{\odot}$, with a spread found by Casagrande et al. (2011), of $\sigma = 0.4$.

Whatever the adopted age-metallicity relationship is in both cases we interpolate both the main-sequence lifetimes of the progenitors and the final masses, cooling times, colors and luminosities of the resulting white dwarfs. For this analysis, we adopt the set of cooling sequences of Renedo et al. (2010), which almost cover the full range of metallicities. If a progenitor star has metallicity lower than $Z = 10^{-3}$, the lowest metallicity of the evolutionary sequences of Renedo et al. (2010), we adopt

the values predicted by these calculations. If the metallicity of the progenitor stars is larger than $Z = 10^{-2}$, we interpolate between the evolutionary sequences of Renedo et al. (2010) and those of Althaus et al. (2010b), which have a maximum metallicity of $Z = 0.06$, which is enough for our purposes. Finally, we adopt an age for the Galactic disk of 9.5 Gyr.

Our results are presented in Fig. 3.4. In particular, we compare the luminosity functions obtained using the age-metallicity relationship of Twarog (1980) and using a fixed value of the metallicity equal to the Solar one with the observational luminosity functions of the SDSS and the SSS in the upper panels of this figure. In the bottom panels, we show the same comparison, but this time using the metallicity law of Casagrande et al. (2011). As in previous figures, we also show the corresponding differences between the theoretical calculations. As can be seen, both theoretical calculations yield almost the same results, and most importantly, the position of the theoretical cut-off of the white dwarf luminosity function is not affected by the adopted metallicity law, no matter if the adopted metallicity law is that of Twarog (1980), that of Casagrande et al. (2011), or if a fixed value of the metallicity is adopted. This, in turn, means that the age estimate of the Solar neighborhood obtained from the location of the drop-off of the white dwarf luminosity function is robust. Actually, the age difference between the theoretical calculations is rather small. For instance, when the luminosity function of the SDSS is adopted, the age of the disk derived using the metallicity law of Casagrande et al. (2011) is obtained to be 9.5 Gyr. If the metallicity law of Twarog (1980) is used, however, the age turns out to be 10 Gyr, and if a fixed value of the metallicity equal to the Solar one is adopted, we obtain 9.8 Gyr. These ages when the adopted luminosity function is that of the SSS are 10 Gyr for the first two cases and 10.3 Gyr for the case in which a constant Solar metallicity with no dispersion is employed.

At first look, this result may seem surprising since at the luminosity of the cut-off contribute the oldest white dwarfs in the Galaxy. These white dwarfs have cooling ages, which are approximately equal to the age of the Galactic disk, and thus have negligible main-sequence lifetimes, which translates in small metallicities for the age-metallicity relationship of Twarog (1980). However, since these white dwarfs have progenitors with very short main sequence lifetimes, it also means that their progenitors are rather massive. Consequently, the steep slope of the initial mass function prevents the formation of a large number of these stars. On the contrary, the peak of the white dwarf luminosity function is dominated by white dwarfs of $\sim 0.6 \pm 0.05\, M_{\odot}$, which are the bulk of white dwarfs in our Solar neighborhood, and which have very different main sequence lifetimes (and metallicities). The net result is that the drop-off of the white dwarf luminosity function is very abrupt, and its position is mainly determined by otherwise typical white dwarfs. Additionally, for the case of the metallicity law of Casagrande et al. (2011), the relatively large dispersion of metallicities contributes to erase the metallicity dependence of stellar lifetimes and results in a negligible dependence of the position of the drop-off of the

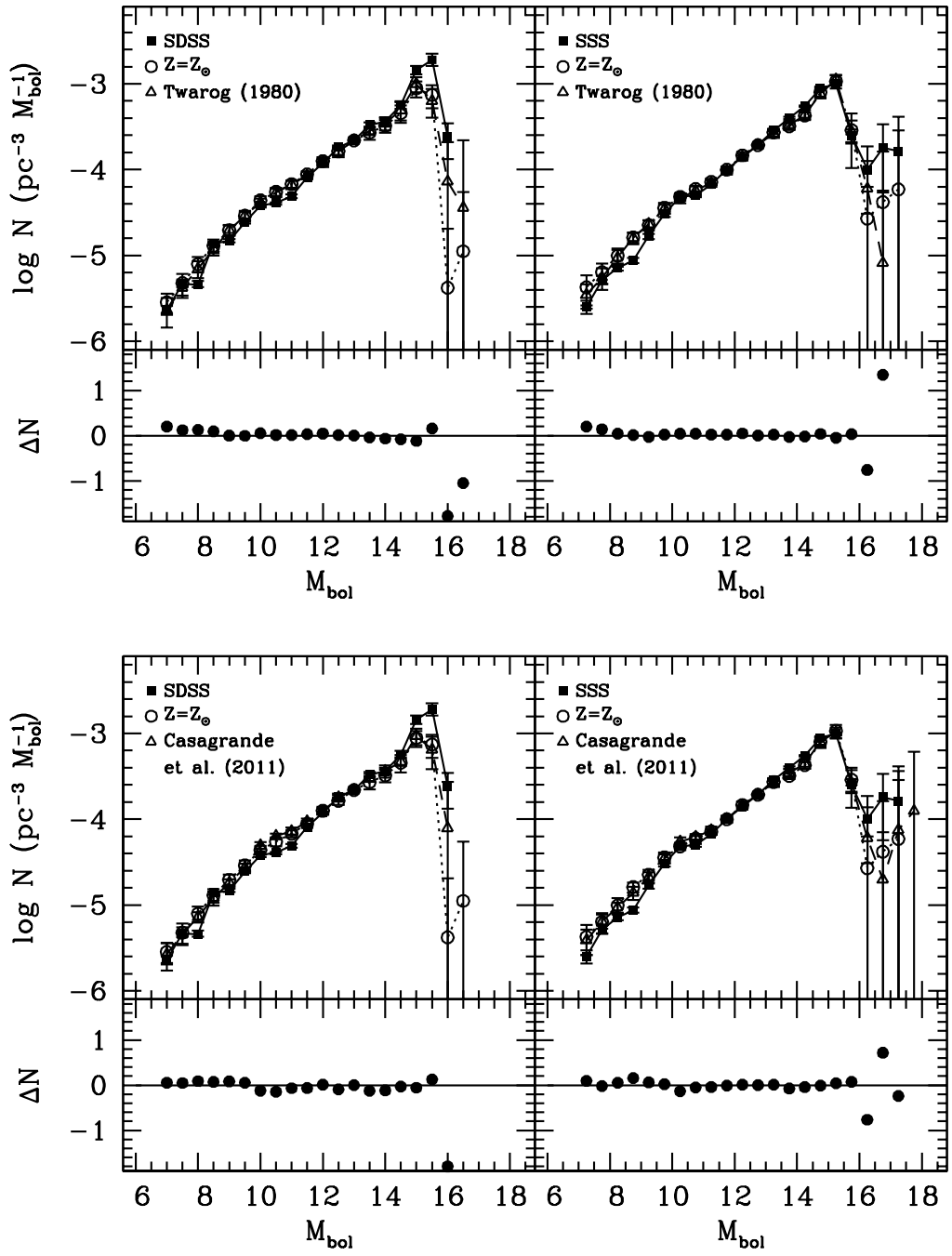

Figure 3.4: Simulated white dwarf luminosity function using the metallicity law of Twarog (1980) (top panels) and that of Casagrande et al. (2011) (bottom panels) compared to the observational white dwarf luminosity functions of Harris et al. (2006) (left panels) and Rowell & Hambly (2011) (right panels). As in previous figures, we also show the residuals between the synthetic luminosity functions computed with a given metallicity law, and the luminosity function computed adopting the Solar value (see text for details).

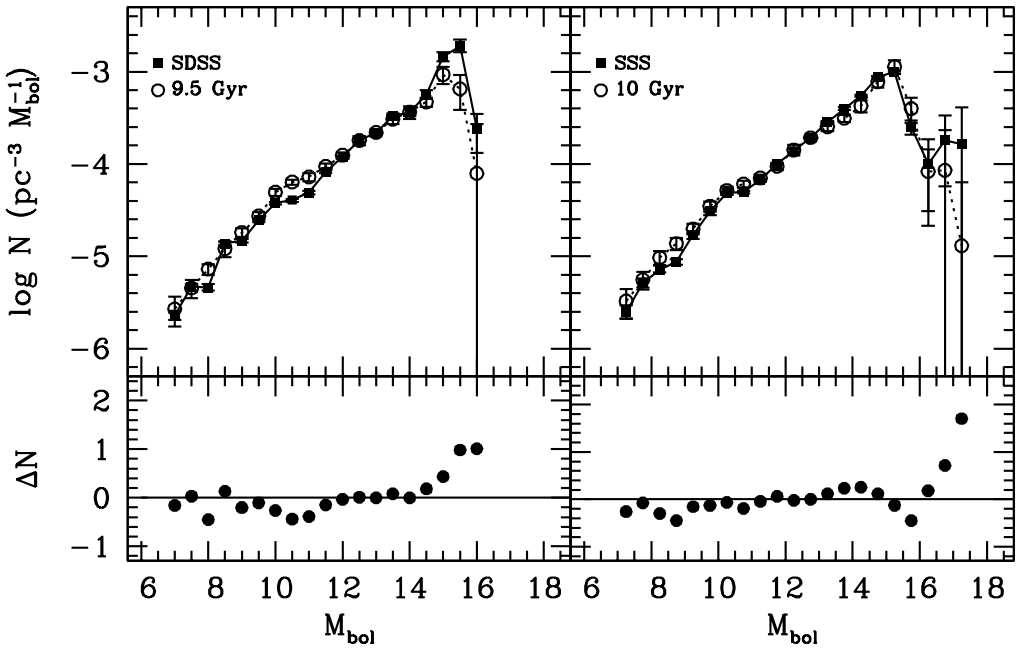

Figure 3.5: Simulated white dwarf luminosity functions using the very recent metallicity law of Casagrande et al. (2011), compared to the observed luminosity functions of the SDSS (left panel) and the SSS (right panel). The adopted disk ages are 9.5 and 10.0 Gyr, respectively, which are the ages that best reproduce the position of the observed cut-off of the luminosity function. As done in previous figures, we also show the corresponding residuals.

white dwarf luminosity function on the metallicity of white dwarf progenitors.

Given that the position of the cut-off of the theoretical white dwarf luminosity function does not depend on the adopted metallicity law, we computed the age of the disk that best fits the observed distribution of white dwarfs. The resulting white dwarf luminosity functions are displayed in Fig. 3.5, and the corresponding ages are 9.5 Gyr for the case in which the white dwarf luminosity function of the SDSS is employed, while we obtain 10.0 Gyr when the luminosity function of the SSS is adopted. Thus, currently, the age determination of the Galactic disk using the cut-off of the white dwarf luminosity function seems to be dominated by the relatively small number of white dwarfs in the lowest luminosity bins. A comparison of the SDSS and SSS luminosity functions indicates that this introduces an uncertainty of ~ 0.5 Gyr.

3.5 Summary and conclusions

In this chapter we explored the possible dependence of the white dwarf luminosity function on the adopted age-metallicity relationship. Our motivation for undertaking such a study was that most age estimators depend on the metallicity of the adopted theoretical stellar evolutionary models, and such a study was lacking for the case in which the age of the Galactic disk is estimated using the position of the cut-off of the white dwarf luminosity function. Our study fills this gap. In doing so, we used an up-to-date Monte Carlo simulator, which incorporates the most recent and reliable prescriptions for both the main sequence lifetimes and cooling ages, as well as the most realistic Galactic inputs. We also adopted two typical and frequently used metallicity laws, the first one being the classical age-metallicity relationship of Twarog (1980), which displays a monotonically increasing trend, and the metallicity law of Casagrande et al. (2011), which does not increase as time passes by, but instead shows a relatively large dispersion around the Solar value. Nevertheless, before studying the role of the adopted age-metallicity relationship, we also studied other possible effects that may eventually have a noticeable impact on the shape of the white dwarf luminosity function. Specifically, we studied how the ratio of non-DA to DA white dwarfs influences the shape of the luminosity function and of its cut-off and also how the choice of the adopted theoretical degenerate cooling sequences affects the luminosity function. We found that neither the shape of the bright portion of the white dwarf luminosity function nor the position of its downturn at low luminosities are noticeably affected by these inputs. More importantly, we also found that the adopted age-metallicity relationship has a negligible impact on the shape of the luminosity function and on the position of its drop-off. Hence, the age estimates of the Galactic disk obtained from the number counts of low-luminosity white dwarfs are robust, and the age differences mainly come from the way in which low-luminosity white dwarfs are culled to obtain a nearly complete sample. For the two most recent observational determinations of the white dwarf luminosity function – namely, that of Harris et al. (2006), which was obtained from white dwarfs found in the SDSS – and that of Rowell & Hambly (2011), which was derived using data from the SSS – we obtain 9.5 Gyr and 10.0 Gyr, respectively.

Chapter 4

The LSS-GAC DA white dwarf luminosity, mass and cumulative age functions

4.1 Introduction

The LAMOST (Large Sky Area Multi-Object Fiber Spectroscopic Telescope) Spectroscopic Survey of the Galactic anti-center (LSS-GAC) follows a well-defined selection criteria aiming at providing spectra for stellar sources of all colors in the Galactic anti-center (including white dwarfs) so that they can be studied in a statistically meaningful way (Liu et al., 2014). LSS-GAC started operations in 2011 and will provide a significantly larger sample of white dwarfs than those within 20 pc of the Sun. In this chapter we derive preliminary observed luminosity, mass and cumulative age functions of white dwarfs identified within the first data release of LSS-GAC, and use our state-of-the-art Monte Carlo population synthesis code adapted to the characteristics of the survey to simulate the white dwarf population in the Galactic anti-center. We apply the LSS-GAC selection criteria to the simulated samples, carefully evaluate all possible observational biases, and derive synthetic luminosity, mass and cumulative age functions. This exercise allows us to perform a meaningful comparison between the outcome of simulations and the observational data.

We first offer a description of the observed sample of white dwarfs from the LSS-GAC Data Release (DR) 1 in Section 4.2 and in Section 4.3 we detail how the observational white dwarf luminosity, mass and cumulative age functions are computed. In Section 4.4 we review our numerical setup, describe the parameter models that we test and present the obtained theoretical white dwarf luminosity, mass and cumulative age functions. In Section 4.5 we perform a comparison between the theoretical functions that we obtain from the different models and also compare our findings to other observational functions. We also discuss the potential effect of

3D atmosphere corrections or double degenerate mergers on the white dwarf mass function and present the deduced DA white dwarf birth rate. Finally, in Section 6.6, we summarize our calculations and present our conclusions.

4.2 The observational sample

The LSS-GAC is an important component of the LAMOST Galactic survey (Cui et al., 2012). Targets are selected uniformly and randomly in $(r, g-r)$ and $(r, r-i)$ Hess diagrams, with a faint limiting magnitude of $r = 17.8$ (18.5 for limited fields) – see Liu et al. (2014). This simple yet non-trivial target selection algorithm allows to study the stellar populations for any given type of target, such as white dwarfs. The LSS-GAC survey is centered on the Galactic anti-center ($|b| \leq 30\,\mathrm{deg}$, $150 \leq l \leq 210\,\mathrm{deg}$) and covers an sky area of over 3,400 deg^2. The g, r, i magnitudes of the LSS-GAC targets were obtained by the Xuyi Schmidt Telescopic Photometric Survey of the Galactic anti-center (XSTPS-GAC), which targeted ∼100 million stars under an area of about 5,400 deg^2 covering the LSS-GAC survey footprint (Liu et al., 2014).

In constructing the LSS-GAC white dwarf sample, two independent but complementary routines were used Rebassa-Mansergas et al. (2016b). The first is the χ^2-template fitting method described in Rebassa-Mansergas et al. (2010), which selected white dwarfs based on χ^2 and signal-to-noise (S/N) ratio constraints. The second method selected white dwarfs by applying the color cut of Girven et al. (2011) to the $g-r$ and $r-i$ XSTPS-GAC colors of all LSS-GAC targets. This resulted in a total number of 107 LSS-GAC white dwarfs, of which 92 are DA white dwarfs. Internal tests indicated that the LSS-GAC DA white dwarf sample is ∼95% complete. Effective temperatures and surface gravities could be confidently determined for 75 out of the 92 DA white dwarfs following the Balmer-line fitting routine described in Rebassa-Mansergas et al. (2007). These 75 DA white dwarf constitute the observed sample that will be used throughout this work. For stars cooler than $\sim 12,000$ K, the 3D corrections of Tremblay et al. (2013) were employed. We finally interpolated these values in the tables from Renedo et al. (2010) and Althaus et al. (2005a) and Althaus et al. (2007) and masses, cooling ages, absolute magnitudes G, R, I and bolometric magnitudes (M_{bol}) were obtained, thus forming our observed sample. Distances were finally obtained from the distance moduli of the targets, also accounting for extinction (Chen et al., 2014).

Taking into account that this is a magnitude-limited survey, a correction must be applied when computing the luminosity and mass functions. For this we used a variant of the classical $1/V_{\mathrm{max}}$ method (Green, 1980), modified to take into account the fact that each of the 16 spectrographs on every LSS-GAC plate has a different magnitude limit (Liu et al., 2014). The resulting luminosity function is presented in Fig. 4.1, and is compared to several recent white dwarf luminosity functions from

different authors, showing in general a good agreement. The mass function is presented in Fig. 4.2. Three features can be identified. Firstly, a noticeable peak around $0.6\,M_{\odot}$, and secondly two broad features, one at $0.4\,M_{\odot}$ presumably attributed to binary interactions and another one at $1\,M_{\odot}$, which could be a consequence of white dwarf binary mergers (see Section 4.4.2).

4.3 Computing the observed DA white dwarf luminosity function, mass function and formation rate

Magnitude-limited surveys such as the LSS-GAC survey are affected by selection effects. Therefore, any parameter distribution that results from the analysis of a given observed population is subject to observational biases. The $1/V_{\rm max}$ method described in Schmidt (1968) and Green (1980) is aimed at removing these biases. In our case this is done calculating the maximum volume in which each of the white dwarfs in the sample would have been detected given the magnitude limits of the LSS-GAC survey. This requires considering the lower and upper magnitude limits of each of the 16 spectrographs of each LSS-GAC plate. For each spectrograph, the lower and upper magnitude limits define respectively the minimum ($d_{\rm min}$) and maximum ($d_{\rm max}$) distances (and therefore minimum and maximum volumes, $V_{\rm min}$ and $V_{\rm max}$, respectively) at which the considered white dwarf would have been detected. The total maximum volume of a white dwarf, $V_{\rm WD}$, is the sum over the individual maximum volumes obtained from each spectrograph – see also Hu et al. (2007) and Limoges & Bergeron (2010):

$$V_{\rm WD} = V_{\rm max} - V_{\rm min} = \sum_{i=1}^{n_{\rm spec}} \frac{\omega_i}{4\pi} \int_{d_{\rm min}}^{d_{\rm max}} e^{-z/z_0}\ 4\pi r^2 dr = $$
$$= -\sum_{i=1}^{n_{\rm spec}} \frac{z_0 \times \omega_i}{|\sin b|} \left[\left(r^2 + \frac{2z_0}{|\sin b|} r + \frac{2z_0^2}{|\sin b|^2} \right) e^{-\frac{r|\sin b|}{z_0}} \right]_{d_{\rm min}}^{d_{\rm max}} \qquad (4.1)$$

where b is the Galactic latitude of the white dwarf, and ω_i is the solid angle in steradians covered by each spectrograph ($1.2\ \deg^2 \times \pi^2/180^2$; $\sum_{i=1}^{n_{\rm spec}} \omega_i$ is the total area observed by the survey, also in steradians). The factor e^{-z/z_0} takes into account the non-uniform distribution of stars in the direction perpendicular to the Galactic disc (Felten, 1976), where $z = r \times \sin(b)$ is the distance of the white dwarf from the Galactic plane, and z_0 is the scale height, which is assumed to be 250 pc (Liebert et al., 2005a; Hu et al., 2007). In the cases where two or more spectrographs observe the same region of sky, we consider the overlapping region with the largest volume, spanning between the smallest lower magnitude limit and the highest upper magnitude limit of the overlapping spectrographs.

Once $V_{\rm WD}$ is calculated for each white dwarf in the observed sample the space density of white dwarfs is simply obtained as $\sum 1/V_{\rm WD} = 0.83 \pm 0.16 \times 10^{-3}$ pc^{-3}, where the summation is over all the white dwarfs in the sample. The error of the space density was obtained artificially producing 200 versions of the observed luminosity function by varying the value of the function in each bin with a random value sampled from a Poisson distribution proportional to the error bar corresponding to that bin. However, it has to be noted that the space density derived here represents an absolute lower limit, as we are able to derive reliable stellar parameters for only 75 of the 92 DAs in our sample. That is, we are considering just 81 per cent of the observed sample in the analysis. Moreover, the lowest effective temperature value among LSS-GAC DA white dwarfs is ∼6,500 K. White dwarfs of lower effective temperatures are too faint to be detected by the survey, and are therefore not accounted for in our calculation of the space density. The space density as a function of the bolometric magnitude $M_{\rm bol}$, mass $M_{\rm WD}$ and cooling age $t_{\rm c}$ yield the white dwarf luminosity, mass and age functions, respectively. Each of these functions is analyzed in the following sub-sections.

The $1/V_{\rm max}$ method described above can be also used to quantify the completeness of the observed sample, i.e. the percentage of white dwarfs that are still missing because of selection effects after applying the $1/V_{\rm max}$ method. This completeness must not be taken as the spectroscopic completeness of the LSS-GAC sample, which is 95% (see Section 4.2). If the sample is complete, then the average value $\langle V - V_{\rm min}\rangle/\langle V_{\rm max} - V_{\rm min}\rangle$ should be 0.5 (Green, 1980). In this expression V is the volume of the white dwarf as defined by its distance, i.e. the same as Eq. (4.1), but integrating from 0 to d. In our case this quantity is 0.4, which corresponds to a completeness of 80%. Of course, the above derived estimate of the completeness is within the context of the magnitude limits of the LSS-GAC survey, i.e. it does not account for populations of white dwarfs that are too faint/rare to make it into the observed sample. Moreover, a 19% of the observed sample has not been considered in the analysis. If we were able to constrain the stellar parameters of these white dwarfs, then the completeness would increase.

4.3.1 The luminosity function

The LSS-GAC white dwarf luminosity function is shown in Fig. 4.1, its associated errors are calculated following Boyle (1989). For comparison we show the luminosity functions obtained by De Gennaro et al. (2008) for the SDSS survey, Torres et al. (2014) for hot DAs in the SDSS – which supersedes the luminosity function of Krzesinski et al. (2009) – and the luminosity function of Giammichele et al. (2012) for a local and volume limited sample of white dwarfs. We note that two more luminosity functions are available from the SDSS. Harris et al. (2006) derived a luminosity function for photometric white dwarf candidates, and Hu et al. (2007) did the same for Data Release 1 DA white dwarfs. However, we do not show them in

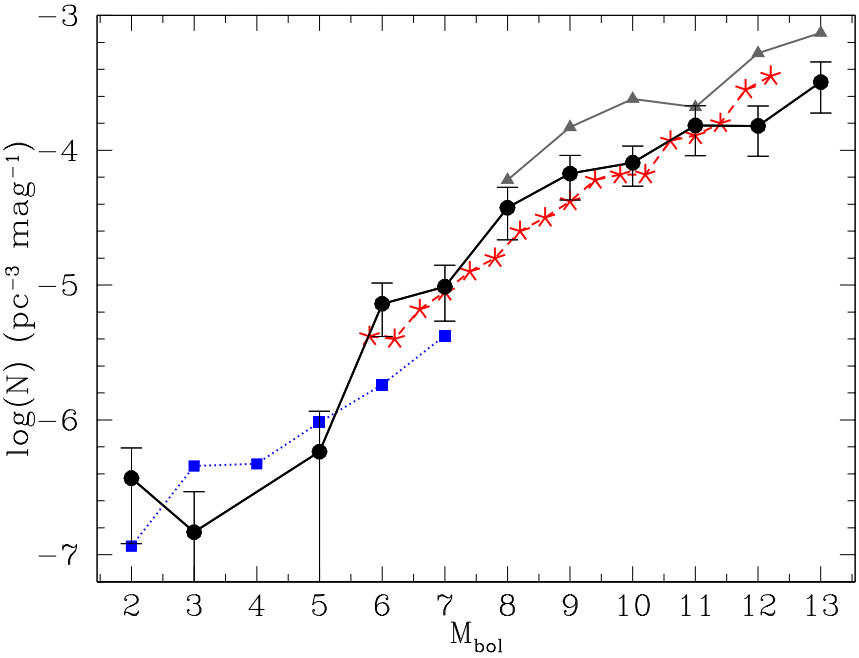

Figure 4.1: The luminosity function of LSS-GAC DA white dwarfs and associated errors – solid black line and solid dots. For the sake of comparison we also show the luminosity functions obtained by De Gennaro et al. (2008) – red dashed line and red stars – Torres et al. (2014) – blue dotted line and blue squares – and Giammichele et al. (2012) – solid gray line and gray triangles.

Fig. 4.1 because firstly the luminosity function of Harris et al. (2006) assumes $\log g = 8$ dex for all white dwarfs in the sample, and moreover, it very much resembles the one of De Gennaro et al. (2008) when considering DA white dwarfs of the same value of $\log g$, and secondly the work of De Gennaro et al. (2008) supersedes the analysis of Hu et al. (2007). Moreover, we decided not to show the luminosity functions obtained by Liebert et al. (2005a) for the Palomar Green Survey and Limoges & Bergeron (2010) for the KISO survey, as they also resemble the luminosity function of De Gennaro et al. (2008) but contain considerably fewer objects. Because of completeness issues, the luminosity function derived by Rowell & Hambly (2011) for white dwarf candidates in the Super-Cosmos survey is not included neither. To avoid clustering of data in Fig. 4.1 we have also opted not to show the errors of all the above mentioned luminosity functions.

Inspection of Fig. 4.1 reveals that, for $M_{\rm bol} \geq 6$ mag, the luminosity function derived in this work is in good agreement with the luminosity function of De Gennaro et al. (2008). The apparent disagreement between our luminosity function and the

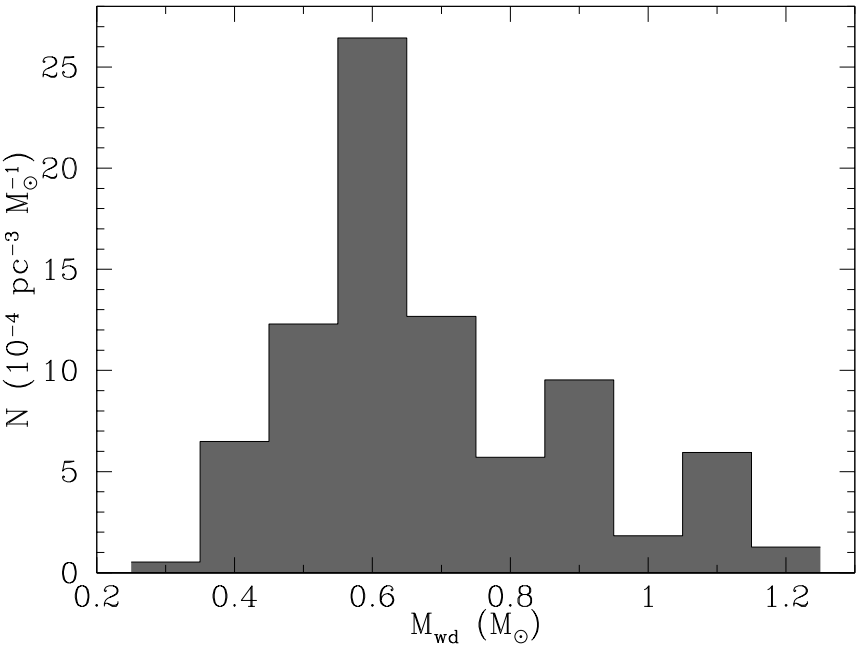

Figure 4.2: The mass function of LSS-GAC DA white dwarfs.

one obtained by Giammichele et al. (2012) is likely due to the fact that the latter study includes all white dwarfs (not only DAs) in a volume-limited local sample which does not presumably suffer from completeness issues, and therefore the space density is higher. For $M_{\rm bol} < 6$ mag, our luminosity function is also in broad agreement with that of Torres et al. (2014) for hot DAs. However, the number of LSS-GAC white dwarfs falling in these bins is too small for a meaningful comparison between the two studies. It should be also noted that the white dwarf luminosity function actually continues to fainter magnitudes than those shown in Fig. 4.1, however we do not display those bins as these objects are too faint to be present in the LSS-GAC sample.

4.3.2 The mass function

The mass function of the LSS-GAC white dwarfs is displayed in Fig. 4.2. As expected, it shows a clear peak around 0.6 $M_\odot$. A relatively high percentage ($\sim 10\%$) of low-mass ($<0.5\,M_\odot$) white dwarfs can also be seen. Traditionally, the existence of these low-mass white dwarfs has been attributed to binary interactions (Liebert et al., 2005a), and indeed it has been demonstrated that the majority of low-mass white dwarfs are formed in binaries (Rebassa-Mansergas et al., 2011; Kilic et al., 2012).

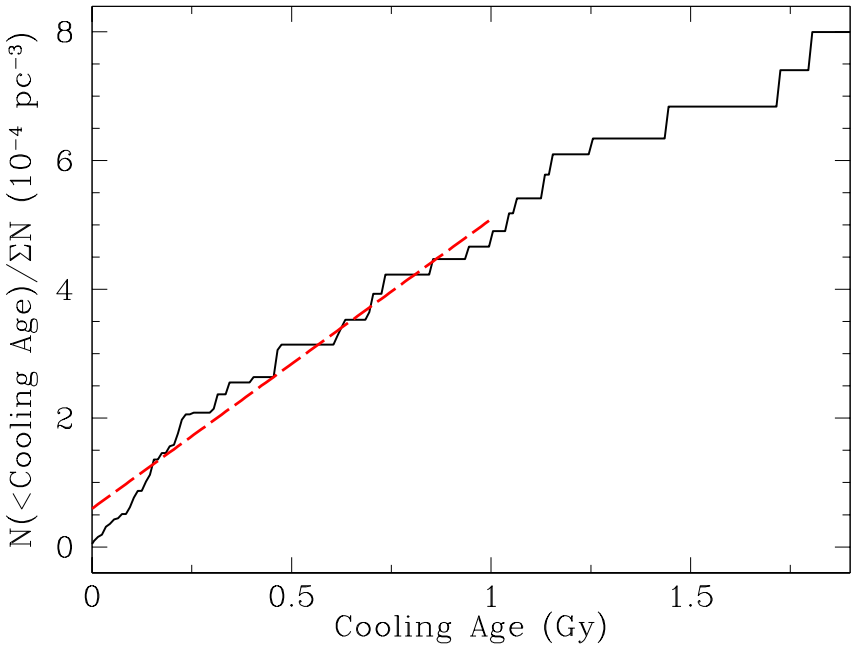

Figure 4.3: The LSS-GAC DA white dwarf cumulative age function. The slope of a straight line fit to the last Gyr (red dashed line) gives the average DA white dwarf formation rate.

Therefore, DA white dwarfs in those low-mass bins are expected to be components of binaries that contain unseen companions. Inspection of Fig. 4.2 also reveals a large fraction ($\sim 30\%$) of massive ($\geq 0.8\,M_{\odot}$) white dwarfs. A high-mass feature has also been regularly detected in a number of studies (Liebert et al., 2005a; Kepler et al., 2007; Kleinman et al., 2013) and it has been claimed that it arises as a consequence of white dwarf binary mergers. Population synthesis studies however do not predict more than $\sim 10\%$ of the entire white dwarf population being the result of binary mergers (Han et al., 1994; Han, 1998; Meng et al., 2008; Toonen et al., 2012; García-Berro et al., 2012). Alternatively, a large number of high-mass white dwarfs in the mass function presented here may be the consequence of large uncertainties in the mass determinations (the mass errors of some of our objects are estimated to be larger than $0.1 - 0.15\ M_{\odot}$, which can move some objects across the corresponding mass bins). We will further discuss the large percentage of high-mass white dwarfs identified in our mass function in Section 4.5.4.

4.3.3 The formation rate of DA white dwarfs

We now estimate the average DA white dwarf formation rate following the method outlined by Hu et al. (2007). If the white dwarf formation rate is assumed to be constant during the last Gyr, then the slope of the cumulative age function (see Fig. 4.3) can be considered as the average formation rate. Thus, we simply fit the cumulative age function with a straight line (the red dashed line in Fig. 4.3), and identify the slope of $5.42 \pm 0.08 \times 10^{-13}$ pc^{-3} yr^{-1} of the fit as the DA white dwarf formation rate. Inspection of Fig. 4.3 reveals that, as expected, the maximum of the cumulative age function is 0.83×10^{-3} pc^{-3}, i.e. the total LSS-GAC DA white dwarf space density.

Numerous studies in the past two decades have obtained white dwarf formation rates. The most recent analysis (Verbeek et al., 2013) results in a birth rate of $5.4 \pm 1.5 \times 10^{-13}$ pc^{-3} yr^{-1}, in excellent agreement with the value estimated here. The formation rates derived by Hu et al. (2007), $2.5 - 2.7 \times 10^{-13}$ pc^{-3} yr^{-1}, Liebert et al. (2005a), 6×10^{-13} pc^{-3} yr^{-1}, and Holberg et al. (2002), 6×10^{-13} pc^{-3} yr^{-1}, are also broadly consistent with the value estimated here. For comparison, earlier studies yielded formation rates that are generally considerably higher – e.g., Green 1980, $20 \pm 10 \times 10^{-13}$ pc^{-3} yr^{-1}, Weidemann 1991, 23×10^{-13} pc^{-3} yr^{-1}, and Vennes et al. 1997, $8.5 \pm 1.5 \times 10^{-13}$ Â pc^{-3} yr^{-1}). This may be a consequence of the recent improvement in quality and size of white dwarf data sets. Planetary nebulae birth rates are also found to be higher in general – Ishida & Weinberger (1987), 80×10^{-13} pc^{-3} yr^{-1}, Phillips (2002), 21×10^{-13} pc^{-3} yr^{-1}, and Frew (2008), $8 \pm 3 \times 10^{-13}$ pc^{-3} yr^{-1}. The discrepancy has been discussed in detail in Liebert et al. (2005a).

4.4 The LSS-GAC simulated DA white dwarf luminosity, mass and cumulative age functions

In the previous sections we presented and characterized the observed LSS-GAC DA white dwarf sample. We also derived the DA white dwarf space density which is used to construct the luminosity and mass functions of DA white dwarfs. Finally, we estimated the DA white dwarf formation rate from the white dwarf cumulative age function. In this section we simulate the LSS-GAC DA white dwarf population and take advantage of the well-defined selection criteria employed by the LSS-GAC survey to evaluate the fraction of simulated white dwarfs that would have been observed by the LSS-GAC survey. This will allow us to directly compare the ensemble properties of the observational data sets with the outcome of the simulations (see Section 4.5).

4.4.1 Building the synthetic white dwarf sample

We provide here a brief description of the inputs for our Monte Carlo white dwarf population synthesis code adapted to reproduce the LSS-GAC survey. A more complete and detailed description of the population synthesis code can be found in Chapter 2.

Stellar masses are sampled using the initial mass function (IMF) of Kroupa (2001) and the moment at which each star is born ($t_{\rm born}$) is obtained in accordance with a star formation rate (SFR), assumed to be constant unless specified otherwise. The position of each star is randomly generated from a double exponential distribution of a constant Galactic scale height of 250p̃c and a constant scale length of 3.5 kpc. The velocity distribution that we employ takes into account the differential rotation of the Galaxy, the peculiar velocity of the Sun and a scale height dependent dispersion law (Mihalas & Binney, 1981). Also, a metallicity value is assigned to each star according to a Gaussian metallicity distribution as presented in Casagrande et al. (2011).

In order to reproduce the LSS-GAC survey, stars are generated in a cone delimited by $-30 \leq b \leq 30^{\circ}$ in Galactic latitude and $150 \leq l \leq 210^{\circ}$ in Galactic longitude (Section 4.2), with no restriction in terms of distance from the Sun. However, we define a test cone of up to 200 pc in length, in which we interactively examine the density of generated stellar mass until we reach a limit density value for the local stellar population (Holmberg & Flynn, 2000). We scale this limit in order to obtain a final restricted white dwarf sample of the same order as the observed one.

Then we introduce a 9.5 Gyr age for the thin disk ($t_{\rm disk}$) and interpolate the main sequence lifetimes ($t_{\rm MS}$) of the generated stars using the BaSTI grids according to stellar mass and metallicity (Pietrinferni et al., 2004). We can compute the white dwarf mass using the mass of the progenitor with the help of an initial-to-final mass relation (IFMR), which will be further detailed in Section 4.4.2. We use the carbon-oxygen white dwarf cooling sequences of Renedo et al. (2010) and Althaus et al. (2010b) for $M_{\rm WD} < 1.1\,M_{\odot}$, and for white dwarf masses above this value we employ the tracks for oxygen-neon white dwarfs of Althaus et al. (2005a) and Althaus et al. (2007). Finally, we convert the $UBVRI$ magnitudes into the $ugriz$ (Jordi et al., 2006), taking into account the 3D Galactic extinction map of Chen et al. (2014) and the extinction coefficients of Yuan et al. (2013).

Some of the DA white dwarf stellar parameters derived from the fits to the LSS-GAC spectra are subject to relatively large errors. It is therefore necessary to account for those uncertainties in the simulated white dwarf populations before comparing the synthetic and observational data sets. The effective temperature errors of the observed sample, which show a modest increase with increasing temperature, were fitted by a third order polynomial such that the error for relatively cool ($\sim 10,000$ K) white dwarfs is about 300 K, increasing to $\sim 1,000$ K for white dwarfs as hot as $25,000$ K. We adopt this polynomial relation for deriving effective temperature er-

Table 4.1: The four models assumed in this work with the aim of reproducing the observed LSS-GAC DA white dwarf population. Model 1 is our standard model.

Model	SFR	IFMR	Slope for the massive regime
1	constant	Catalán et al. (2008)	0.1
2	constant	Catalán et al. (2008)	0.06
3	constant	Ferrario et al. (2005)	0.1
4	bimodal	Catalán et al. (2008)	0.1

rors of our simulated white dwarfs. The observational errors of $\log g$ cluster around ~ 0.2 dex, and we take this value as the surface gravity uncertainty of the synthetic white dwarfs. The values of effective temperature and surface gravity for each simulated white dwarf are re-defined considering a random value within the error range defined for the two quantities. We then interpolate new values of mass, luminosity, cooling age, and bolometric and absolute magnitudes from the redefined $T_{\rm eff}$, and $\log g$ values. This results in, for example, an average error in mass of $\sim 0.1\,M_{\odot}$ for our simulated white dwarfs. Photometric errors are also taken into account. They are directly derived from the photometric uncertainties associated with the XSTPS-GAC survey (Liu et al., 2014).

4.4.2 Models

As presented in Section 4.3, the observational sample exhibits several specific features that are clearly visible in the luminosity, age and cumulative age functions of the LSS-GAC white dwarf sample (Figs. 4.1, 4.2 and 4.3). We attempt to reproduce those features as best as possible by employing the above described Monte Carlo simulator.

Given the apparent excess of massive white dwarfs seen in the mass function (Fig. 4.2), we attempt to reproduce this feature focusing on three parameters of the simulations that are thought to affect the final white dwarf mass distribution, namely the SFR, the IFMR up to an initial mass of about 6 $M_{\odot}$ (the white dwarf CO-core production regime) and the slope of this (linear) relationship for the massive (ONe-core) white dwarf regime. We start with our fiducial model, from now on called Model 1, which uses a constant SFR, the piece wise linear IFMR of Catalán et al. (2008) for the CO white dwarf regime, and a 0.1 slope for the massive regime as proposed by Iben et al. (1997).

We then consider three additional models, in which we vary only one of the above three parameters with respect to Model 1. In Model 2 we employ a 0.06 slope of the IFMR for massive white dwarfs, as inspired by Weidemann (2005). In this work

Table 4.2: The synthetic white dwarf populations are passed through consecutive steps of filtering that gradually reduce the number of surviving objects. We show here an example for one of the 10 performed realizations of Model 2 (Table 4.1). In the last two columns we indicate the percentage of white dwarfs that survive respect to the previous step and the percentage of white dwarfs that survive respect to the initial population, respectively.

	Filter	$N_{\rm WD}$	%	%
	Initial sample	5507		
Step 1	Selection Criteria	1358	25	25
Step 2	GAC plates + mag. limits + fibre allocation	250	18	0.04
Step 3	S/N $\geq$5	105	42	0.02
Step 4	Completeness + spectral fit	81	77	0.015

it was suggested to use an unsteady IFMR. The reason for decreasing the value of the slope of the relationship is to expand the range of initial masses that can produce massive white dwarfs (over 1 $M_{\odot}$) in the hope of reproducing the observed excess of these white dwarfs. In order to ensure the continuity of the IFMR over the entire white dwarf mass range and to be consistent with the upper carbon-oxygen white dwarf mass limit, we consider that all stars with masses between 6 and 11 $M_{\odot}$ become white dwarfs of core masses ranging from 1.1 to 1.4 $M_{\odot}$, which neatly gives a 0.06 slope. Extending the mass range up to 1.4 $M_{\odot}$ is not correct, given that a white dwarf that massive would most likely explode (Ritossa et al., 1999), but for the purposes of the current test is an acceptable assumption. Model 3 uses the IFMR of Ferrario et al. (2005) for the carbon-oxygen regime, which, according to the authors, results in a better agreement with the white dwarf mass distribution as compared to when a linear fit is used. In Model 4 we use the bimodal SFR proposed by Rowell (2013) with two broad peaks at around 2 and 7 Gyr ago, which should favor an increase in the number of massive white dwarfs during the last 2 Gyr given their shorter main sequence lifetimes. For each model we perform 10 individual realizations, and we compute the ensemble average of all the relevant quantities. A summary of the input parameters used for each model is given in Table 4.1.

4.4.3 The selection function

Once the synthetic DA white dwarf samples have been obtained for the different models outlined in the previous section, it becomes necessary to evaluate which of those synthetic white dwarfs would have been observed by the LSS-GAC survey. Here, we describe how the selection process is performed.

The first step is to evaluate the effect of the LSS-GAC target selection criteria

(Section 4.2). This is done independently for each of the 10 realizations of each model. For this purpose, the g, r, and i magnitudes of all white dwarfs of a given synthetic population are embedded within the XSTPS-GAC photometric catalog and the selection criteria is then applied to the entire resulting population. The magnitude limits of the LSS-GAC survey are $14 \leq r \leq 18.5$ mag (Section 4.2), and within those limits the LSS-GAC criteria efficiently selects $80 - 85\%$ of the total simulated white dwarf population , depending on the model. This fraction increases to $85 - 90\%$ if we consider $14\,\mathrm{mag} \leq r \leq 18\,\mathrm{mag}$. The high success rate of selecting white dwarfs is not unexpected, considering that the LSS-GAC survey is specifically developed to efficiently target stars of all colors, including blue objects such as white dwarfs (Section 4.2).

In a second step we evaluate which of the simulated white dwarfs that are selected by the LSS-GAC criteria fall within the field of view ($5\,\mathrm{deg}^2$) of the LSS-GAC plates actually executed. If this is the case, an additional condition is that the simulated white dwarfs are required to fulfill the magnitude limits of the plates/spectrographs, otherwise they would not have been observed. In practice, we consider the distances between the position defined by the right ascension and declination of each simulated white dwarf and the central positions of the 16 spectrographs of the plate where the synthetic white dwarf falls (also defined by their right ascensions and declinations) and evaluate whether or not the r magnitude of the synthetic white dwarf is within the magnitude limits of the nearest spectrograph. If all those conditions are passed, we then consider the probability of a given target to be allocated a fiber (some fibers are used for sky observations). This probability is simply given by $N_{\mathrm{spec}}/(N_{\mathrm{spec}} + N_{\mathrm{sky}})$, and is generally $\sim$0.9. In this expression N_{spec} is the number of target spectra observed by the spectrograph, and N_{sky} is the number of fibers allocated for sky observations.

If the synthetic white dwarfs survive all the previously explained filtering we consider the LSS-GAC survey would have observed them. Therefore, in a third step we consider the probability for each simulated white dwarf to have a LAMOST spectrum of S/N ratio ≥ 5 in both the blue and red arms. For each synthetic white dwarf we calculate the fluxes from their associated g and r magnitudes, add and subtract a 5% of flux in each case and calculate the magnitudes that result from this exercise (g_+, g_- and r_+, r_-, where the suffixes + and $-$ indicate that we have added and subtracted the 5% of the corresponding flux). We then consider all targets observed by the corresponding spectrograph (i.e. the spectrograph where the simulated white dwarf falls) having $g_- < g < g_+$ and $r_- < r < r_+$, and calculate the median S/N ratio of their LSS-GAC spectra in the two bands. If no observed spectra are found satisfying the above magnitude ranges, or if one of the median S/N ratios < 5, the synthetic white dwarf is then excluded from the analysis. This exercise takes into account nigh-to-night variations of S/N ratio that may arise e.g. from varying observing conditions, as the S/N is evaluated specifically for objects observed during the same night with the same plate/spectrograph, and of similar

magnitudes as the simulated white dwarf of concern.

Finally, in a fourth step we take into account the spectroscopic completeness of the observed sample (the fraction of LSS-GAC DA white dwarfs that we have identified among all DA white dwarfs observed) as well as consider the fact that we are not able to obtain reliable stellar parameters for 19 per cent of the observed sample. We have estimated a completeness of $\sim 95\%$ (Section 4.2). Therefore we randomly exclude 5% of all synthetic white dwarfs that passed the previous filters. After this correction, we proceed by randomly excluding 19% of the surviving systems.

In order to minimize the effects of the random exclusion of synthetic white dwarfs, we repeat steps two to four 20 times per model realization. Given that each of the four models considered (Table 4.1) counts 10 realizations, we obtain 200 different final synthetic populations for each model. The number of simulated white dwarfs that pass the entire selection process described above vary slightly from model to model (and realization to realization) and yields synthetic samples of 65–85 objects, similar to the number of white dwarfs in the observed sample, 75 DA white dwarfs. An example of how the number of synthetic white dwarfs gradually decreases as they are passed through each of the filters of our selection process is shown in Table 4.2. In a final step we use bootstrapping techniques to produce synthetic samples of the same number of objects as the observed one. The final luminosity, mass and cumulative age functions for each model are the result of averaging the 200 individual functions derived from each of the independent realizations. These are shown in Figs. 4.5, 4.6 and 4.8, respectively, where we also include the luminosity, mass and cumulative age functions derived from the observational sample. A comparison of the synthetic and observed functions is presented and discussed in detail in the next section.

4.5 Discussion

In this section we compare the luminosity, mass and cumulative age functions (i.e. birth rates) that result from our numerical simulations to those derived observationally. Before comparing in detail the numerical and observed functions, we compare the white dwarf populations obtained from each of the models employed here. We also estimate the number of DA white dwarfs that the LSS-GAC will eventually observe.

4.5.1 The final expected number of LSS-GAC DA white dwarfs

The LSS-GAC selection criteria (Section 4.2) applied to our simulated white dwarf populations results in $\sim$ 80-85% of the synthetic DA white dwarfs falling within the magnitude limits of the survey being selected for observations (Section 4.4.3). The total number of white dwarfs generated by each model oscillates between 3,800 and 3,900, which reduces to 2,130–2,160 if we consider the magnitude limits of the

LSS-GAC. This implies that, on average, ∼1,700-1,850 DA white dwarfs could be potentially observed at the end of the survey, depending on the assumed model.

We have shown that ∼ 50% of our synthetic DA white dwarfs would have S/N≥5 if observed by the LSS-GAC (see Table 4.2). This percentage is expected to increase up to ∼2/3 for the data release 2 (and subsequent releases) of LSS-GAC spectra. The number of LSS-GAC DA white dwarfs expected to have spectra of S/N≥5 at the end of the survey is thus $N_{\rm DA}$ =(1,700–1,850 − $N_{\rm obs}$) × 2/3 ≃ 1,070–1,170, where $N_{\rm obs}$ = 92, i.e. the number of currently observed DA white dwarfs. Considering spectroscopic completeness and spectral fitting effects (Section 4.4.3, Table 4.2), which exclude ∼ 25% of the DA white dwarf spectra with S/N≥5, the final number of LSS-GAC DA white dwarfs with available and reliable stellar parameters at the end of the survey is expected to be ≃800–875, i.e. approximately one order of magnitude higher than the current number of observed LSS-GAC DA white dwarfs with reliable stellar parameters.

4.5.2 Effects of observational uncertainties

We have employed four different models to simulate the white dwarf population in the Galactic anti-center with the aim of constraining what set of assumptions (SFR, IFMR,. . .) fits better the observational data. As expected, the intrinsic properties of the simulated populations differed from model to model. However, these properties are changed when the observational uncertainties are incorporated (Section 4.4.1). For example, the simulated mass distributions become broader and lose detail, and more importantly, peak at larger values – for instance, for Model 2 the median of the distribution shifts from 0.57 $M_{\odot}$ to 0.60 $M_{\odot}$). Hence, incorporating observational uncertainties results in less prominent differences between the synthetic white dwarf parameter distributions.

This is more accentuated when we take into account the selection biases. In order to illustrate these effects together, in Fig. 4.4 we show the correlations between the effective temperatures, masses, cooling ages and distances for the synthetic population (red stars) and compare them to those obtained from the observational sample (black dots). For the sake of clarity we chose one typical realization of our Model 1, although very similar results are obtained for the rest of the realizations and models. It becomes obvious that the model reproduces well the observational data, and that the correlations between the considered parameters follow the same pattern as the observational ones.

4.5.3 The luminosity function

Fig. 4.5 shows the luminosity functions derived from our simulated samples, as well as that deduced from the observational data. The uncertainties in the simulated functions were derived in the same way as it was done for the observed

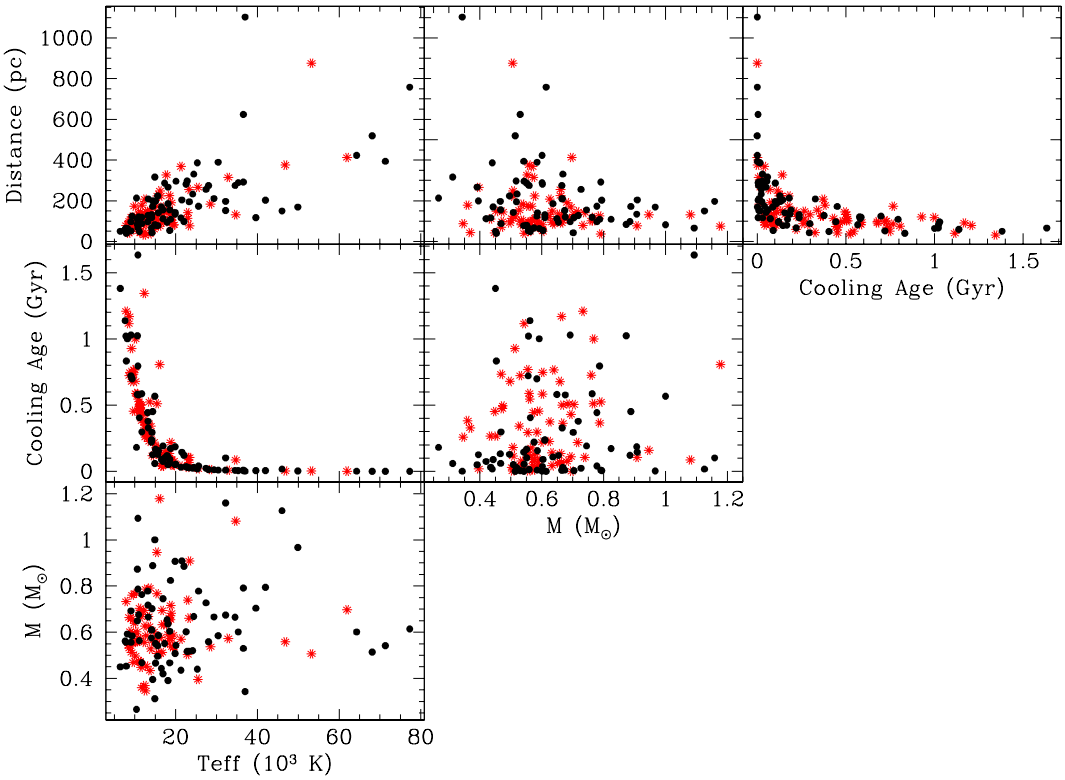

Figure 4.4: Effective temperatures, masses, distances and cooling ages correlations of the 75 LSS-GAC DA white dwarfs (black dots) compared to those of a typical realization of our Monte Carlo simulatior described in Section 4.4 (red stars). As can be seen, the degree of overlap of the synthetic sample and the observational one is excellent in all six panels.

one (Section 4.3.1). The space densities obtained for models 1, 2, 3 and 4, are 0.96 ± 0.19, 0.98 ± 0.21, 1.16 ± 0.20 and $1.06 \pm 0.20 \times 10^{-3}$ pc^{-3}, respectively. Although these values are slightly larger than the space density derived from the observations ($0.83 \pm 0.16 \times 10^{-3}$ pc^{-3}, they perfectly agree within the observational errors. It is evident that there is an overall good agreement (within the error bars) between the simulated and the observed luminosity functions, except at $M_{\rm bol}$ 2 and 6 mag, where the observed luminosity function predicts a considerably larger space density. It has to be noted, however, that the number of targets falling within bins of $M_{\rm bol} < 7$ mag is small (18% of the total observed sample). Hence, the observed luminosity function in those high luminosity bins is subject to low number statistics and the apparent increase of the observed luminosity function at those specific bins should be taken with some caution. A further inspection of Fig. 4.5 reveals that, because of the reasons explained above (Section 4.5.2), no model seems to have an

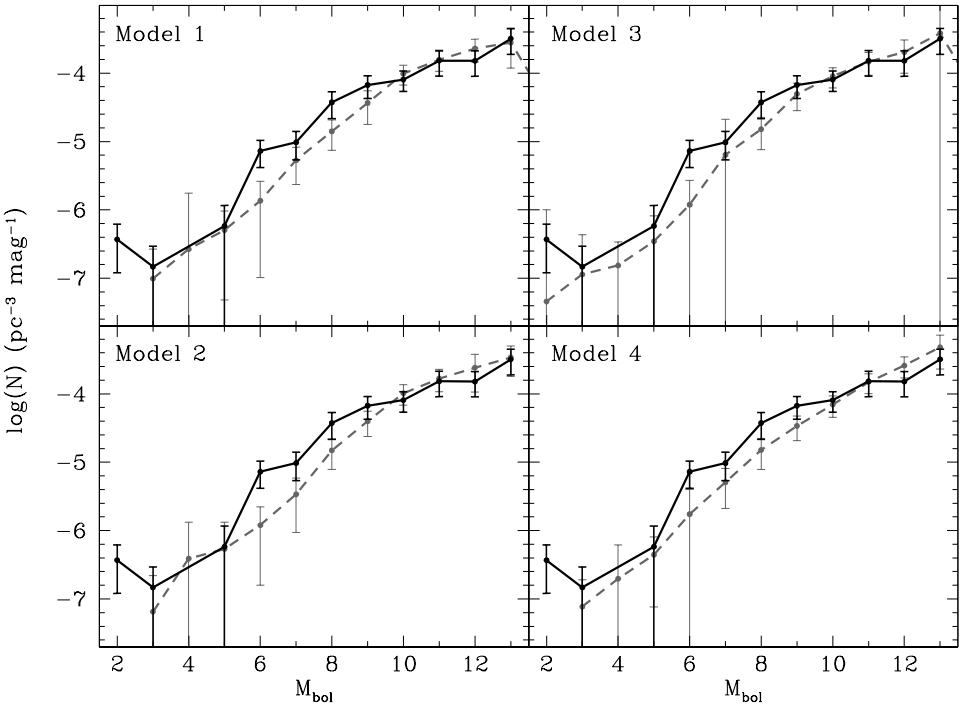

Figure 4.5: Simulated DA white dwarf luminosity functions (gray solid lines) for the models considered in Section 4.4.2 – see Table 4.1. The observed LSS-GAC white dwarf luminosity function is shown by the black solid line.

obvious advantage over the rest of models in reproducing the observational data.

4.5.4 The mass function

After applying the LSS-GAC target selection criteria and the target selection process described in Section 4.4.3 to our simulated populations, the mass functions yielded by all simulations are rather similar (Fig. 4.6). In addition, synthetic (single) white dwarfs of masses as low as $0.35\,M_{\odot}$ are now possible as a consequence of incorporating observational uncertainties. This effect partly explains the apparent over-abundance of low-mass ($\lesssim 0.45\,M_{\odot}$) white dwarfs in the observed mass function (black solid line in Fig. 4.2). Alternatively, a relative large fraction of low-mass white dwarfs in the observed sample could be the result of binary star evolution (Rebassa-Mansergas et al., 2011). The companions are likely to be cooler and/or more massive white dwarfs, or low-mass late-type main sequence stars, although other exotic companions such as brown dwarfs cannot be ruled out.

It is also clear that none of our models manages to completely reproduce the observed behavior at high mass bins, i.e. the fraction of massive white dwarfs (>

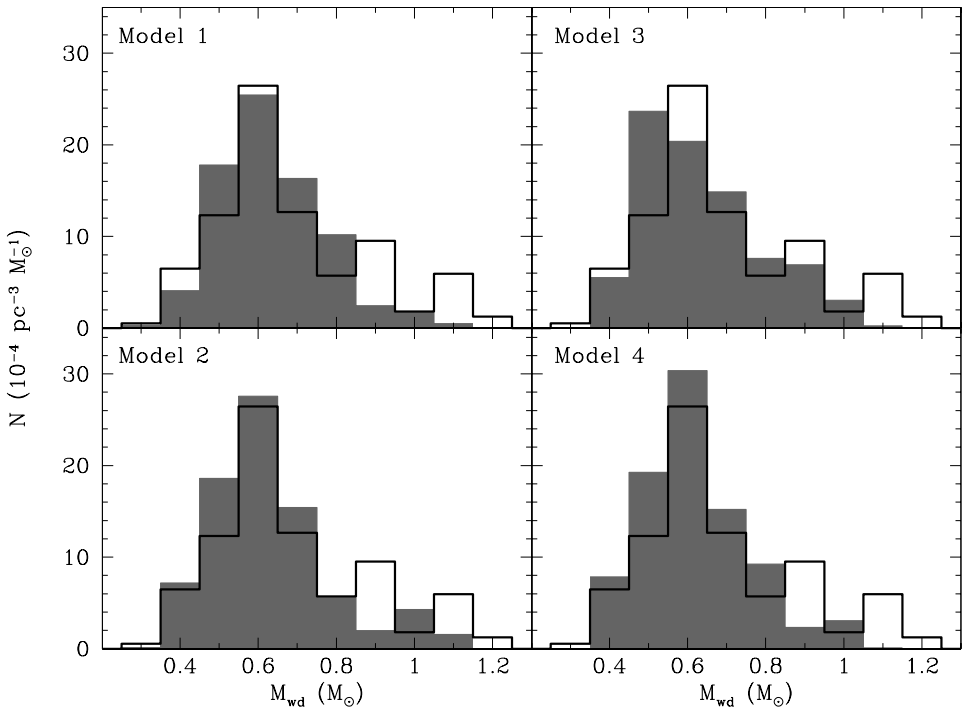

Figure 4.6: Simulated DA white dwarf mass functions resulting from the four models considered (gray histogram) compared with the observed LSS-GAC white dwarf mass distribution (white histogram).

$0.8\,M_\odot$) relative to those of typical mass ($0.6\,M_\odot$). This fraction is larger in the observed sample (a fraction of 0.29 for the observed sample while models 1 to 4 have fractions of 0.18, 0.16, 0.21 and 0.16, respectively). We discuss possible explanations of this feature below.

4.5.5 The initial-to-final mass relation

The currently available IFMRs have been derived from observational data that exhibit a large scatter in the initial-to-final mass diagram – see, for example, Fig. 1 of Catalán et al. (2008). In one of our models we have investigated the effect of varying the slope of the IFMR for producing a wider range of massive white dwarfs (see Section 4.4.2 and Table 4.1). We have also explored the effect of employing the IFMR of Ferrario et al. (2005). To further investigate the impact of the large scatter in the initial-to-final mass diagram to the simulated mass function, two additional models (Models 5 and 6) that take into account the error bars of the IFMR of Catalán et al. (2008) have been considered. In this way the IFMR is virtually moved "up" in one model and "down" in the other model. The remaining free parameters of Models

5 and 6 are the same as for our standard model (Table 4.1). The results show that the mass functions obtained from these two models do not differ significantly from those shown in Fig. 4.6 and are therefore unable of reproducing the high-mass excess present in the observed mass function.

4.5.6 S/N ratio and 3D model atmosphere correction effects

Two additional plausible explanations for the large fraction of massive white dwarfs observed are effects of limited S/N ratios and 3D model atmosphere corrections. We discuss them in the following paragraphs.

The LSS-GAC spectra considered in this work have a minimum S/N ratio of 5. It is therefore possible that some systematic uncertainties in the white dwarf stellar parameters result as a consequence of the relatively low S/N ratio of some white dwarf spectra. This may lead to the masses of some white dwarfs being overestimated. In order to investigate this possibility we re-derive the observed mass function excluding all systems with spectra having a S/N ratio below 8. This leaves us with 56 DA white dwarfs. We decided not to increase the S/N threshold to larger values because otherwise the number of massive (fainter and with systematically lower S/N ratios) white dwarfs that would survive the cut would be severely reduced. The mass function that results from this exercise does not differ significantly from the one obtained using the full sample, and displays a large fraction of massive white dwarfs as well. Therefore, the S/N ratio effects are unlikely the cause of the observed excess of massive white dwarfs.

The DA white dwarf sample analyzed in this work includes cool white dwarfs for which we have applied the 3D model atmosphere corrections to their stellar parameters deduced from 1D model atmosphere fitting. This provides us with the effective temperature and surface gravity, hence with their mass. If those corrections are somehow incorrect, they may lead to an apparent overabundance of massive white dwarfs. To explore this possibility we re-derived the mass function excluding all white dwarfs in our sample with an effective temperature below $13,000\,\mathrm{K}$. This results in a sub-sample of 60 DA white dwarfs. The mass function deduced from this sub-sample again presents a clear overabundance of massive white dwarfs. We therefore find that the overabundance of massive white dwarfs is unlikely caused by the possible effects related to the 3D model atmosphere corrections.

4.5.7 Double degenerate mergers

An exciting possible explanation for the excess of high-mass white dwarfs in the observed mass function is that a relatively large fraction of those stars is the result of mergers of two low-mass white dwarfs (Marsh et al., 1997; Vennes, 1999). Although no population synthesis study hitherto predicts such a large fraction of high-mass white dwarfs as the outcome of white dwarf mergers (e.g. Han et al., 1994; Han,

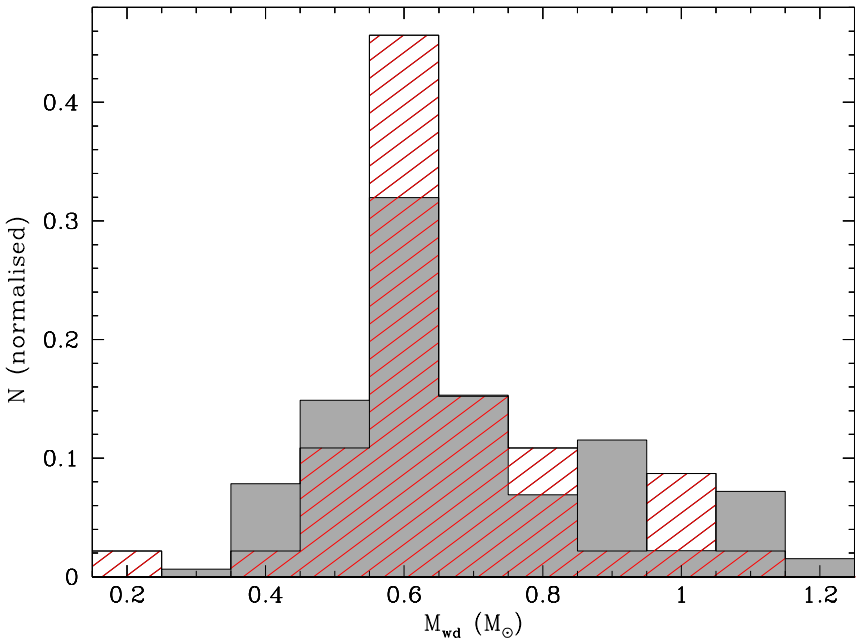

Figure 4.7: Normalized LSS-GAC DA white dwarf mass function (gray solid histogram) compared withe the normalized mass distribution of DA white dwarfs from the local and volume-limited sample of Giammichele et al. (2012) (red dashed histogram).

1998; Meng et al., 2008; Toonen et al., 2012), this scenario has been adopted in some of the previous observational studies (e.g. Liebert et al., 2005a; Giammichele et al., 2012). To further investigate this hypothesis we compare in Fig. 4.7 the normalized mass function obtained in this work with the normalized mass distribution of DA white dwarfs in the local, volume-limited sample of Giammichele et al. (2012). In becomes obvious that the peak at $0.6\,M_{\odot}$ is less pronounced in our normalized mass function, an effect likely related to the fact that we are subject to larger observational uncertainties which broaden the distribution. Interestingly, whilst the high-mass peak in the normalized mass distribution of Giammichele et al. (2012) is found at $1\,M_{\odot}$, our normalized mass function shows two apparent peaks at the 0.9 and $1.1\,M_{\odot}$ bins, and reflects a scarcity of systems at the $1\,M_{\odot}$ bin. Although this discrepancy is likely due to our larger uncertainties, which are sufficient to shift objects across bins, both studies favor the hypothesis that an excess of massive white dwarfs seems to exist.

The large white dwarf merger rate suggested by the current work indicates that an even larger number of close white dwarf binaries may exist in the Galaxy that have not yet merged. Those close binaries could be a main source of gravitational waves to be detected by future facilities such as the space interferometer eLISA (Nelemans, 2013; Aznar-Siguán et al., 2014; García-Berro et al., 2005; Lorén-Aguilar

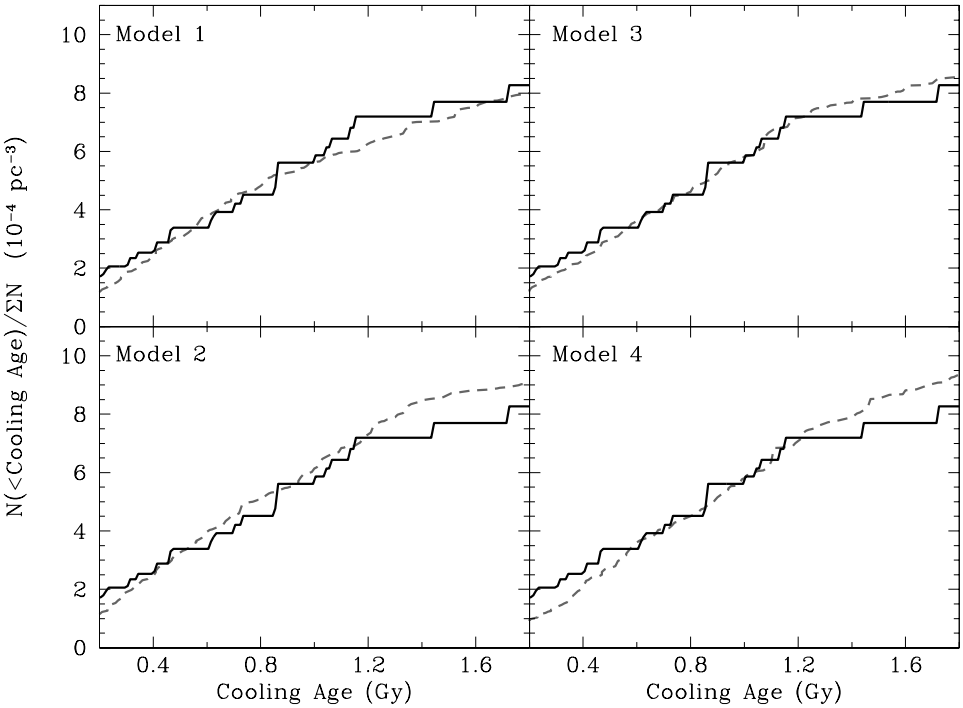

Figure 4.8: Simulated DA white dwarf cumulative age functions resulting from the four models considered (dashed line) compared with the LSS-GAC DA white dwarf cumulative age function (solid line).

et al., 2005). Therefore, indirect support in favor of the merger scenario may be obtained by analyzing the population of close double white dwarfs that eLISA will discover.

4.5.8 The average DA white dwarf formation rate

The cumulative age functions derived from our simulated populations are illustrated in Fig. 4.8, where the observed cumulative age function is also displayed. There is an overall good agreement between our simulations and the observations for cooling ages up to 1 Gyr, except perhaps for our model 4, which seems to systematically overestimate the space density for cooling age bins <0.4 Gyr (note that in model 4 we are employing a bimodal star formation rate). For cooling ages larger than 1 Gyr the discrepancies between the models and the observations arise due to the scarcity of white dwarfs at those specific cooling ages.

Fitting the simulated cumulative age functions with a straight line (see Section 4.3.3) we derive average DA white dwarf formation rates of 6.04±0.05, 6.42±0.05, 5.85±0.02 and 5.97±0.04 $\times 10^{-13}$ pc^{-3} yr^{-1} for models 1, 2, 3 and 4 respectively.

These values agree with the average formation rate derived from our observations within the errors ($5.42 \pm 0.08 \times 10^{-13}$ pc^{-3} yr^{-1}, see Section 4.3.3. Because of the observational uncertainties (Section 4.5.2), we find that no model seems to have an obvious advantage over the rest in reproducing the observational data.

4.6 Summary and conclusions

The recently initiated LAMOST Spectroscopic Survey of the Galactic anti-center, the LSS-GAC, selects targets for spectroscopic observations following a well-defined criteria. This significant advantage over previous surveys has allowed us to present a well-characterised magnitude-limited sample of 92 LSS-GAC hydrogen-rich (DA) white dwarfs from the data release 1. Our catalog is expected to be $\sim 95\%$ complete. We have determined the stellar parameters (surface gravity, effective temperature and mass), absolute and bolometric magnitudes, and distances of 75 DA white dwarfs. Taking into account volume corrections we have derived an absolute lower limit for the space density of DA white dwarfs of $0.83 \pm 0.16 \times 10^{-3}$ pc^{-3}. We have also obtained preliminary observed LSS-GAC DA white dwarf luminosity, mass and cumulative age functions. The luminosity function resembles those found in previous observational studies. The mass function reveals an excess of massive white dwarfs. Finally, the DA white dwarf formation rate derived from the cumulative age function is $5.42 \pm 0.08 \times 10^{-13}$ pc^{-3} yr^{-1}, in good agreement with other recent studies.

We have simulated the DA white dwarf population in the Galactic Anti-center using an existing Monte Carlo code adapted to the characteristics of the LSS-GAC survey. For this purpose, and specially aiming at reproducing the observed excess of massive white dwarfs, we have employed four different models. All those models take into account the observational uncertainties, both spectroscopic (i.e. we incorporate errors in the stellar parameters of our simulated white dwarfs based on the observational errors) and photometric. We find that the LSS-GAC criteria selects $\sim 80 - 85\%$ of all simulated white dwarfs with $14 \leq r \leq 18.5$ mag (the magnitude limits of the survey) in each model, thus providing robust evidence for the high efficiency of LSS-GAC in targeting white dwarfs. Once the observational uncertainties have been taken into account in our simulations, the distribution of stellar parameters are very similar for all models. We find that all our simulations reproduce well the observed luminosity function, however no particular model seems to fit better the data.

None of our considered models is able to reproduce the observed excess of massive DA white dwarfs. We have investigated possible explanations for this feature and concluded that a plausible scenario is that a sizable fraction of those massive white dwarfs are products of mergers of two initially lower-mass white dwarfs. If that is the case, then the white dwarf merger rate in our Galaxy is considerably higher than currently assumed. This may have important implications for the production

of Type Ia supernovae via the double-degenerate channel.

Finally, it is important as well to emphasize that although our study represents an important step forward towards unveiling the underlying population of DA white dwarfs in the Galaxy, the size of the LSS-GAC sample is still small, and that the stellar parameters we derived for some objects are subject to relatively large uncertainties. Forthcoming LSS-GAC data releases are expected to increase the number of DA white dwarfs by one order of magnitude. In addition, the quality of the LAMOST spectra will improve, which will reduce the uncertainties in the stellar parameter determinations. We will hence derive updated luminosity and mass functions and DA white dwarf formation rates at the end of the survey.

Chapter 5

Revisiting the halo white dwarf luminosity function

5.1 Introduction

White dwarfs are the evolutionary remnant of stars of intermediate and low masses at the zero-age main sequence. The upper limit for a main-sequence star to evolve to a white dwarf is still the matter of some debate, but it is estimated to be $\sim 10\,M_{\odot}$ (Becker & Iben, 1979, 1980; Miyaji et al., 1980; Renzini & Voli, 1981; Nomoto, 1984; García-Berro et al., 1997; Poelarends et al., 2008). Thus, given the shape of the initial mass function it is expected that the vast majority of the remnants of the evolution of single stars will be white dwarfs. Since white dwarfs are numerous, have well-studied properties (Althaus et al., 2010a), and long evolutionary timescales, they are the most suitable tool to study the properties of old populations, like the Galactic stellar spheroid. Moreover, our knowledge of the physics controlling the evolution of white dwarfs relies on solid grounds, since the basic principle of their evolution is a well understood and relatively simple cooling process. Although this basic principle of the theory of white dwarf cooling has remained unaltered in recent decades, we now have very sophisticated and accurate stellar evolutionary models that allow us to perform precise cosmochronology, and to characterize the ensemble properties of several white dwarf populations, like those of the Galactic disk – see Cojocaru et al. (2014), and references therein, for a recent work on this subject – and of the system of Galactic open (García-Berro et al., 2010; Bellini et al., 2010; Bedin et al., 2010) and globular clusters (Hansen et al., 2002, 2013; García-Berro et al., 2014).

We now also have accurate white dwarf cooling tracks for white dwarfs descending from very low-metallicity progenitors (Miller Bertolami et al., 2013; Althaus et al., 2015). These cooling tracks improve upon those used in the early and pioneering calculations of Isern et al. (1998) and García-Berro et al. (2004), and in the more

recent calculation of van Oirschot et al. (2014). These evolutionary sequences have been self-consistently evolved from the zero-age main sequence, through the red giant and thermally pulsing AGB phases to the white dwarf regime, and have revealed the important role of residual hydrogen burning in the atmospheres of low-mass white dwarfs, a physical process that needs verification.

Here we aim to produce synthetic samples of the population of halo white dwarfs using the most up-to-date physical inputs and prescriptions for the Galactic spheroid and compare them with the current observational data. The present chapter is organized as follows. In Section 5.2 we briefly describe the numerical tools employed in this work. It is followed by Section 5.3, where we first discuss the effects of residual hydrogen burning, the adopted initial mass function, the assumed density profile for the Galactic halo, of a population of unresolved binary white dwarfs, and the star formation history. Finally, in Section 5.4, we summarize our calculations and draw our conclusions.

5.2 A brief description of the numerical set up

In the following, we describe the most important inputs of our standard model. We follow the general prescription for the Galactic stellar halo presented in Section 2.3.2. We compute the main-sequence lifetime for each progenitor star, adopting a set of evolutionary sequences with metallicity $Z = 0.0001$, which together with the age of the population (for which in our reference model we adopted 13.7 Gyr), and the progenitor mass, allowed us to determine which stars have had time to become white dwarfs. We then obtained the corresponding masses and cooling ages for each simulated white dwarf. We employ full evolutionary sequences, that is, the progenitor and white dwarf cooling evolutionary tracks, of Althaus et al. (2015). These were obtained from self-consistent evolutionary calculations and expand the previous calculations of Miller Bertolami et al. (2013). Hence, the main-sequence lifetimes, the relationship linking the progenitor and white dwarf masses, and the cooling ages are all self-consistently computed using an homogeneous evolutionary framework. This represents a clear improvement over the most recent calculations of this kind, as we employed self-consistent evolutionary models of the right metallicity, which incorporate state-of-the-art prescriptions for all the relevant physical processes. Our calculations incorporate a fraction of 20% of non-DA white dwarfs, for which we employ theoretical cooling sequences for white dwarfs with pure helium atmospheres. We elaborate on the cooling tracks employed here in Section 5.2.1. Using these values we derived the stellar parameters of each white dwarf in the synthetic sample. Namely, we computed its luminosity, effective temperature, surface gravity, and magnitudes in the different passbands. A standard model of Galactic absorption was also used (Hakkila et al., 1997) to obtain reliable apparent magnitudes.

Our synthetic white dwarf sample is then passed through a series of filters that

Table 5.1: Number of synthetic white dwarfs that survive the different observational cuts for a typical Monte Carlo realization of our standard model.

Filter	$N_{\rm WD}$	%
Initial sample	592 199	100
$\mu_{\rm min}$ cut	8,952	1.5
$12 < r_{59\rm F} < 19.75$	111	0.02
RPMD cut	111	0.02
$V_{\rm tan} > 200\,{\rm km\,s^{-1}}$	77	0.01

mimic the selection criteria employed to observationally select halo white dwarfs in a real sample. These filters are described in detail in Section 5.2.2. After this procedure is followed the white dwarf luminosity function can be computed, except for a normalization factor. We chose to normalize the theoretical results to the density of white dwarfs in the highest density bin with finite error bars of the observational luminosity function, $M_{\rm bol} = 15.75$. This is, in fact, equivalent to normalizing the luminosity function to the total population density, given that this bin practically dominates the stellar counts. In our fiducial model only single white dwarfs were considered, however, we also explored models with a fraction of unresolved binaries in our calculations. In addition, our simulations also include a careful exploration of the effects of other inputs, which is further explained in Section 5.3.

5.2.1 Cooling tracks

White dwarf progenitors in the Galactic halo are characterized by a significantly low metallicity. In the solar vicinity, the halo metallicity distribution function peaks at [Fe/H]$\sim -1.5\,$dex. Actually, Frebel & Norris (2013) and Carollo et al. (2010) found that the Galactic halo has a dual population. The first of these halo populations peaks at [Fe/H]$\sim -1.6\,$dex, whereas the second one peaks at [Fe/H]$\sim -2.2\,$dex. All in all, it is clear that to adequately capture the essential properties of this metal-poor population, a set of cooling sequences of white dwarfs with hydrogen-rich atmospheres descending from low-metallicity progenitors is needed.

We interpolate the cooling times using the set of evolutionary sequences of Althaus et al. (2015). These cooling sequences were computed considering stable, residual hydrogen shell burning in white dwarf atmospheres during the white dwarf stage, although they also provide a set of cooling tracks in which this physical mechanism is disregarded. This is an important issue, since Miller Bertolami et al. (2013) showed that although in most cases residual hydrogen burning is not a significant source of energy, for white dwarfs with hydrogen atmospheres descending from progenitors with very low metallicity it can become a dominant source of energy, and can

delay significantly white dwarf cooling. This effect is more noticeable for low-mass white dwarfs with luminosities ranging from $\log(L/L_{\odot}) = -2$ to -4. As mentioned, we consider that adopting this set of sequences represents a clear improvement with respect to the most recent calculation of the luminosity of halo white dwarfs (van Oirschot et al., 2014), which employed evolutionary sequences for progenitors of solar metallicity.

Although the evolutionary sequences for white dwarfs with hydrogen-rich atmospheres that we adopt here are a clear improvement over previous attempts to model the population of single white dwarfs in the Galactic halo, a cautionary remark is in order here. There is solid evidence that old stellar systems exhibit an enhancement of α elements (Aller & Greenstein, 1960; Wallerstein, 1962). While this kind of enhancement has virtually no effects on the evolutionary timescales of initially low-mass stars, they can play a role in the evolution of intermediate-mass stars. In particular, the resulting total metallicity is larger than that obtained by assuming a solar-scaled composition and, because of the increase of the oxygen abundance, the global abundance of carbon, nitrogen, and oxygen is larger than the corresponding solar-scaled abundance. This, in turn, has an effect on the evolutionary timescales of the progenitor stars of typical white dwarfs. A more rigorous treatment of low-metallicity stars should require the inclusion of α-enhanced initial chemical compositions to compute the stellar sequences. Our evolutionary sequences do not take this enhancement into account, but we estimate that the effects of including it in the calculation of the white dwarf luminosity function is limited. In particular, we checked that the differences of progenitor lifetimes and resulting white dwarf masses between the solar-scaled sequences and α-enhanced ones are smaller than 1% (Pietrinferni et al., 2006) for the metallicities and progenitor masses relevant to our study. Hence, our results are almost insensitive to the adopted metal ratios.

Finally, we employed the cooling sequences of Althaus et al. (2005a) and Althaus et al. (2007) for more massive oxygen-neon white dwarfs, whereas we used the cooling tracks of Bergeron et al. (2011) for white dwarfs with pure helium atmospheres. In both cases, the white dwarf evolutionary sequences correspond to progenitors of solar metallicity. This, of course, is not a self-consistent treatment, but nevertheless we judge that the effects on the computed white dwarf luminosity functions should be modest – see below for a detailed discussion.

5.2.2 The observational sample and selection cuts

We compare our results with the most recent and statistically relevant observational halo white dwarf luminosity function (Rowell & Hambly, 2011). This observational luminosity function was derived from a sample of 93 halo white dwarfs detected in the SuperCosmos Sky Survey (SSS). The SSS is an advanced photographic plate-digitizing machine, using plates taken with the UK Schmidt telescope (UKST), the ESO Schmidt telescope, and the Palomar Schmidt telescope. The resulting cata-

logs were compiled by digitizing several generations of photographic Schmidt plates. The survey uses a photometric system that has three passbands: $b_{\rm J}$, $r_{\rm 59F}$, and $i_{\rm N}$ (Hambly et al., 2001). Employing data from several generations of plates, Rowell & Hambly (2011) constructed a catalog of $\sim$10,000 white dwarfs with magnitudes down to $r_{\rm 59F} \sim 19.75$, and proper motions as low as $\mu \sim 0.05\,{\rm yr}^{-1}$, covering nearly three quarters of the sky. Using strict velocity cuts, the authors isolated subsamples of white dwarfs belonging to the thin disk, thick disk, and halo populations, and presented observational white dwarf luminosity functions for each one of these populations.

In our study, we distinguish between the complete sample of synthetic halo white dwarfs and a restricted sample. The latter is obtained by replicating the observational selection criteria adopted to derive the observed halo white dwarf luminosity function of the SSS. First, a proper motion cut, depending on the $b_{\rm J}$ magnitude, is applied. This proper motion cut is given by the following expression: $\mu > 5(\sigma_{\mu}^{\rm max}(b_{\rm J}) + 0.002)$, where σ_{μ} is the standard deviation in the proper motion measurements. Also, a magnitude cut is imposed, $12 < r_{\rm 59F} < 19.75$. Next, a cut in the reduced proper motion diagram is performed, selecting only objects below and blueward of a reduced proper motion corresponding to $V_{\rm tan} = 30\,{\rm km\,s}^{-1}$. Lastly, to separate the halo population, a tangential velocity cut is used. Specifically, we only select stars with tangential velocities $V_{\rm tan} > 200\,{\rm km\,s}^{-1}$. Finally, we also impose an upper limit on the tangential velocity of $400\,{\rm km\,s}^{-1}$ to prevent selecting stars with velocities larger than the escape velocity of the Galaxy.

5.3 Results

In this section, we compare the results of our simulations to the halo luminosity function of Rowell & Hambly (2011), and we study the sensitivity of the theoretical white dwarf luminosity function to different model inputs.

To start with, we discuss how the observational selection criteria affect the size of the synthetic samples. This is done with the help of Table 5.1. In this table, we list for our reference model the number of white dwarfs in the original synthetic sample (first row), and in subsequent rows we list the number of white dwarfs that survive the different cuts. As is shown in Table 5.1, only 1.5% of the synthetic stars survive the proper motion cut. After applying the magnitude cut, we are left with 111 synthetic stars, representing about 0.02% of the original sample. For this particular realization, the reduced proper motion cut does not further decrease the number of simulated white dwarfs, whereas the filter in tangential velocities even further reduces the number of simulated stars to about 0.01% of the original sample, to 77 white dwarfs, a number comparable with that found observationally.

To compare our results with those of van Oirschot et al. (2014), we only culled white dwarfs using the tangential velocity cut, as they did. Using only this selection

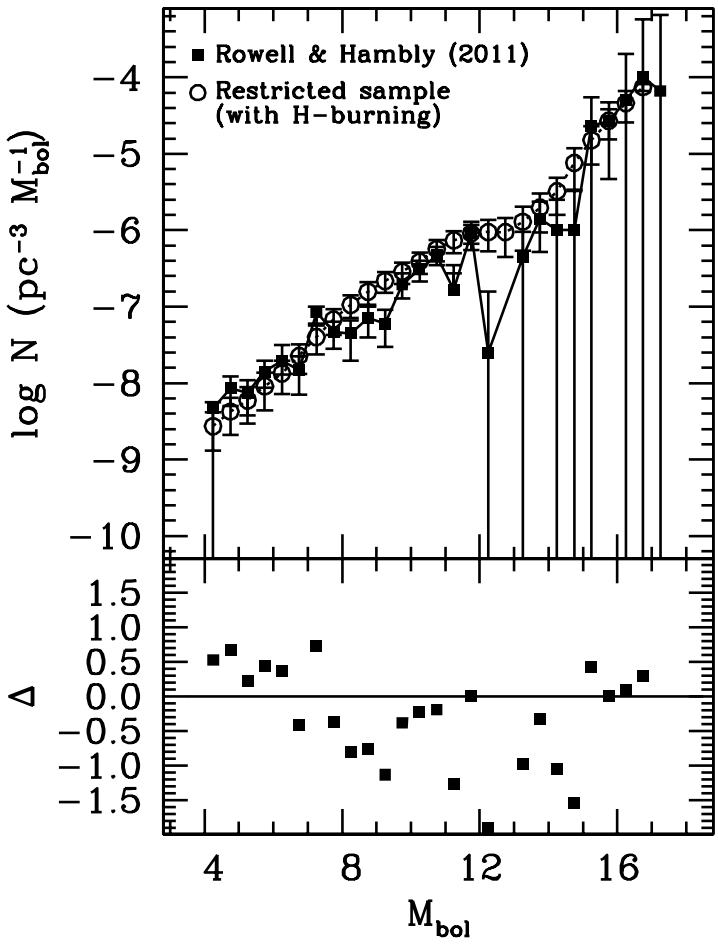

Figure 5.1: Halo white dwarf luminosity function for our fiducial Galactic model. The top panel shows the theoretical white dwarf luminosity function obtained when the cooling sequences incorporating residual hydrogen burning are employed (open circles). We also show, with solid squares, the observed halo luminosity function of Rowell & Hambly (2011). The bottom panel shows the residuals between the observed luminosity function and the theoretical calculations, $\Delta = 2(N_{\rm obs} - N_{\rm sim})/(N_{\rm obs} + N_{\rm sim})$.

criterion, the size of the restricted sample is much larger. In particular, when this procedure is adopted it results in a restricted sample which is 63% of the initial sample. Obviously, the advantage of this large synthetic sample is that it is comparable to the complete sample, producing a smooth luminosity function that faithfully preserves the intricacies of the adopted model. However, the main drawback of only adopting this selection criterion is that the resulting sample is ultimately not directly comparable to the observational sample. Our sample, in contrast, is comparable to the observational sample.

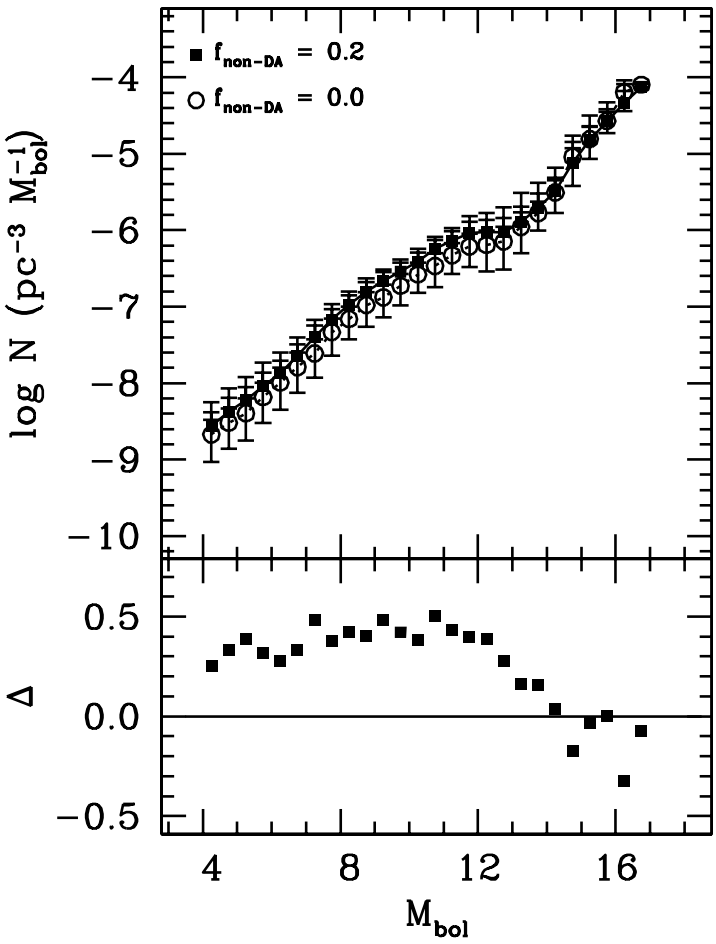

Figure 5.2: White dwarf luminosity functions when only hydrogen-rich synthetic white dwarfs are generated in the Monte Carlo simulation. The bottom panel shows, with solid squares, the residuals between our standard model, in which a fraction of 20% of non-DA white dwarfs was employed, and, with hollow circles, that in which this percentage is zero, $\Delta = 2(N_{\rm std} - N_{\rm no-DA})/(N_{\rm std} + N_{\rm no-DA})$, respectively.

The top panel of Fig. 5.1 shows the white dwarf luminosity function of our reference model with open circles, and the observed luminosity function of Rowell & Hambly (2011) with solid squares, while we show the corresponding residuals in the bottom panel. As is shown in the figure, the agreement between the theoretical results and the observed data is very good. Our fiducial model reproduces not only the observed slope of the white dwarf luminosity function, but also accounts for the scarcity of halo white dwarfs at very low luminosities ($M_{\rm bol} > 17$). This indicates that our Monte Carlo code correctly reproduces the selection criteria employed by Rowell & Hambly (2011).

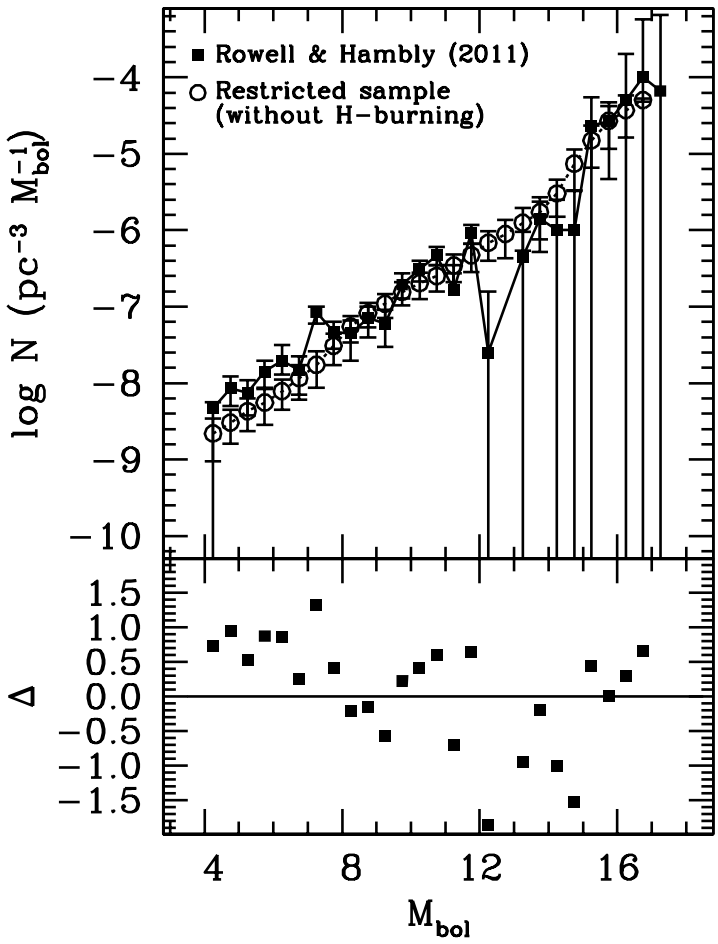

Figure 5.3: Same as Fig. 5.1 for the case in which residual hydrogen burning is not considered. The bottom panel shows the residuals between the luminosity function computed using our standard cooling sequences and that obtained when residual hydrogen burning is artificially ignored, $\Delta = 2(N_{\rm std} - N_{\rm no-H})/(N_{\rm std} + N_{\rm no-H})$.

In a second step, we checked the sensitivity of our synthetic white dwarf luminosity function with our choice of cooling sequences for massive, oxygen-neon white dwarfs, and non-DA white dwarfs. For these stars we employed a set of cooling sequences of solar metallicity. Specifically, we assessed the final number of these white dwarfs in the restricted sample, that is, once we take observational selection criteria into account, and we found that in a typical Monte Carlo realization only one of these white dwarfs, at most, survives the successive selection cuts. The most stringent observational cut is the magnitude cut, $r_{59\rm F} \sim 19.75$. In most Monte Carlo realizations none of these white dwarfs survives this cut. Additionally, we mention

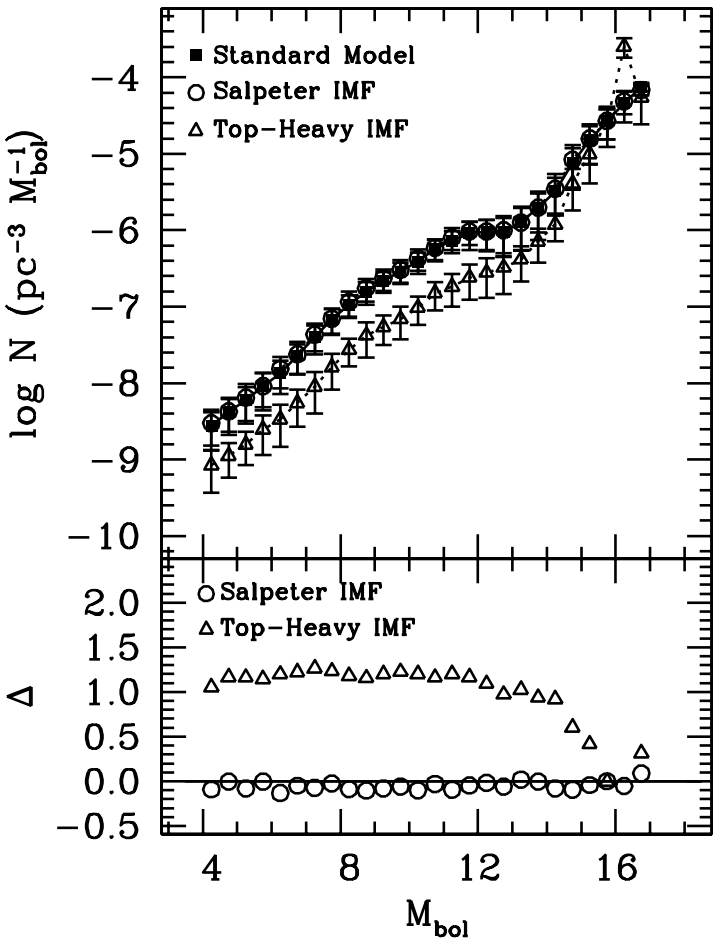

Figure 5.4: White dwarf luminosity functions when different initial mass functions are considered for the stellar spheroid. The bottom panel shows, with circles, the residuals between our standard model and, with triangles, those obtained when the Salpeter (1955) and the top-heavy initial mass function of Suda et al. (2013) are used, $\Delta = 2(N_{\rm std} - N_{\rm IMF})/(N_{\rm std} + N_{\rm IMF})$, respectively.

that even if this cut is not employed, the proper motion cut eliminates almost 99.5% of oxygen-neon white dwarfs from the final sample. Thus, there are very few oxygen-neon white dwarfs in the final sample. The reason for this behavior is twofold. First, these white dwarfs are very scarce, since their formation is strongly inhibited by the shape of the initial mass function. Thus, not surprisingly, they contribute little to the white dwarf luminosity function. The second reason is that since these white dwarfs are made of oxygen and neon, their heat capacity is smaller than that of a carbon-oxygen white dwarf of the same mass (Garcia-Berro et al., 1997) and consequently cool faster. Accordingly, these white dwarfs essentially contribute to the

faintest bins of the luminosity function, which is not probed by observations, because it is excluded by the magnitude cut. In summary, we conclude that the influence of adopting a set of cooling sequences of solar metallicity for oxygen-neon white dwarfs is negligible.

To assess the influence of adopting a set of cooling sequences of solar metallicity for non-DA white dwarfs, we ran an additional simulation in which the percentage of non-DA white dwarfs was set to zero, and consequently all the synthetic stars had hydrogen-rich atmospheres. We then computed the residuals between the resulting white dwarf luminosity function and that obtained with our reference model, for which the ratio of non-DA white dwarfs is 20%. The results, shown in Fig. 5.2, reveal that the differences are small, although not negligible. As a matter of fact, the space density of hot white dwarfs is smaller in the case in which only synthetic DA white dwarfs are generated, however, this is a consequence of the normalization procedure. Hydrogen-deficient white dwarfs have cooling sequences that resemble those of a black body, whereas the atmospheres of DA white dwarfs are more transparent. Consequently, at low temperatures non-DA white dwarfs cool faster than DA white dwarfs. Thus, the percentage of non-DA white dwarfs increases for decreasing luminosities, and therefore these white dwarfs accumulate at luminosities close to that of the peak of the theoretical luminosity function and even smaller. However, the number counts of white dwarfs in the luminosity bins close to the peak of the luminosity function dominate the total number counts of white dwarfs in the synthetic sample. Thus, since the total number of white dwarfs in any Monte Carlo realization must be kept constant and, moreover, must be close to the observed value, the hot branch of the luminosity function is depleted in the case in which non-DA white dwarfs are not generated. Nevertheless, we emphasize that because white dwarf cooling sequences of low metallicity for non-DA white dwarfs are not available, it is clear that this procedure largely overestimates the impact of adopting a set of cooling sequences of inappropriate metallicity. Thus, we conclude that the possible effect of adopting a set of cooling sequences of solar metallicity for non-DA white dwarfs is limited.

Next, we assess the sensitivity of these results to the most relevant inputs of our model. In particular, we first discuss if the adopted cooling tracks for carbon-oxygen white dwarfs with hydrogen-rich atmospheres could change this picture. In a second step, we study whether a different choice of the adopted initial mass function could affect our results. Later, we evaluate if a different halo model could have a noticeable influence in our calculations. Finally, we also study whether different percentages of unresolved binaries vary the shape of the white dwarf luminosity function. We conclude our assessment by comparing our theoretical results for different ages of the stellar halo.

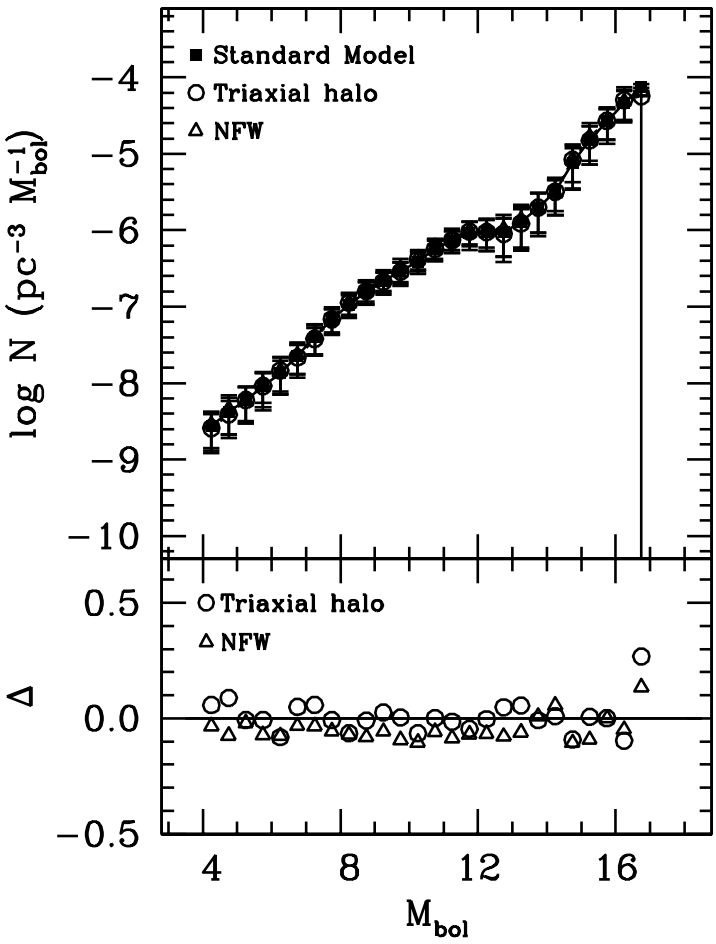

Figure 5.5: White dwarf luminosity functions for different density profiles of the stellar halo. The bottom panel shows, with circles, the residuals between our standard model, and, with triangles, those obtained when the density profile of a triaxial halo (Helmi, 2004) and that of Navarro et al. (1996) are employed, $\Delta = 2(N_{\rm std} - N_\rho)/(N_{\rm std} + N_\rho)$, respectively.

5.3.1 Hydrogen burning

It has been shown (Miller Bertolami et al., 2013) that residual hydrogen burning can significant impact the cooling process of white dwarfs with progenitors of very low metallicity, the effect being more noticeable for low-mass white dwarfs (those with masses between 0.5 and 0.6 $M_\odot$). Since low-mass white dwarfs contribute to all the luminosity bins of the hot branch of the luminosity function, and since the shape of the luminosity function is directly related to the cooling rate, it is natural to ask ourselves whether a different choice of cooling sequences could affect the slope at moderately high luminosities. We check this using the two different sets of cooling

tracks described in Althaus et al. (2015). The first of these sets is that used in our reference model, and considers residual nuclear burning, while the second set does not take nuclear reactions into account (as it occurs for white dwarf progenitors with $Z > 0.001$).

In Fig. 5.3, we present the resulting white dwarf luminosity function for the halo population when we adopt the cooling sequences in which residual hydrogen burning is artificially ignored. This luminosity function should be compared with that shown in Fig. 5.1. The only difference between both sets of theoretical calculations is that for the case in which the cooling sequences incorporating residual hydrogen burning are employed, there is a small plateau between $M_{\rm bol} = 12$ and 14, which is absent in the case in which no residual hydrogen burning is considered. This plateau reflects the slow-down of cooling due to the release of energy of residual hydrogen burning. The differences between both calculations are minor, however, and the currently available observational luminosity function, which is derived using only ~ 100 white dwarfs, does not allow us to draw definite conclusions about the real existence of residual nuclear burning.

5.3.2 Initial mass function

As mentioned, we also test the influence that the adopted initial mass function may have on our results. Since the formation timescale of the stellar halo is short, it is straightforward to show that when a burst of negligible duration is adopted the luminosity function is given by,

$$N(L) \propto \frac{dn}{dM_{\rm bol}} = \frac{dn}{dM}\frac{dM}{dM_{\rm bol}} \propto \Phi(M)\frac{dM}{dM_{\rm bol}}. \tag{5.1}$$

In this expression, n stands for the space density, and Φ for the initial mass function (IMF). Thus, it is clear that the adopted initial mass function should influence the shape of the luminosity function.

To test the influence of the IMF on the luminosity function, we employ three parametrizations. The first is that used in our fiducial model, namely the so-called universal mass function of Kroupa (2001). For the mass range relevant to our study this IMF is totally equivalent to a two-branch power law with exponent $-\alpha$, with $\alpha = 1.3$ for $0.08 \leq M/M_{\odot} < 0.5$ and $\alpha = 2.3$ for $M/M_{\odot} \geq 0.5$. We also compute theoretical white dwarf luminosity functions adopting the classical IMF of Salpeter (1955), which is a power law with index $\alpha = 2.35$. Finally we also adopt a top-heavy IMF, i.e.,

$$\Phi(M) = \frac{1}{M}\exp\left(\frac{-\log(M/\mu)}{2\sigma^2}\right). \tag{5.2}$$

In this expression $\mu = 10\,M_{\odot}$ and $\sigma = 0.44$. This IMF was introduced by Suda et al. (2013), and is dominated by high -mass stars. It has been found that this IMF

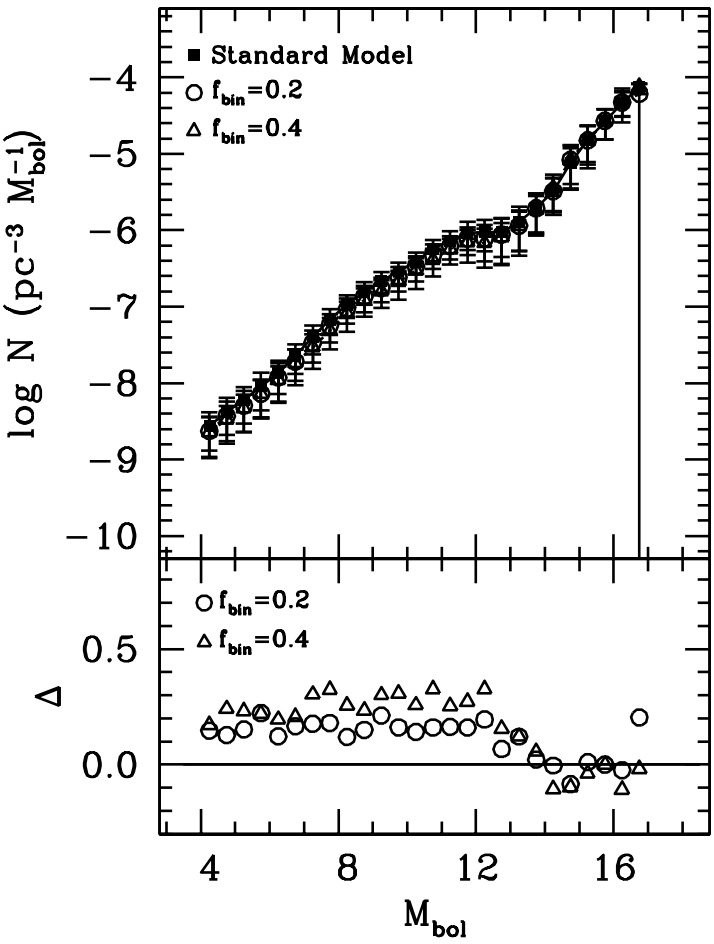

Figure 5.6: Same as Fig. 5.5, except for different fractions of unresolved binaries. The bottom panel shows, with circles, the residuals between our standard model with circles, and, with triangles, those obtained when the adopted fractions of unresolved binaries are 20% and 40%, $\Delta = 2(N_{\rm std} - N_{\rm bin})/(N_{\rm std} + N_{\rm bin})$, respectively.

better reproduces the characteristics of metal-poor populations, namely those with [Fe/H]≤ -2.

The corresponding luminosity functions for these IMFs are shown in the top panel of Fig. 5.4, and their respective residuals with respect to our fiducial model are shown in the bottom panel of this figure. As shown in the figure, there are no noticeable differences between the calculations in which the IMF of Kroupa (2001) and that of Salpeter (1955) are employed. The reason for this is that in the relevant luminosity range the slope of both IMFs is very similar. We note, however, that when the top-heavy IMF of Suda et al. (2013) is used, the luminosity function presents a

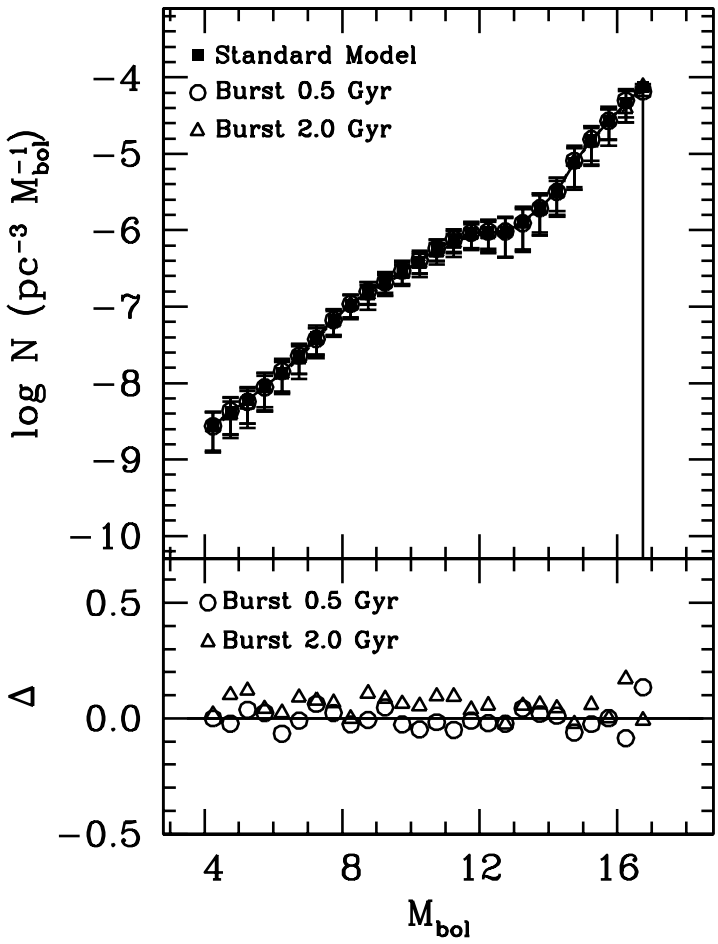

Figure 5.7: Same as Fig. 5.5, except for different duration of the initial burst of star formation. The bottom panel shows, with circles, the residuals between our standard model and, with triangles, those obtained when the adopted duration of the initial burst of star formation are 0.5 and 2.0 Gyr, $\Delta = 2(N_{\rm std} - N_{\Delta t})/(N_{\rm std} + N_{\Delta t})$, respectively.

drop in the space density at large luminosities. This deficit of bright white dwarfs is quite apparent, but it is marginally consistent with the observed data.

5.3.3 Density profiles

Another possible concern would be the adopted density profile for the stellar halo. As explained in Section 5.2, in our reference model we adopted the density profile of the classical isothermal sphere, but there are other density profiles that are worth studying. Accordingly, here we study how this choice affects our results. To do this we first adopted a triaxial oblate halo model, which is based in a logarithmic

dark halo potential (Helmi, 2004),

$$V = \frac{1}{2}{v_0}^2 \ln(R^2 + z^2/q^2 + d^2), \tag{5.3}$$

which results in a density distribution:

$$\rho(R,z) = \left(\frac{v_0^2}{4\pi G q^2}\right) \frac{(2q^2+1)d^2 + R^2 + (2-q^{-2})z^2}{(d^2 + R^2 + z^2 q^{-2})^2}. \tag{5.4}$$

In this expression, we have adopted $d = 12\,\mathrm{kpc}$ and $v_0 = 131.5\,\mathrm{km/s}$, which gives a circular velocity of the Sun of 229 km/s, and an oblateness parameter $q = 0.8$. Our third and last profile is the following widely used profile of (Navarro et al., 1996):

$$\rho \sim \left(\frac{r}{r_s}\right)^{-1} \left(1 - \frac{r}{r_s}\right)^2, \tag{5.5}$$

with $r_s = 18\,\mathrm{kpc}$.

As Fig. 5.5 reveals, the differences between the luminosity functions computed, using these three different density profiles for the stellar halo, are totally negligible. This is because the sample of halo white dwarfs of Rowell & Hambly (2011) is local, whereas the differences between the three model profiles should be prominent at large distances.

5.3.4 Unresolved binaries

One of the potential problems when calculating the observed luminosity function for single stars are unresolved binary white dwarfs, since they compute as single stars, and hence this may modify the shape of the luminosity function. This has been proven to be the case in some Galactic clusters (Bedin et al., 2008; García-Berro et al., 2010). It is therefore interesting to check the effect that a certain fraction of unresolved binaries can have on the theoretical luminosity function. To test this, we compute a new set of simulations based on our fiducial model, increasing the fraction of unresolved binaries. As mentioned earlier, we consider no unresolved binaries in our reference model. As for the distribution of secondary masses, we adopted a model in which the masses of both components are not correlated.

Fig. 5.6 shows the result of this numerical experiment when the fractions of unresolved binaries are, 20% and 40%, respectively. As can be observed in this figure, increasing the fraction of unresolved binaries considered in the sample does not result in any noticeable change, but results in a slight reduction of the number of white dwarfs populating the brightest luminosity bins. The reason for this can easily be explained. Since low-luminosity white dwarfs have longer evolutionary timescales the low-luminosity bins also have large space densities. Consequently, unresolved binaries also concentrate in the luminosity bins with the largest densities, and thus

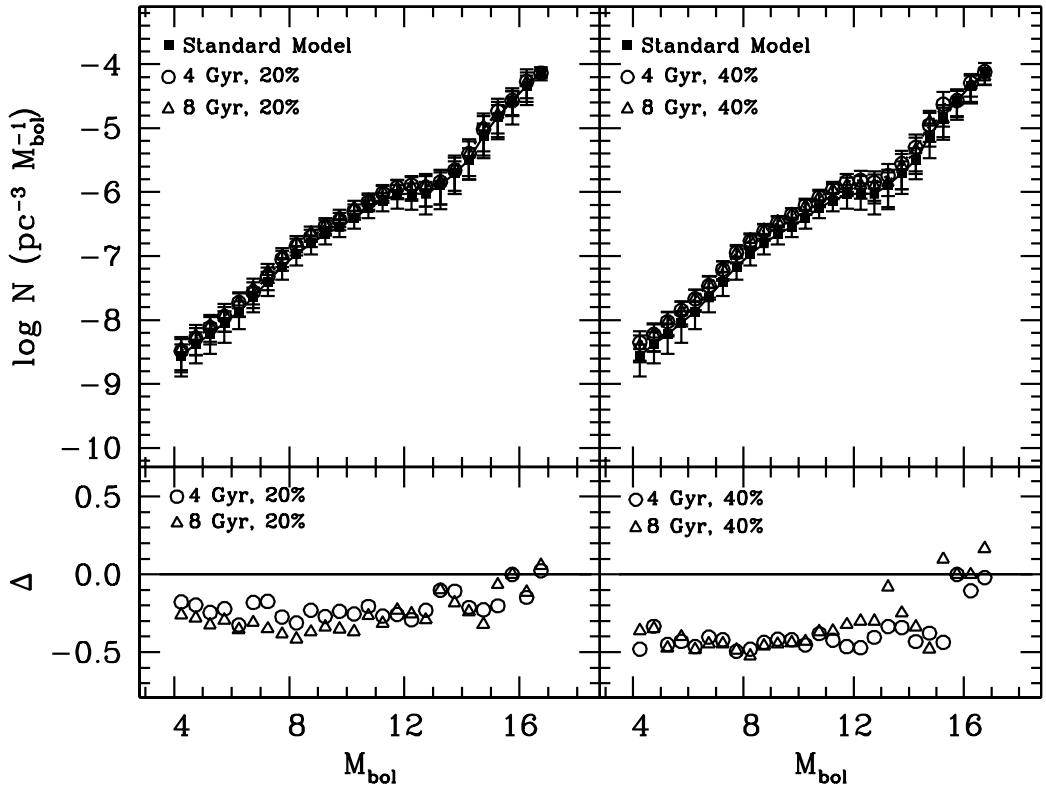

Figure 5.8: Same as Fig. 5.5, except for four merger episodes of two strengths and at two different times. The bottom panels show the residuals between our standard model and those obtained when the impact of a merger episode is analyzed, $\Delta = 2(N_{\rm std} - N_{\rm mer})/(N_{\rm std} + N_{\rm mer})$. See text for details.

the bright luminosity bins are less populated. Since we normalize our theoretical luminosity function to the observed luminosity bin at $M_{\rm bol} = 15.75$, the result is that the bright branch of the theoretical luminosity function is depleted. Nevertheless, the differences are minor even when an unrealistic percentage of 40% of the objects in the synthetic sample are unresolved binaries.

5.3.5 The star formation history

Another point of concern is the adopted star formation history. This may also have potential effects on the morphology of the hot branch of the halo white dwarf luminosity function. To start with we discuss the effects of the duration of the initial burst of star formation. This is done with the help of Fig. 5.7, where we show the theoretical white dwarf luminosity functions for two burst of duration 0.5 and 2.0 Gyr, and compare them with our reference model, for which we recall that we

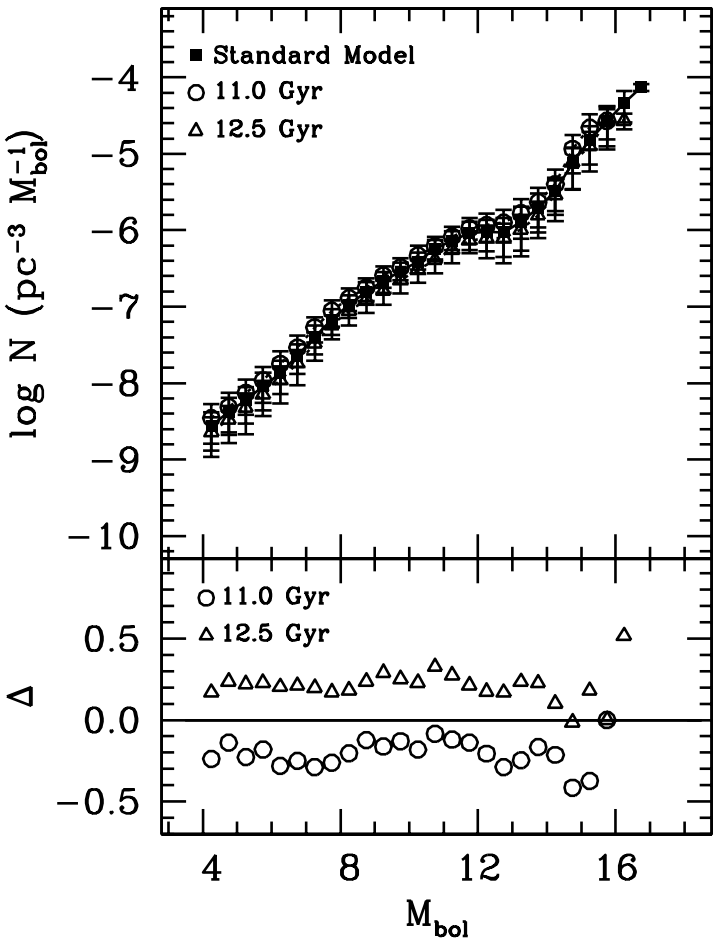

Figure 5.9: Same as Fig. 5.5, except with different ages of the halo population. The bottom panel shows the residuals between our standard model and the luminosity functions obtained when the age of the stellar halo is varied, $\Delta = 2(N_{\rm std} - N_T)/(N_{\rm std} + N_T)$.

employed a burst of duration 1.0 Gyr. This figure clearly shows that, except for the smaller space densities at moderately high luminosities, the differences between these two luminosity functions and our fiducial functions are marginal. Consequently, current observations do not allow us to discern between different duration of the initial burst of star formation.

Furthermore, a consensus about the origin of the stellar spheroid has not been reached yet. The two main competing scenarios, i.e., monolithic collapse of the protogalactic gas (Eggen et al., 1962) or formation through several merger episodes (Searle & Zinn, 1978), still need to be confronted with observations. Hence, it is natural to wonder if these two scenarios leave observable imprints in the shape of

the hot branch of the white dwarf luminosity function of single halo white dwarfs. To this end, we conducted an additional set of simulations in which, in addition to the initial burst of star formation, we modeled the luminosity function in which a second burst of star formation occurring some time ago is adopted. Specifically, we ran four additional simulations in which a secondary burst of star formation occurs at times 4 and 8 Gyr, varying the strength of this secondary burst. The metallicities of the secondary bursts of star formation were the same as adopted for the initial burst. This choice minimizes the effects of these merger episodes, but the effects of the different metallicity of the secondary bursts are expected to be minor. Specifically, the secondary burst was given amplitudes 20% and 40% of the initial burst. In all cases, the duration of all the bursts (that is, both the initial and the secondary ones) were kept fixed and equal to 0.1 Gyr, while we recall that in the standard model a duration of 1 Gyr was adopted. The results of this numerical experiment are shown in Fig. 5.8. In the left panels of this figure, we show the results when we adopt a secondary burst with an amplitude 20% of the initial burst, whereas the right panels show the results from when the amplitude of the secondary burst is increased to 40% of the primary burst. As shown in the figure, the differences are again very small. Thus, unfortunately, the current observational database of halo white dwarfs does not allow us to distinguish the two aforementioned formation scenarios of the stellar halo.

5.3.6 Age of the population

Finally, we ran a set of simulations in which we varied the age of the halo population, from 11 to 13 Gyr, and we compared the results of these calculations with those obtained in our reference model, for which we adopted an age of 13.7 Gyr. We show the results of these calculations in Fig. 5.9. As expected, the bright branch of the white dwarf luminosity function does not depend appreciably on the adopted age of the stellar spheroid. Moreover, since the observed luminosity function does not show a cutoff, the age of the halo population cannot be yet computed using the termination of the cooling sequence of halo white dwarfs. This is a consequence of the cuts used to select the observed sample, and is specifically caused by the cut in bolometric magnitude. The only quantitative assessment about the age of the halo that can be made with the available observed data is to place a lower limit. This can be done in a simple way by imposing that the dimmest populated luminosity bin of the theoretical white dwarf luminosity function is that observationally found, at $M_{\rm bol} = 17.25$. Using this procedure we find that, although it is not possible to fit the halo age, a lower limit for its age of 12.5 Gyr can be safely established.

5.4 Conclusions

We have revisited the luminosity function of halo white dwarfs in the light of the recently computed white dwarf cooling sequences for low-metallicity progenitors. These cooling sequences (Miller Bertolami et al., 2013; Althaus et al., 2015) have been derived evolving their progenitors self-consistently from the zero-age main sequence, through the red giant and thermally pulsing AGB phases to the white dwarf regime, and have unveiled the role of residual hydrogen burning in the atmospheres of low-mass white dwarfs. In this sense, it is important to realize that these evolutionary calculations supersede those used in the early and pioneering calculations of the halo white dwarf luminosity function of Isern et al. (1998) and García-Berro et al. (2004), and in the recent work of van Oirschot et al. (2014). Moreover, in pursuing this endeavor we have employed a state-of-the-art numerical code, incorporating the most recent advances that enable an accurate description of the Galactic halo and a detailed implementation of the observational biases and restrictions. This is an issue that most theoretical calculations do not take into account, thus impeding a sought comparison with the observed sample. This is an important issue, as the observed sample of white dwarfs belonging to the Galactic spheroid suffers from small statistics. Moreover, given that the density of halo white dwarfs is low and that this population is old, hence, intrinsically faint, the detection of halo white dwarfs is hampered by observational difficulties. Consequently, the selection biases are important, and we are restricted to comparing the theoretical results of our results with an observational sample plagued with uncertainties.

Since residual hydrogen burning occurs at moderately low luminosities, say from $\log(L/L_{\odot}) = -2$ to -4, the halo luminosity function could eventually offer a unique possibility to test the reliability of these recent cooling sequences. This could have important consequences for our understanding of how white dwarfs are formed and how their progenitor stars evolve in low-metallicity environments, and, more specifically, it could shed light on the occurrence of the third dredge-up for metallicities $\lesssim 10^{-3}$. We have found that, unfortunately, the scarcity of halo white dwarfs at the luminosities at which residual hydrogen burning occurs prevents us from making a meaningful comparison between the sequences that incorporate this physical ingredient and those that do not. Thus, this effort will have to wait until we have larger and more reliable samples. Alternatively, this can be done using the white dwarf luminosity functions of Galactic globular clusters, of which NGC 6397 Torres et al. (2015) is, perhaps, the leading example.

Additionally, we have investigated whether or not the observed luminosity function of single white dwarfs can be eventually used to learn more about the stellar population of the Galactic halo. In particular, we have studied whether the observed luminosity function can be used to constrain the initial mass function of this population, its star formation history and age, to probe different halo density profiles, or possibly to discern the fraction of unresolved binaries that may contaminate obser-

vations. Unfortunately, our calculations show that the hot branch of the luminosity function is almost insensitive to all these input, as occurs in the disk white dwarf luminosity function (Isern et al., 2008). Consequently, unless we have a more accurate determination of the luminosity function at large bolometric magnitudes (low luminosities) there is no hope to extract all this information from the observed data. However, large space-borne surveys, like Gaia, will provide us with a large sample of halo white dwarfs (Torres et al., 2005), and hopefully a wealth of information will be extracted in the near future. Nonetheless, the lack of sensitivity of the hot branch of the luminosity function of halo white dwarfs to all these inputs can be interpreted positively since it allows us to obtain a robust statistical measure of the cooling rate of white dwarfs at low metallicities and high luminosities.

Chapter 6

Monte Carlo simulations of the WD+MS population in the SDSS

6.1 Introduction

White dwarf-main sequence (WD+MS) binaries are the evolutionary products of main sequence binaries. In a $\sim 75\%$ of the cases the initial main sequence binary separations are large enough for the binary components to evolve in the same way as if they were single stars. The orbital separations of the remaining $\sim 25\%$ of main sequence binaries are close enough for the systems to undergo a phase of dynamically unstable mass transfer once the primary becomes a red giant or an asymptotic giant branch star (Willems & Kolb, 2004). This leads to the formation of a common envelope around the giant's nucleus and the main sequence companion (Webbink, 2008) and hence to a dramatic decrease of the orbital separation. WD+MS binaries that evolved through a common envelope phase are referred to as post-common envelope binaries (PCEBs).

Modern large scale surveys such as the Sloan Digital Sky Survey (York, Adelman, Anderson, Anderson, Annis et al., 2000), hereafter SDSS, the UKIRT Infrared Sky Survey (Dye, Warren, Hambly, Cross, Hodgkin et al., 2006), UKIDSS, and the Large sky Area Multi-Object fiber Spectroscopic Telescope (LAMOST) survey (Zhao et al., 2012), have facilitated the compilation of comprehensive spectroscopic WD+MS binary samples during the last few years (Rebassa-Mansergas et al., 2010, 2012a; Liu et al., 2012; Rebassa-Mansergas et al., 2013a; Ren et al., 2014). Among these, the SDSS WD+MS binary catalog is the largest and most homogeneous, with a total number 3,291 systems identified within the data release 12 (Rebassa-Mansergas et al., 2016b).

SDSS WD+MS binaries have been used as superb tools for analyzing numerous

open problems in astrophysics. These include, for example, constraining theories of close compact binary evolution (Zorotovic et al., 2010; Davis et al., 2010; Zorotovic et al., 2011; Rebassa-Mansergas et al., 2012b), providing observational confirmation for disrupted magnetic braking (Schreiber et al., 2010; Zorotovic et al., 2016), rendering robust evidence for the majority of low-mass white dwarfs being formed in binaries (Rebassa-Mansergas et al., 2011), studying the pairing properties of main sequence stars (Ferrario, 2012), constraining the rotation-age-activity relation of low-mass main sequence stars (Rebassa-Mansergas et al., 2013b), investigating the statistical properties of the PCEB population (Toonen & Nelemans, 2013; Camacho et al., 2014; Zorotovic et al., 2014), or constraining the age-metallicity relation of the Galactic disc (Rebassa-Mansergas et al., 2016a). In this chapter we continue using SDSS WD+MS binaries as astrophysical tools, in particular we aim at constraining the properties of the initial mass ratio distribution (IMRD) of main sequence binaries. Hereafter, we define the mass ratio as $q = m_2/m_1$, where m_1 is the mass of the primary (or more massive) star in a main sequence binary, and m_2 is the mass of its main sequence companion or secondary star.

The IMRD plays a key role for understanding the evolution of stars in binary systems and for constraining models of binary star formation. The physical properties of the IMRD have been a topic of much debate for over four decades with results often contradicting each other. Indeed, decreasing (Jaschek & Ferrer, 1972), increasing (Dabbowski & Beardsley, 1977), bimodal (Trimble, 1974) and flat IMRDs have been suggested. This lack of agreement remains when comparing more recent results. For example, whilst Ducati et al. (2011) claim a decreasing IMRD, Reggiani & Meyer (2013) suggest a flat IMRD. These discrepancies may be a simple consequence of the IMRD being dependent on both the primary mass and the orbital separation, as suggested by Duchêne & Kraus (2013). This seems to be confirmed by several observational studies (Carrier et al., 2002; Burgasser et al., 2006; Delfosse et al., 2004; Carquillat & Prieur, 2007; Raghavan et al., 2010; Tokovinin, 2011; Sana et al., 2012; Reggiani & Meyer, 2013; Gullikson et al., 2016). However, it is important to emphasize that these observational studies are affected by important selection effects, which likely introduce uncertainties in the results obtained. This is particularly important when the secondary star in a main sequence binary is intrinsically faint and harder to detect against a moderately hot primary.

In order to shed light on this issue we perform a serie of Monte Carlo simulations of the WD+MS binary population in the Galactic disc, which are calibrated using the largest sample of SDSS WD+MS binaries currently known (Rebassa-Mansergas et al., 2016b), under the premise that the spectral type distribution of the secondary stars in these WD+MS binaries is sensitive to the choice of IMRD used in our simulations. The simulations are performed implementing the IMRD as a universal law governing all the main sequence binaries that are formed so that we can investigate how different assumptions for this parameter reflect on the resulting WD+MS populations. Observational selection effects are carefully taken into account in our

simulations.

This chapter is organized as follows. In Section 6.2 we describe the observational sample of WD+MS from (Rebassa-Mansergas et al., 2016b). Afterwards, in Section 6.3 we briefly describe the numerical setup and in Section 6.4 we review the selection effects and describe their numerical implementation. In Section 6.5, we analyze the effects of the adopted age, the assumed star formation history model and the initial-to-final mass relation, also placing constraint on the common envelope parametrization and the initial mass ratio distribution. Finally, in Section 6.6, we summarize our calculations and discuss our conclusions.

6.2 The observational WD+MS binary sample

As already mentioned, the SDSS WD+MS binary catalog currently constitutes the largest and most homogeneous sample of spectroscopic WD+MS binaries, with 3,291 systems identified within the data release 12 (Rebassa-Mansergas et al., 2016b). Because of selection effects, the vast majority of SDSS WD+MS binaries contain a low-mass M-dwarf secondary star, as hotter main sequence stars generally outshine the white dwarf in the optical SDSS spectrum (more details on this issue are provided in Section 6.4.3).

The majority of SDSS WD+MS binaries have been observed as part of the Legacy Survey (Adelman-McCarthy et al., 2008; Abazajian et al., 2009) and BOSS – Barion Oscillation Spectroscopic Survey (Dawson et al., 2013) – simply because of their overlap in color space with quasars. Hence, Legacy and BOSS WD+MS binaries generally contain hot ($\gtrsim 10000\,\mathrm{K}$) white dwarfs. In order to overcome this observational bias, WD+MS binaries were additionally observed as part of a SEGUE – Sloan Exploration of Galactic Understanding and Evolution (Yanny et al., 2009) – surveys. These surveys aimed at targeting WD+MS binaries containing cool white dwarfs (Rebassa-Mansergas et al., 2012a). Hereafter, we flag these systems as SEGUE WD+MS binaries. Finally, a small number of WD+MS binaries were observed by the SEGUE and SEGUE-2 surveys of SDSS that aimed at obtaining spectra of main sequence stars and red giants. We flag these as SEGUE-2 WD+MS binaries.

White dwarf effective temperatures, surface gravities and masses and secondary star (M dwarf) spectral types were derived for each of the SDSS WD+MS binaries from their SDSS spectra using the decomposition/fitting routine outlined in Rebassa-Mansergas et al. (2007). (Rebassa-Mansergas et al., 2016b) demonstrated that the stellar parameter distributions resulting from the four different sub-populations of SDSS WD+MS binaries (namely Legacy, BOSS, SEGUE and SEGUE-2 WD+MS binaries) are statistically different, a simple consequence of the different selection criteria and magnitude limit cuts applied by the four sub-surveys. In consequence, the overall SDSS WD+MS binary population is substantially affected by selection effects and modeling the entire SDSS WD+MS sample, thus implies the added com-

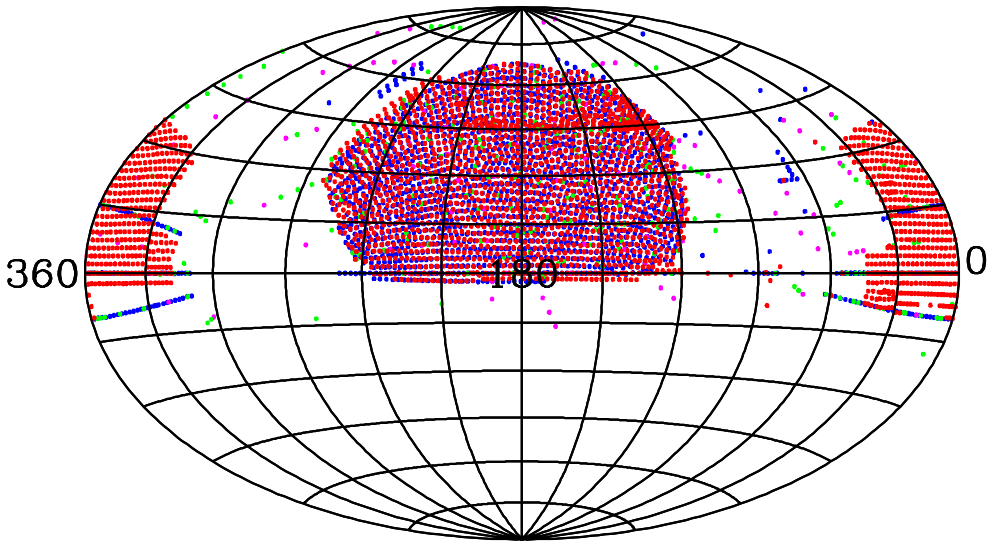

Figure 6.1: Plate positions in equatorial coordinates. Red dots correspond to the Legacy plates, blue dots to BOSS, green dots to SEGUE and magenta dots to SEGUE-2.

plication of implementing the specific selection biases for each sub-sample. Moreover, our simulations need to take into account that SDSS observed in specific regions of the sky, being these marked by the positions of the over 4,000 fiber-fed spectroscopic plates used during the observations (see Fig. 6.1).

6.3 The synthetic WD+MS binary sample

Here we present the main ingredients of our population synthesis simulations of the WD+MS binary sample. The ZAMS mass of the primary was randomly sampled from the initial mass function of Kroupa (2001) and Kroupa & Weidner (2003) and the time of birth obtained from a constant star formation history unless otherwise stated – see Section 6.5.1. The progenitor metallicity was assumed to be Solar for the entire population and the single or binary star membership was decided according to an assumed binary fraction of a 50%. This is in agreement with the findings of Duchêne & Kraus (2013), who give a multiplicity frequency of 44% for F/G/K type progenitors and $> 50\%$ for A type progenitors. If the star is member of a binary system we obtain the ZAMS mass of the secondary star according to an IMRD. The initial binary separation and eccentricity are sampled following the distributions described in Section 2.2.2. We then assign a position (and distance) for the object according to a Galactic model. The allowed positions follow the coordinate distributions of all SDSS plates used up to the data release 12. For each plate we define a cone centered at its equatorial coordinates of aperture 7 squared degrees

that extends to 2 kpc. We employ a double exponential distribution for the local density of stars, with a 300 pc scale height and a 2.6 kpc scale length for the thin disc, and a 900 pc scale height and a 3.5 kpc scale length for the thick disk (Bland-Hawthorn & Gerhard, 2016). Velocities are sampled according to the prescriptions presented in Section 2.3.1. We only select unresolved WD+MS binaries for our final sample, considering the position of each binary, its final separation and inclination (according to a flat $\sin i$ distribution), assuming an angular resolution of 1.5 arcsec for the SDSS.

We then allow the synthetic star or binary to evolve until present time, in accordance to a thin disk age of 10 Gyr (Cojocaru et al., 2014) and a thick disk age of 12 Gyr. We note that Feltzing & Bensby (2009) presents a sample of very likely thick disk candidates with ages on average above 10 Gyr and that Ak et al. (2013) finds thick disk cataclysmic variables with ages up to 13 Gyr, so our adopted age is a reasonable estimate. If the object is a single star and has time to become a white dwarf, it evolves following the cooling tracks detailed in the following section. If that is the case, the mass of the white dwarf is obtained from the initial-to-final mass relation (IFMR) according to the prescription of Hurley et al. (2002). If the object is a binary and the primary star has time to become a white dwarf, then the system can evolve through two different scenarios, either as a detached system, where the primary star evolves into a white dwarf, or passing through mass transfer episodes. In the last case, the evolution of the binary is reproduced using the BSE package of Hurley et al. (2002), following the parameter assumptions for binary evolution and for the common envelope phase of Camacho et al. (2014), which were detailed in Section 2.2.2. The common-envelope evolution of the binary is governed by two parameters, namely, $\alpha_{\rm CE}$, which describes the efficiency in converting orbital energy into kinetic energy used to eject the envelope, and $\alpha_{\rm int}$, which gives the internal energy contribution to expelling the envelope. The influence of these two parameters is further investigated in Section 6.5.2.

6.3.1 Evolutionary sequences and cooling tracks

The BSE package (Hurley et al., 2002) provides luminosities, temperatures and surface gravities for both the main sequence and the white dwarf, computed using the evolutionary tracks of Pols et al. (1998) and a modified Mestel cooling law, respectively. We re-compute these stellar parameters using more modern tracks that also provide photometric magnitudes in the Johnson-Cousins $UBVRI$ system (taking into account both rejuvenation and ageing during overflow episodes). These evolutionary tracks are also used to derive the stellar parameters of the binary components in binaries where no mass transfer interactions take place.

For the main sequence companion we use the new evolutionary tracks for low mass stars from Baraffe et al. (2015), which provide improved predictions for optical colors. The only downside here is that these sequences only provide the VRI magnitudes.

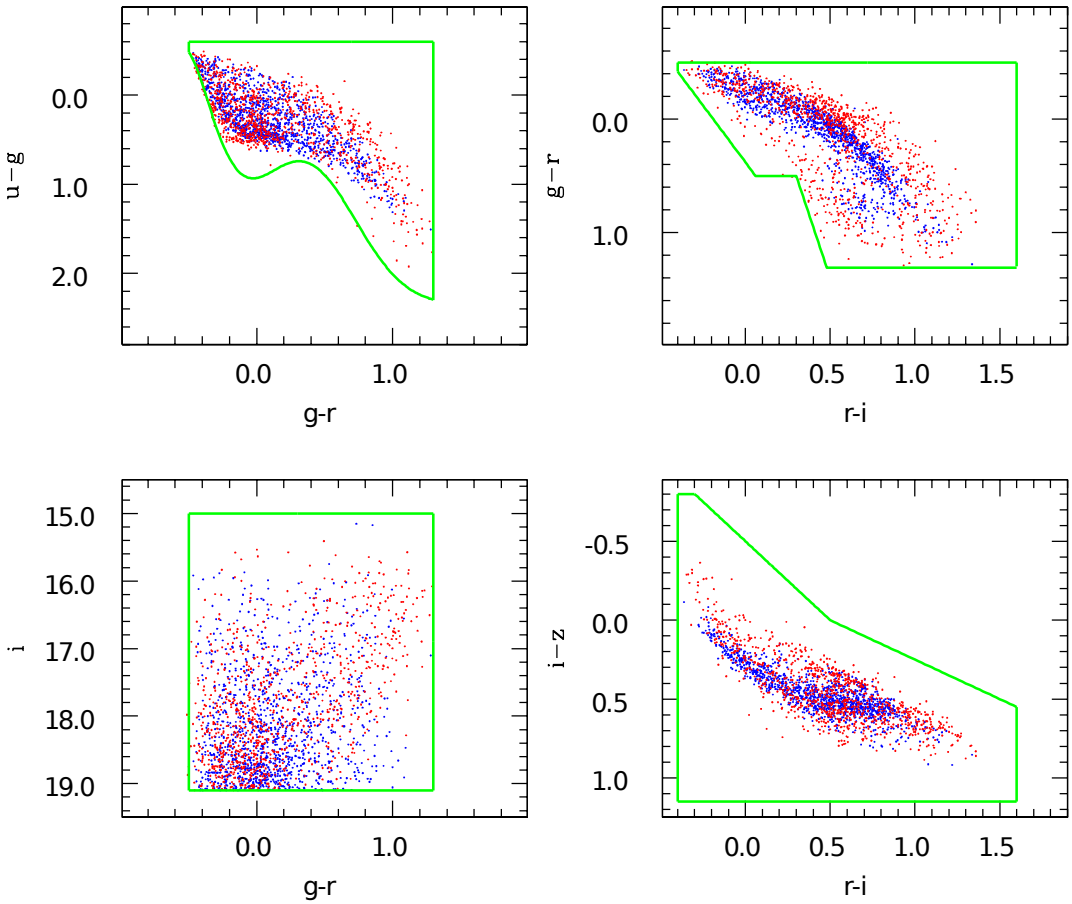

Figure 6.2: Color-color and color-magnitude diagrams of the synthetic and observed Legacy WD+MS subsample. The red dots are the observed data, while the blue dots correspond to the synthetic objects. The color and magnitude cuts presented in Section 6.4 are shown as green lines.

Thus, we obtain U and B magnitudes using a third order polynomial approximation based on observations of G, K and M stars from Pickles (1998).

For carbon-oxygen white dwarfs (those with masses $M_{\rm WD}$ between 0.45 and 1.1 $M_{\odot}$) we use the evolutionary calculations of Renedo et al. (2010), for oxygen-neon core white dwarfs ($M_{\rm WD} > 1.1\,M_{\odot}$) we employ those of Althaus et al. (2005a); Althaus et al. (2007) and for helium core white dwarfs ($M_{\rm WD} < 0.45\,M_{\odot}$) we adopt the cooling tracks of Serenelli et al. (2001). In all cases Solar metallicity and hydrogen-rich atmospheres are assumed and the full set of $UBVRI$ magnitudes are provided. We then convert these to the *ugriz* system and account for Galactic extinction, as explained in Section 2.4.

6.4 Observational biases

In this section we provide details on the selection effects that affect the observed SDSS WD+MS binary population and we explain how these selection effects are incorporated into our synthetic WD+MS binary populations (see Fig. 6.3 for a representative example).

6.4.1 Color and magnitude cuts

The spectroscopic survey of SDSS is magnitude-limited. Hence, all our synthetic WD+MS binaries must comply with the magnitude limit cut of SDSS, which depends on the specific survery as follows:

$$15 < i < 19.1, \text{ for Legacy} \tag{6.1}$$
$$15 < g < 22, \text{ for BOSS} \tag{6.2}$$
$$15 < g < 20, \text{ for SEGUE and SEGUE-2} \tag{6.3}$$

Moreover, observed SDSS WD+MS binaries define a clear region in the *ugriz* color space (Rebassa-Mansergas et al., 2013a) which allows us to define color cuts to cull our synthetic samples (see Figure 6.2 for an example):

$$\begin{aligned}(u-g) < & 0.93 - 0.27 \times (g-r) - 4.7 \times (g-r)^2 + \\ & 12.38 \times (g-r)^3 + 3.08 \times (g-r)^4 - 22.19 \times \\ & (g-r)^5 + 16.67 \times (g-r)^6 - 3.89 \times (g-r)^7,\end{aligned} \tag{6.4}$$

$$\begin{aligned} & -0.6 < (u-g), \\ (g-r) < & 2 \times (r-i) + 0.38, \text{ if } -0.4 < (r-i) \leq 0.06, \\ (g-r) < & 4.5 \times (r-i) - 0.85, \text{ if } 0.3 < (r-i) \leq 0.48, \\ (g-r) < & 0.5, \text{ if } 0.06 < (r-i) \leq 0.3, \\ & -0.5 < (g-r) < 1.3, \\ & -0.4 < (r-i) < 1.6, \\ (r-i) < & 0.5 + 2 \times (i-z), \text{ if } (i-z) > 0, \\ (r-i) < & 0.5 + (i-z), \text{ if } (i-z) \leq 0, \\ & -0.8 < (i-z) < 1.15 \end{aligned} \tag{6.5}$$

It is important to emphasize here that the SEGUE WD+MS binary survey was defined for targeting WD+MS binaries containing cool white dwarfs. Hence, SEGUE

WD+MS binaries populate different regions in the *ugriz* color space (Rebassa-Mansergas et al., 2012a). These regions define the following color cuts that we applied to the synthetic SEGUE WD+MS binary population:

$$\begin{aligned}
(u-g) &< 2.25, \\
-0.2 < (g-r) &< 1.2, \\
-19.78(r-i)+11.13 < (g-r) &< 0.95(r-i)+0.5, \\
(i-z) &> 0.5 \quad \text{for } (r-i) > 1.0, \\
(i-z) &> 0.68(r-i)-0.18 \quad \text{for } (r-i) \leq 1.0, \\
0.5 < (r-i) &< 2.0, \\
15 < g &< 20
\end{aligned} \tag{6.6}$$

6.4.2 Spectroscopic completeness

The target selection criteria employed by the different sub-surveys of the SDSS implies that not all WD+MS binaries have the same probability of being observed. The Legacy and BOSS surveys follow selection criteria that aim at targeting mainly galaxies (Strauss et al., 2002) and quasars (Richards et al., 2002; Ross et al., 2012). Hence, WD+MS binaries containing hot white dwarfs ($> 10,000-15,000\,\mathrm{K}$) and/or late type (>M2) companions are more likely to be observed. SEGUE WD+MS binaries are dominated by systems containing cooler white dwarfs and/or early type companions, a simple consequence of our defined target selection criteria (Rebassa-Mansergas et al., 2012a). Finally, SEGUE-2 WD+MS binaries have similar colors to those of single main sequence stars, i.e. the white dwarf contributes little to the spectral energy distribution. Hence, in order to produce realistic simulations of the SDSS WD+MS population we need to implement the probability for a given WD+MS binary to be observed. That is, we need to apply a spectroscopic completeness correction.

The first step in this process is determining the spectroscopic completeness of the observed sample, following the approach described in Camacho et al. (2014). That is, we consider a four dimensional space composed by the $u-g$, $g-r$, $r-i$ and $i-z$ colors, and we define a 0.2 magnitude four-dimension sphere around each observed object. We then use the `casjobs` interface to count the number of point sources with clean photometry ($N_{\rm phot}$) as well as the number of spectroscopic sources ($N_{\rm spec}$) within each sphere. The ratio $N_{\rm spec}/N_{\rm phot}$ gives the spectroscopic completeness for the observed object. Then, for each WD+MS binary produced in the synthetic sample, we compute a four-dimensional distance in color space to each of the observed WD+MS binaries and we select the observed object that is closest to the synthetic one. If the distance to the selected closest observed object is less than 0.2 magnitudes, then the synthetic WD+MS binary will be assigned the same

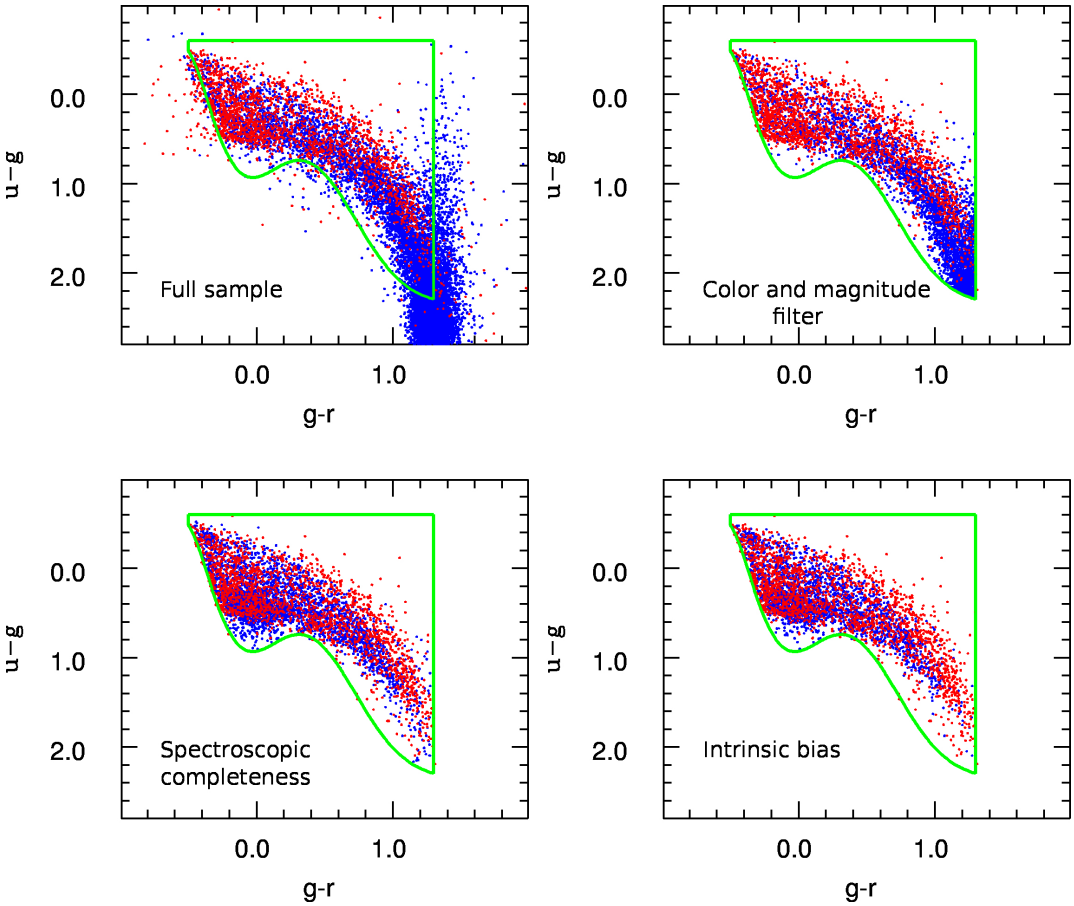

Figure 6.3: Color-color diagram of the synthetic WD+MS sample obtained using our population synthesis code. The red dots are the observed data, and the blue dots the synthetic data for our reference model, after applying the different filters as explained in Section 6.4.

spectroscopic completeness as that of the observed one. Conversely, if the distance is larger than 0.2 magnitudes, then the assigned completeness will be null. This exercise is performed separately for the observed/simulated objects within the four sub-surveys of SDSS.

6.4.3 Intrinsic WD+MS binary bias

In order to detect in the sample a spectrum of a WD+MS binary the spectral features of both components must be observed. This implies that WD+MS binaries in which one of the two stars dominates the spectral energy distribution will be harder, or even impossible, to detect (Parsons et al., 2016 submitted). Moreover, WD+MS binaries that are further away are intrinsically fainter and the resulting SDSS spectra

are of lower signal-to-noise ratio (since the SDSS exposures are generally the same for all targets). Identifying the spectral features of the two components is obviously harder when dealing with low signal-to-noise ratio spectra. It is then mandatory to eliminate a certain percentage of the synthetic WD+MS binaries according to these reasonings.

In Camacho et al. (2014) was presented a multi-demensional grid of WD+MS binary parameters (white dwarf effective temperatures and surface gravities, secondary star spectral types and distances) that allowed to evaluate which synthetic WD+MS binaries would have been detected by the SDSS. We follow the same approach in this work.

6.4.4 Uncertainties in the observed WD+MS binary parameters

The measured SDSS photometric magnitudes and the stellar parameters derived from fitting the SDSS WD+MS binary spectra can have relatively large uncertainties (Rebassa-Mansergas et al., 2016b). Hence, it is necessary to incorporate such uncertainties in the synthetic WD+MS binary sample before any comparison to the observational data sets is performed. Fig. 6.4 shows the photometric errors, σ, as a function of the corresponding magnitude. As it can be seen, the photometric errors clearly increase as the apparent magnitude is fainter. We fitted the distributions using a fifth order polynomial, which provides us with an expression for σ as a function of the apparent magnitude. We then defined a Gaussian error distribution for that specific magnitude that we sampled in order to obtain the photometric error of each synthetic WD+MS binary in each passband. We applied a similar procedure for the errors in the white dwarf effective temperature and surface gravity, using a third order polynomial fit in this case (see Fig. 6.5). For the companion spectral type distribution we assumed a constant value of σ of one bin, i.e. an uncertainty of one spectral sub-class. Only after adding the corresponding errors in photometric magnitudes and stellar parameters we do apply the color and magnitude cuts and the other observational filters previously described. Given the random character of this procedure, for each realization that provided us with a WD+MS binary sample from the Monte Carlo code, we repeated the process of adding errors and afterwards filtering the sample 20 times per realization.

Finally, for both the observed and synthetic samples we only considered objects with a relative error smaller than 10% in effective temperature, and with absolute errors under 0.075 dex in surface gravity. This explains why different distributions from the same sample contain a different number of objects.

6.5 Results

We use our population synthesis code to model the WD+MS binary population in the Galactic disk. For this, we first define a standard model that uses a flat IMRD

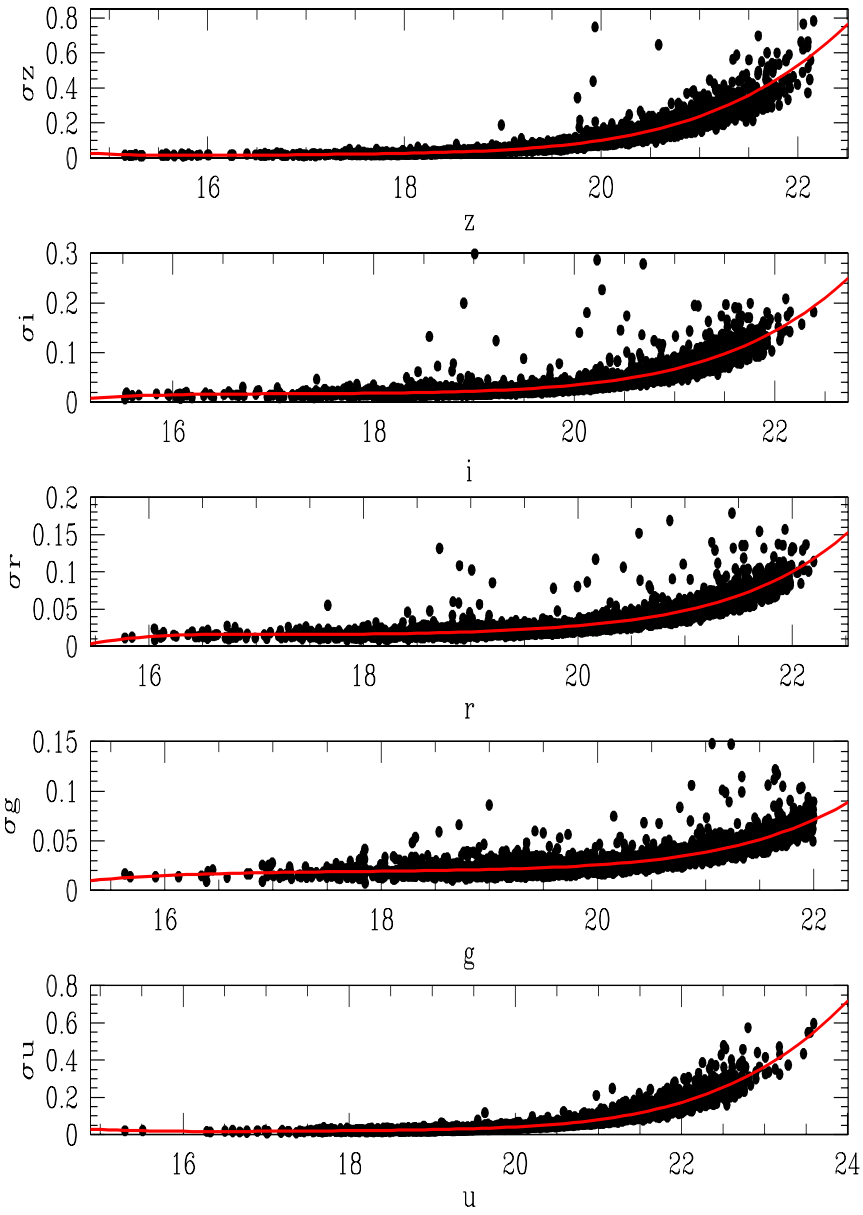

Figure 6.4: Distribution of photometric errors in passbands the u, g, r, i and z passbands (black dots), each fitted to a fifth order polynomial (red line).

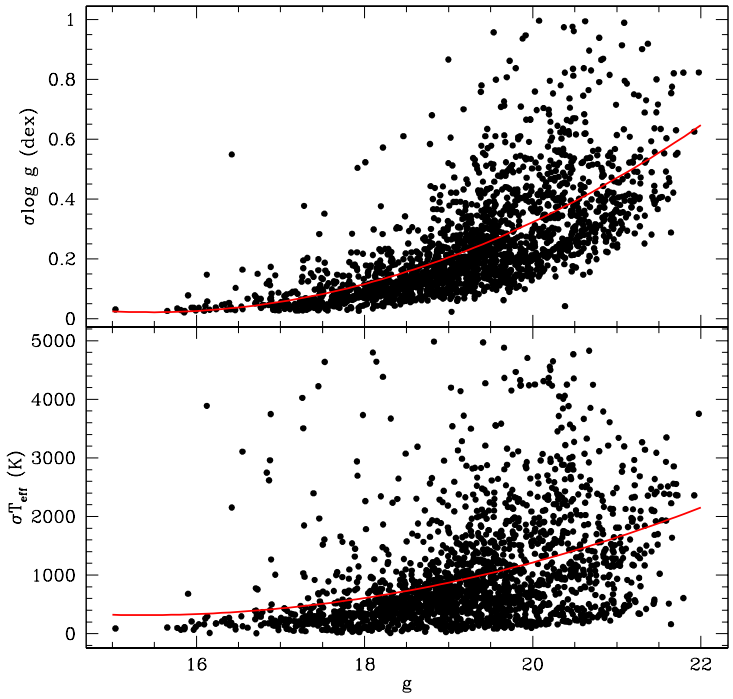

Figure 6.5: Observational errors for white dwarf effective temperatures and surface gravities as a function of the apparent magnitude g (black dots), fitted to a third order polynomial (red line)

$(n(q))$, 10 Gyr thin disk age, constant star formation rate, $\alpha_{\rm CE} = 0.3$, $\alpha_{\rm int} = 0$ and all the fixed parameter assumptions previously explained in Section 6.3.

6.5.1 Preliminary checks

In order to properly cover the parameter space, we initially varied several input parameters to better understand their possible effect on the three distributions under scrutiny: the white dwarf effective temperature and surface gravity, and the M dwarf spectral type. We first varied the age of the thin disk between 8 and 12 Gyr. We obtained that the three distributions were not particularly sensitive to precise value of the age. Overall, for shorter ages ($\sim$ 8 Gyr), the ratio between the secondary and the primary peak in the white dwarf $\log g$ distribution shifts to smaller values when compared to observations, and for longer ages ($\sim$ 12 Gyr) the white dwarf $T_{\rm eff}$ distribution shows an excess of cool white dwarfs with respect to the observed data. We also try three different prescriptions for the star formation history: constant, recent enhanced star formation with one broad peak in the SFR between 1 and 3 Gyr

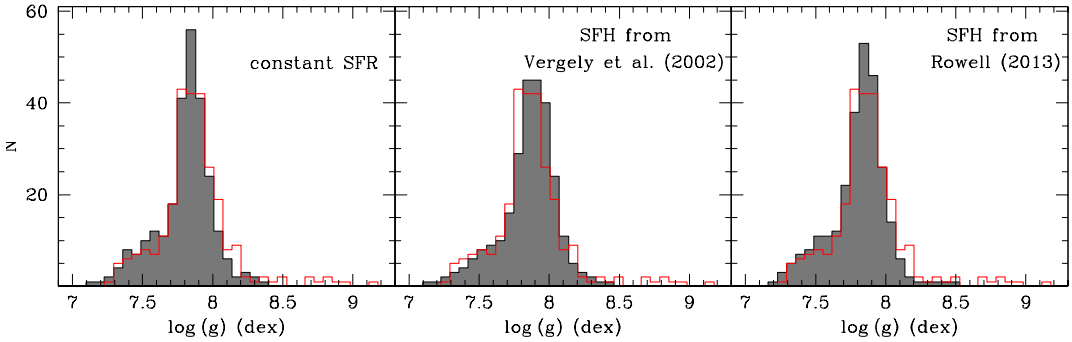

Figure 6.6: Synthetic $\log g$ distribution for different SFR models (gray solid histograms): constant SFR – left panel – SFH form Vergely et al. (2002) – central panel – and that of Rowell (2013) – right panel. The observational $\log g$ distribution is also represented (red open histogram).

ago (Vergely et al., 2002), and a bimodal SFR with two broad peaks at around 2 and 7 Gyr ago (Rowell, 2013)). The different synthetic $\log g$ distributions are shown in Figure 6.6 (solid gray histograms) compared with the observational distribution (open red histogram).

In our reference model (left panel of Fig 6.6), the white dwarf $\log g$ distribution appears to be slightly, but systematically, shifted towards smaller values as compared to observations, while the other two SFH models (central and right panels, respectively) seem to correct this trend, which could in fact favor the existence of a star formation burst occurring 2–3 Gyr ago. For convenience, in our simulations we use the IFMR of Hurley et al. (2002), which results from an evolution algorithm consisting basically of a competition between core-mass growth and envelope mass-loss. Nevertheless, we test this against the IFMR of Catalán et al. (2008). We obtained that there is a systematic difference, although it does not generally surpass a 0.02 difference in white dwarf mass. Lastly, we consider an initial 15% contribution from the thick disk, which corresponds to a $7-17\%$ contribution to the final sample (after all observational filters are passed), depending on the full parameter combination. However, we run one simulation with no thick disk contribution and the differences in the three distributions are minimal.

6.5.2 Formation channels and the CE efficiency parameter

Nebot Gómez-Morán et al. (2011) show that $21-24\%$ of all SDSS WD+MS binaries have experienced common-envelope evolution. We perform this test over the simulated data and find that, for the standard model, $\sim 10\%$ of present day WD+MS binaries from the entire simulated sample and 29% from the filtered sample have gone through a common envelope episode (and have not merged in the meantime), which

Table 6.1: Percentage of present day WD+MS binaries that have undergone common envelope evolution (and have not yet merged), in the complete and filtered sample for different values of $\alpha_{\rm CE}$ and $\alpha_{\rm int}$ assumptions

$\alpha_{\rm CE}$	$\alpha_{\rm int}$	Complete sample	Filtered sample
0.1	0.0	3%	10%
0.2	0.0	6%	21%
0.3	0.0	10%	29%
0.3	0.1	13%	30%
0.3	0.2	14%	32%
0.3	0.5	17%	33%
0.5	0.0	16%	38%
0.7	0.0	21%	43%
1.0	0.0	26%	45%

is compatible with the observed data. This percentage proves to be sensitive to the choice of $\alpha_{\rm CE}$ and $\alpha_{\rm int}$. Low values of $\alpha_{\rm CE}$ result in an underproduction of low-orbital separation binaries, while high values of $\alpha_{\rm CE}$ lead to an overproduction. $\alpha_{\rm int} > 0$ also leads to a slight increase in the percentage of WD+MS that suffer a common-envelope episode. Table 6.1 collects our findings when varying these two parameters (but maintaining the other assumptions of the standard model). This table shows that $\alpha_{\rm CE} \sim 0.2 - 0.3$ gives the best results.

Another way to constrain the value of $\alpha_{\rm CE}$ is using the overall $\log g$ distribution. Once more, for small values of $\alpha_{\rm CE}$ the secondary peak in this distribution cannot be reproduced, whereas large values of this parameter lead to an excess with respect to the observed data for the secondary peak (see Fig. 6.7). Again, the best fit is obtained for $\alpha_{\rm CE} \sim 0.3$.

6.5.3 Initial mass ratio distribution (IMRD)

Recently, Ducati et al. (2011) have studied a large number of models by using Monte Carlo simulations and comparing to a sample consisting of 249 objects from the Ninth Catalogue of Spectroscopic Binaries (Pourbaix et al., 2004). Their findings favor a linearly decreasing $n(q) \sim 1 - aq$, with $a = 0.5$. However, given the diversity of the models they studied, we adopt most of them together with the more classical IMRD studied in Camacho et al. (2014), testing in total 12 models for the IMRD.

The best approach for comparing the simulated distributions to the observed ones is to use distance metrics, a procedure which will allow us not only to decide which simulated distribution fits best, but also to order the models from best to worst. Among the possible number of distance metrics that can be defined, we choose three

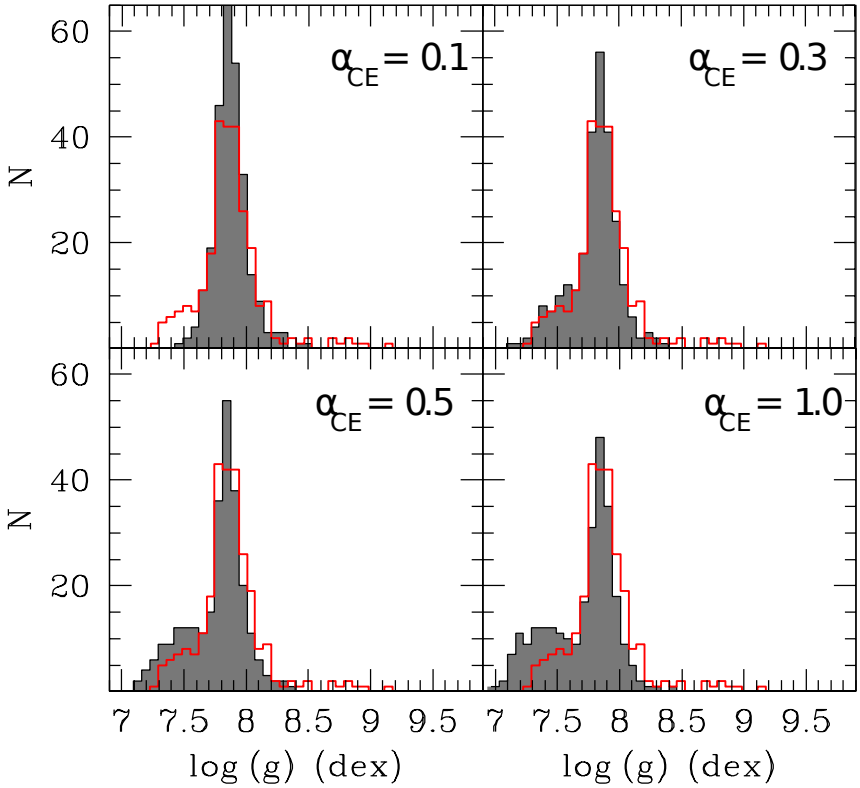

Figure 6.7: Overall $\log g$ distribution for different values of $\alpha_{\rm CE}$ (adopting $\alpha_{\rm int} = 0$)

typical ones, which perfectly cover the statistical properties of our sample. Let P be the observed distribution and Q the simulated one, the three metrics employed here are:

i) Standard least squares:

$$D_{\rm LS} = \sum_i (P(i) - Q(i))^2 \tag{6.7}$$

ii) Kullback-Leibler (KL) divergence:

$$D_{\rm KL} = \sum_i P(i) \ln\left(\frac{P(i)}{Q(i)}\right) \tag{6.8}$$

iii) Bhattacharyya coefficient:

$$\cos(\beta) = \sum_i \sqrt{P(i)Q(i)} \tag{6.9}$$

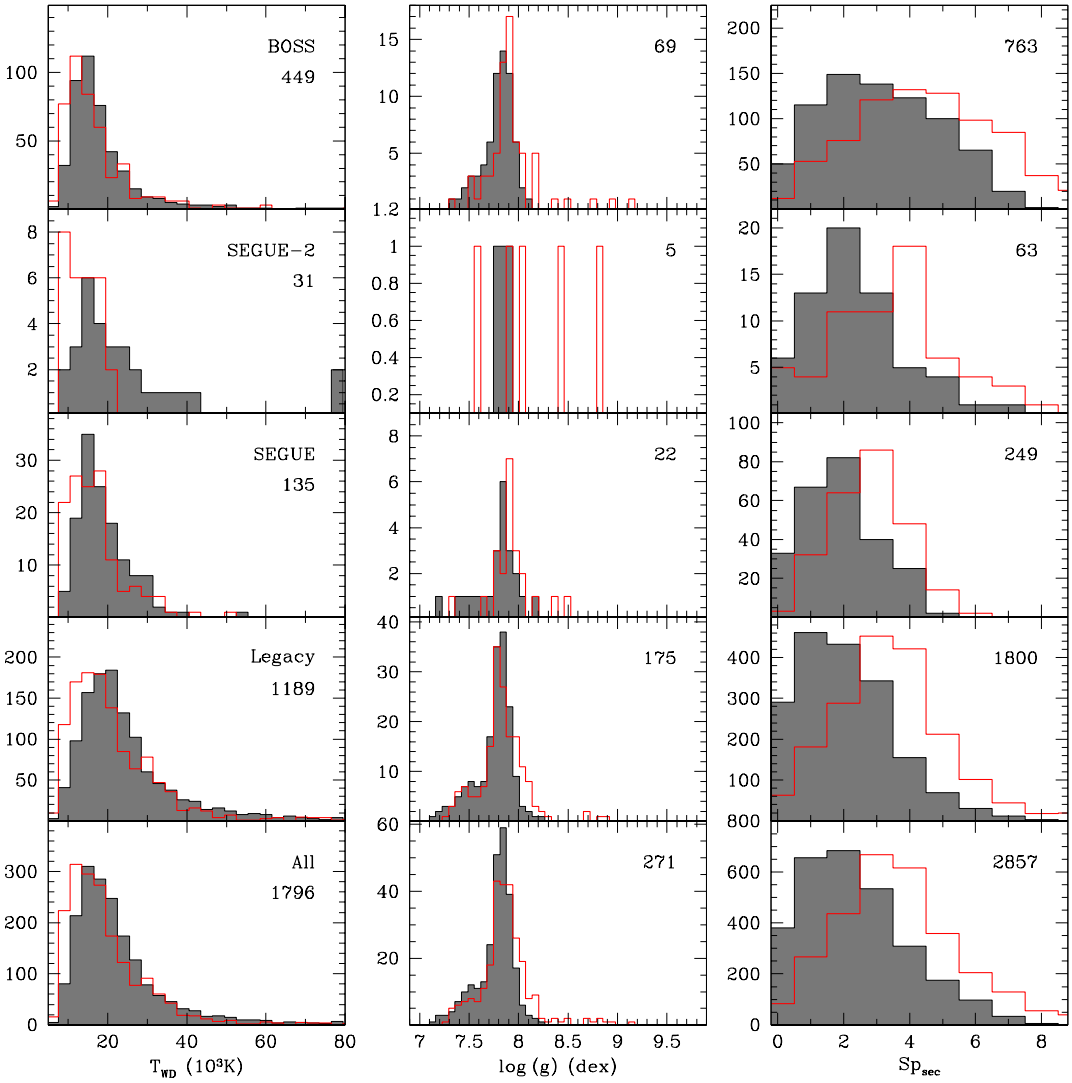

Figure 6.8: Distributions of the hite dwarf effective temperature, surface gravity and M dwarf spectral type. The observational data is that of Rebassa-Mansergas et al. (2016b), and the synthetic data has been obtained assuming $n(q) \sim q$. This is a an example of a bad fit.

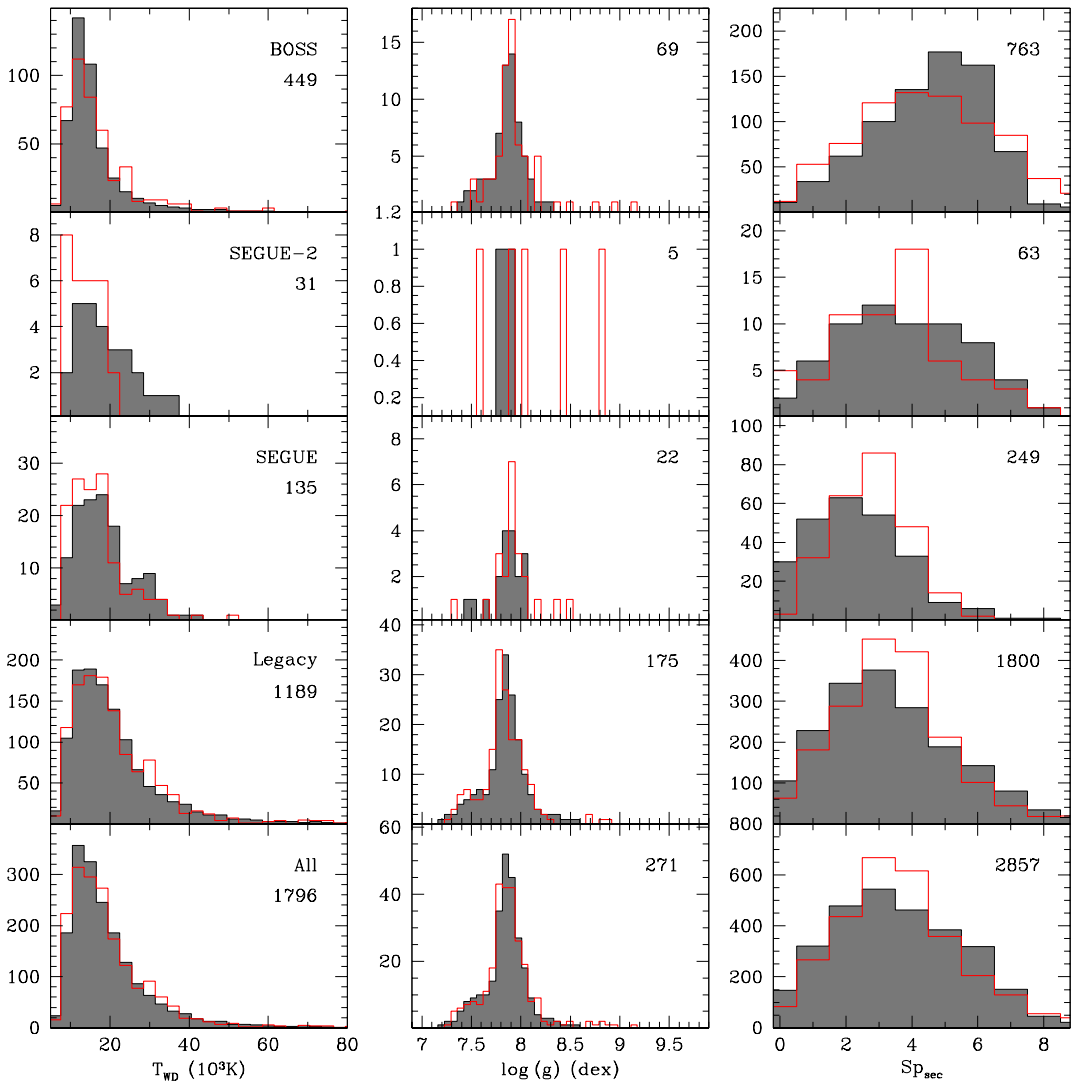

Figure 6.9: White dwarf effective temperature, white dwarf surface gravity and M dwarf spectral type distributions. Observational data from Rebassa-Mansergas et al. 2016b, synthetic data obtained assuming a $n(q) \sim q^{-1}$ – example of a good fit

Table 6.2: Different models for $n(q)$, ordered from best to worst according to the fit to observational data. In the last three columns is represented the average value of the three distance metrics used in our analysis (see text for details).

Order	$n(q)$	Type	$\langle D_{\rm KL} \rangle$	$\langle D_{\rm LS} \rangle$	$\langle \beta \rangle (^\circ)$
1	q^{-1}	Decreasing	7.89×10^{-2}	6.28×10^{-3}	9.1
2	$\left(q - \frac{1+q_0}{2}\right)^2, q_0 = 0.08$	Bimodal	7.97×10^{-2}	6.65×10^{-3}	8.9
3	$1 - aq, a = 0.5$	Decreasing	8.46×10^{-2}	9.07×10^{-3}	10.4
4	q^{-2}	Decreasing	8.90×10^{-2}	9.02×10^{-3}	10.5
5	1	Flat	9.49×10^{-2}	9.96×10^{-3}	10.8
6	$\left(q - \frac{1+q_0}{2}\right)^2, q_0 = 0.1$	Bimodal	1.07×10^{-1}	1.33×10^{-2}	12.1
7	q	Increasing	1.79×10^{-1}	2.25×10^{-2}	14.7
8	$(q - q_0)^{1/3}, q_0 = 0.08$	Increasing	2.09×10^{-1}	2.39×10^{-2}	15.5
9	$q - q_0, q_0 = 0.08$	Increasing	3.42×10^{-1}	4.14×10^{-2}	18.7
10	$q - q_0, q_0 = 0.1$	Increasing	4.66×10^{-1}	4.49×10^{-2}	20.2
11	$(q - q_0)^2, q_0 = 0.08$	Increasing	5.15×10^{-1}	5.97×10^{-2}	23.5
12	$(q - q_0)^2, q_0 = 0.1$	Increasing	5.10×10^{-1}	6.56×10^{-2}	23.0

The least squares method is a standard distance metric. On the other hand, the Kullback-Leibler divergence is not symmetrical and both this distance metric and the Bhattacharyya coefficient do not satisfy the triangle inequality, thus they must be considered pre-metrics. The Bhattacharyya coefficient also has an interesting geometrical interpretation, as the cosine of the angle between two multidimensional vectors describing the two distributions. We employ these three methods and order models from lowest to largest distance (or angle), using the $T_{\rm eff}$ and log g distributions for the white dwarf and the spectral type distribution of the M dwarf, from Legacy and BOSS data and also the overall distributions. We do not use SEGUE and SEGUE-2 data due to the small size of the samples. We obtain roughly the same sorting using all three metrics and also set a limit of $\beta > 13^\circ$ above which we consider a model (parameter set) incompatible with observations. In order to exemplify this, in Fig. 6.8 and Fig. 6.9 we show a poor fit and a good fit, respectively. The overall results are shown in an ordered way in Table 6.2. As can be seen, all the models that increase with q can be discarded. Also, in some of the models we vary the minimal mass ratio parameter, q_0, only between 0.08 and 0.1 – the acceptable range according to Ducati et al. (2011) – and find that, in general, $q_0 = 0.08$ performs best.

6.6 Conclusions

We performed a population synthesis study of the WD+MS population of the Galactic disk and compared it to the observed distributions of the white dwarf effective temperature, white dwarf surface gravity and M dwarf spectral type of Rebassa-Mansergas et al. (2016b). We tested 12 models for the IMRD against this data and found that all IMRDs that increase with q can be excluded. This agrees with the results of other studies. In particular, other observational studies have shown that for lower primary masses ($M_1 < 0.3\,M_\odot$) and/or shorter periods (separation $a < 5$ AU), the IMRD is biased towards higher values of q (Biller et al., 2006; Burgasser et al., 2006; Delfosse et al., 2004). However, above this limit (for Solar type, intermediate mass or higher mass stars), main-sequence binaries show an almost flat distribution down to $q \approx 0.1$, occasionally with a marginal peak at $q \sim 0.95 - 1$ (Raghavan et al., 2010; Reggiani & Meyer, 2013; Carquillat & Prieur, 2007; Sana et al., 2012; Duchêne & Kraus, 2013).

We also find that a CE efficiency parameter 0.3 is compatible to the observed data, both in terms of percentage of WD+MS binaries that suffer a common envelope episode and the white dwarf $\log g$ distribution. This is consistent with previous observational (Nebot Gómez-Morán et al., 2011) and theoretical (Camacho et al., 2014) results.

Chapter 7

Conclusions

The goal of this thesis was the study of the white dwarf single and binary populations in the Galactic disk and halo, employing population synthesis methods and taking advantage of the ever growing observational samples of white dwarfs that are currently available owing to modern large scale surveys. All this offered the possibility of analyzing the influence of more subtle aspects of single stellar evolution, like the effect of the stellar metallicity on the disk and halo white dwarf luminosity functions, or the apparent excess of massive white dwarfs in the observed mass function, or to infer constraints on important parameters of binary evolution, such as the common envelope efficiency parameter, or the initial mass ratio distribution.

With this aim in mind, we have improved and updated an existing population synthesis code that can reproduce the white dwarf populations in the context of both single and binary stellar evolution. Our code also includes a Galactic model for the thin and thick disk and the stellar halo. We have incorporated the most recent and up-to-date progenitor evolutionary sequences and white dwarf cooling tracks, computed for different stellar metallicities. To this end, we have updated the interpolation modules of the code, that now can derive accurate values for the properties of the white dwarf interpolating for different progenitor metallicities, masses and ages. This allows us to obtain metallicity-dependent stellar parameters for both main sequence stars and white dwarfs. Additionally, and perhaps more important, we have proceeded in such a way that for each observational sample used as reference, we can study, model and reproduce all the observational filters and biases.

In the following paragraphs we summarize the most important results we have obtained from our studies on the white dwarf populations of the Galactic disk and halo, which were presented in detail in the previous chapters.

In Chapter 3 we performed a study of the role that metallicity plays on the white dwarf luminosity function of the Galactic thin disk, which is often employed as a tool for determining the age of this population. We use a Monte Carlo population synthesis code that models the properties of the Galactic white dwarf population of

the thin disk, employing the most up-to-date evolutionary cooling sequences for white dwarfs with hydrogen-rich and hydrogen-deficient atmospheres, for both carbon-oxygen and oxygen-neon cores. To this aim, we test two different models for the evolution of metallicity. In the first, the adopted metallicity is constant in time, but has a moderate dispersion. In the second model, the metallicity is time dependent, and it is assumed to increase with time.

We obtain that, independently of the adopted age-metallicity law, the simulated white dwarf luminosity function is in very good agreement with the observational luminosity functions derived from the Sloan Digital Sky Survey and from the Super-COSMOS Sky Survey. We find that the age-metallicity relation has no significant impact on the shape of the bright branch of the luminosity function, which implies that it can be safely employed to test theoretical evolutionary sequences. In addition, the position of the cut-off proves to be almost insensitive to the adopted age-metallicity law, ensuring that its location can be used as a robust indicator of the age of the Galactic thin disk.

The dawn of modern large-scale surveys has helped to increase the number of white dwarf identifications up to an order of magnitude. Despite this important advance, the complicated target selection algorithms that these surveys employ make it very difficult to quantify the effects of observational biases. The more recent LAMOST Spectroscopic Survey of the Galactic Anti-center (LSS-GAC) uses a well-defined target selection criteria. This has allowed us to cull a well-characterized magnitude-limited sample of hydrogen-rich (DA) white dwarfs that we used to derive the observed luminosity function, and the mass and cumulative age functions. The latter also allowed us to compute the DA white dwarf formation rate.

We next used our Monte Carlo population synthesis code to simulate the population of single DA white dwarfs in the direction of the Galactic Anti-center, under several sets of assumptions. We applied the LSS-GAC selection criteria over the synthetic populations, also taking into account the observational biases. This procedure allowed us to perform a meaningful comparison between the observed and simulated functions. We found that our simulations of the white dwarf luminosity function are in good agreement with the observed luminosity function, however all the scenarios analyzed so far fail to reproduce the excess of massive white dwarfs identified in the observed mass function. This led us to the conclusion that a certain percentage of massive white dwarfs in our Galaxy could be the product of double degenerate mergers, also implying that the merger rate should be larger than currently estimates. We derived a value of $0.8{\times}10^{-3}$ pc^{-3} for the space density and 5.4×10^{-13} pc^{-3} yr^{-1} for the formation rate of DA white dwarfs.

We also revisited the halo white dwarf luminosity function, using our updated population synthesis code and employing recent and reliable cooling sequences for metal-poor progenitors. By performing an accurate modeling of observational biases, we analyzed the information that can be extracted from the currently available observational sample of halo white dwarfs. Our findings show that the shape of the

hot branch of the halo white dwarf luminosity function is insensitive to different assumptions for the initial mass function and different density profiles for the halo. We also showed that assuming a fraction of unresolved binaries does not produce any noticeable change in the luminosity function, only a slight reduction of the number of white dwarfs in the brightest bins. Given that the cut-off of the observed luminosity function has not yet been determined, we can only place a lower limit of 12.5 Gyr on the age of the halo population.

Due to the reduced size of the current observational sample of halo white dwarfs, we cannot obtain definite conclusions about the effectiveness of the recently computed white dwarf cooling sequences which incorporate residual hydrogen burning. We have, however, shown that the determination for the hot branch of this luminosity function is robust and insensitive to most relevant inputs parameters, thus providing a reliable way of measuring the cooling rate of hot white dwarfs originating from low metallicity progenitors.

We performed as well a population synthesis study of white dwarf-main sequence (WD+MS) binaries in the Galactic disk with the aim of constraining the properties of the initial mass ratio distribution (IMRD) of main sequence binaries, which is a crucial parameter for understanding the evolution of stars in binary systems. We produce a detailed set of Monte Carlo simulations of the WD+MS binary population observed by the SDSS using different initial shapes of the IMRD and taking into account all observational biases.

We showed not only that our simulations reproduce well the observed parameter distributions, but also that we are able to exclude all increasing laws for the IMRD. We also demonstrated that a common envelope efficiently parameter value of $\sim$ 0.3 is compatible with the observed sample of WD+MS binaries, confirming previous findings from the study of post-common envelope binaries.

In short, stellar population synthesis applied to the populations of white dwarfs has proven to be a powerful tool for extracting indirect information about the formation and evolution of stellar populations in our Galaxy. Nevertheless, some of the work described in this thesis was limited by the sample size and it could very well be repeated with presumably better results, once larger samples are made available. This is particularly valid for the sample of white dwarfs from the LSS-GAC, which was based only on the first data release of this survey, that is designed to run for five years in total, and it is also true for the currently available sample of halo white dwarfs, which is expected to increase in future years with the advent of space-born missions such as Gaia.

The code and methods shown in this thesis can also be used for analyzing the double degenerate population in our Galaxy, which is of special interest because they constitute one of the favorite progenitor scenarios for Type Ia supernovae. In this sense, we have ongoing work in computing the delay type distribution for several subpopulations of double degenerate binaries and also the study of common envelope parametrization and other relevant population input parameters needed to correctly

model the population. Among them we mention those that are related to binarity, because they play a key role in the understanding of several current astrophysical problems.

Appendix A

The $1/V_{\rm max}$ method

The Schmidt estimator, also know as the $1/V_{\rm max}$ method, was first suggested by Schmidt (1968), for the study of the space distribution of the quasar population, and later generalized by Felten (1976), who introduced the dependence on the direction of the sample (essential for non-uniformly distributed samples) and also demonstrated that the estimator is unbiased. This method is nowadays widely used for computing the observed white dwarf luminosity function for magnitude and proper motion-limited samples (Liebert et al., 1988, 2005a; Harris et al., 2006; De Gennaro et al., 2008; Hu et al., 2007; Rebassa-Mansergas et al., 2015).

Next we describe our standard procedure for applying the $1/V_{\rm max}$ method for a magnitude and proper motion-limited sample (García-Berro et al., 2004). For each synthetic sample, the maximum and minimum distances over which any star can contribute are:

$$r_{\rm max} = \min\left[\pi^{-1}(\mu/\mu_{\rm min}); \pi^{-1}10^{0.2(m_{\rm max}-m)}\right] \tag{A.1}$$

$$r_{\rm min} = \max\left[\pi^{-1}(\mu/\mu_{\rm max}); \pi^{-1}10^{0.2(m_{\rm min}-m)}\right] \tag{A.2}$$

where: π is the parallax, μ the proper motion, with $\mu_{\rm min}$ and $\mu_{\rm max}$ the lower and upper proper motion limits for the sample, and m the apparent magnitude, with $m_{\rm min}$ and $m_{\rm max}$ the magnitude limits of the sample. Thus, the maximum volume that a star can contribute is:

$$V_{\rm max} = \frac{\Omega}{3}(r^3_{\rm max} - r^3_{\rm min}) \tag{A.3}$$

where Ω is the solid angle covered by the survey.

In the case of the Galactic disk, for which the stars are not spherically distributed, we must implement an additional correction to this relation, $\exp(-z/H)$, where z is the elevation of each star with respect to the Galactic plane and H the specific scale height of the disk. Fleming et al. (1986) showed that assuming different scale heights

has a significant impact only on the hot and more luminous end of the luminosity function.

Every star contributes to the local space density n with $1/V_{\rm max}$:

$$n = \sum_{i=1}^{N_{\rm obj}} \frac{1}{V_{{\rm max}_i}} \tag{A.4}$$

and the effective volume of the sample is then:

$$V_{\rm eff} = \frac{N_{\rm obj}}{n} \tag{A.5}$$

The uncertainty associated with the contribution of each star in the sample is assumed to be equal to the value of the contribution itself (Liebert et al., 1988). The error for every bin of the luminosity function will then be (Boyle, 1989):

$$\sigma = \left[\sum_{i=1}^{n_{\rm bin}} \left(\frac{1}{V_{\rm max_i}} \right)^2 \right]^{1/2} \tag{A.6}$$

Liebert et al. (1988) warn that one should not necessarily expect the overall error to improve with the number of stars per bin, because the partial contribution of a single star to the uncertainty in that bin can be far larger than that of all the other stars, especially if the partial volume contribution of that star is very small, as is the case of nearby stars with small proper motions (Leggett et al., 1998).

Equation 4.1 (used in Chapter 4) offers a more thorough procedure for computing the total maximum volume corresponding to each star as the sum over all the individual maximum volumes obtained from each spectrograph (Hu et al., 2007; Limoges & Bergeron, 2010). This method also takes into account possible overlaps between the observed volumes of two or more spectrographs. In such cases, we only take into account the overlapping region with the largest volume, computed between the smallest lower magnitude limit and the highest upper magnitude limit for the overlapping spectrographs (Liebert et al., 2005a).

The advantages of the $1/V_{\rm max}$ method, that also justify its popularity, mostly reside in the fact that it is a non-parametric and non-biased estimator, that can be applied following a relatively simple procedure, as previously described. For a large enough sample and when observational biases are properly accounted for, the $1/V_{\rm max}$ estimator provides a good characterization of the white dwarf luminosity function, also correctly recovering the position of the cut-off (Geijo et al., 2006). This method also offers a way to measure sample completeness by computing the mean $\langle V/V_{\rm max} \rangle$, dividing the actual volume of the sample by the estimated maximum volume. For a complete sample, we would expect this ratio to be ~ 0.5 (Leggett et al., 1998).

However, a series of potential drawbacks or at least caveats must be taken into account. The method requires the sample to be both complete and homogeneous

(Takeuchi et al., 2000). It is known to underestimate the white dwarf density for moderately high luminosities and it is also sensitive to how data is binned, finer binning giving more reliable results (Geijo et al., 2006). Also, the above described method for assigning error bars tends to underestimate errors for the bright bins down to one order of magnitude and an alternative that uses Poissonian statistics should be considered in order to correct this (Liebert et al., 1988).

As alternatives to using the $1/V_{\max}$ estimator we recall the C^{-} method, the STY method and the Choloniewski method – see Geijo et al. 2006 and Torres et al. 2007 for a comparison and a discussion on their statistical significance, overall effects and inherent biases. As a final note, we emphasize that these authours find that the Choloniewski method in particular, is more robust when dealing with possible sample incompletenesses, performing better than the $1/V_{\max}$ method in recovering the overall density of white dwarfs, but it fails to reproduce the exact location of the cut-off in the white dwarf luminosity function.

Bibliography

Abazajian, K. N., Adelman-McCarthy, J. K., Agüeros, M. A., Allam, S. S., Allende Prieto, C., An, D., Anderson, K. S. J., Anderson, S. F., Annis, J., Bahcall, N. A. & et al., 2009. The Seventh Data Release of the Sloan Digital Sky Survey. *ApJS*, **182**, 543–558.

Adams, W. S., 1915. The Spectrum of the Companion of Sirius. *Pub. Ast. Soc. Pacific*, **27**, 236.

Adelman-McCarthy, J. K., Agüeros, M. A., Allam, S. S., Allende Prieto, C., Anderson, K. S. J. et al., 2008. The Sixth Data Release of the Sloan Digital Sky Survey. *ApJS*, **175**, 297–313.

Ak, T., Bilir, S., Güver, T., Çakmak, H. & Ak, S., 2013. Population types of cataclysmic variables in the solar neighbourhood. *NewA*, **22**, 7–14.

Aller, L. H. & Greenstein, J. L., 1960. The Abundances of the Elements in G-Type Subdwarfs. *ApJS*, **5**, 139.

Althaus, L. G., Camisassa, M. E., Miller Bertolami, M. M., Córsico, A. H. & García-Berro, E., 2015. White dwarf evolutionary sequences for low-metallicity progenitors: The impact of third dredge-up. *A&A*, **576**, A9.

Althaus, L. G., Córsico, A. H., Isern, J. & García-Berro, E., 2010a. Evolutionary and pulsational properties of white dwarf stars. *A&A Rev.*, **18**, 471–566.

Althaus, L. G., García-Berro, E., Isern, J. & Córsico, A. H., 2005a. Mass-radius relations for massive white dwarf stars. *A&A*, **441**, 689–694.

Althaus, L. G., García-Berro, E., Isern, J., Córsico, A. H. & Rohrmann, R. D., 2007. The age and colors of massive white dwarf stars. *A&A*, **465**, 249–255.

Althaus, L. G., García-Berro, E., Renedo, I., Isern, J., Córsico, A. H. & Rohrmann, R. D., 2010b. Evolution of white dwarf stars with high-metallicity progenitors: the role of 22Ne diffusion. *ApJ*, **719**, 612–621.

Althaus, L. G., Miller Bertolami, M. M., Córsico, A. H., García-Berro, E. & Gil-Pons, P., 2005b. The formation of DA white dwarfs with thin hydrogen envelopes. *A&A*, **440**, L1–L4.

Althaus, L. G., Serenelli, A. M. & Benvenuto, O. G., 2001. Diffusion and the occurrence of hydrogen-shell flashes in helium white dwarf stars. *MNRAS*, **323**, 471–483.

Anand, S. P. S., 1968. The Equilibrium Structure of Rapidly Rotating Gaseous Polytropes and Completely Degenerate Systems. *ApJ*, **153**, 135.

Anderson, W., 1929. Gewöhnliche Materie und strahlende Energie als verschiedene #8222Phasen“ eines und desselben Grundstoffes. *Zeitschrift fur Physik*, **54**, 433–444.

Asplund, M., Grevesse, N., Sauval, A. J. & Scott, P., 2009. The Chemical Composition of the Sun. *ARA&A*, **47**, 481–522.

Aznar-Siguán, G., García-Berro, E., Magnien, M. & Lorén-Aguilar, P., 2014. On the possible observational signatures of white dwarf dynamical interactions. *MNRAS*, **443**, 2372–2383.

Baraffe, I., Homeier, D., Allard, F. & Chabrier, G., 2015. New evolutionary models for pre-main sequence and main sequence low-mass stars down to the hydrogen-burning limit. *A&A*, **577**, A42.

Barstow, M. A., Good, S. A., Holberg, J. B., Hubeny, I., Bannister, N. P., Bruhweiler, F. C., Burleigh, M. R. & Napiwotzki, R., 2003. Heavy-element abundance patterns in hot DA white dwarfs. *MNRAS*, **341**, 870–890.

Bastian, N., Covey, K. R. & Meyer, M. R., 2010. A Universal Stellar Initial Mass Function? A Critical Look at Variations. *ARA&A*, **48**, 339–389.

Becker, S. A. & Iben, Jr., I., 1979. The asymptotic giant branch evolution of intermediate-mass stars as a function of mass and composition. I - Through the second dredge-up phase. *ApJ*, **232**, 831–853.

Becker, S. A. & Iben, Jr., I., 1980. The asymptotic giant branch evolution of intermediate-mass stars as a function of mass and composition. II - Through the first major thermal pulse and the consequences of convective dredge-up. *ApJ*, **237**, 111–129.

Bedin, L. R., King, I. R., Anderson, J., Piotto, G., Salaris, M., Cassisi, S. & Serenelli, A., 2008. Reaching the End of the White Dwarf Cooling Sequence in NGC 6791. *ApJ*, **678**, 1279–1291.

Bedin, L. R., Salaris, M., King, I. R., Piotto, G., Anderson, J. & Cassisi, S., 2010. The Bottom of the White Dwarf Cooling Sequence in the Old Open Cluster NGC 2158. *ApJL*, **708**, L32–L35.

Bellini, A., Bedin, L. R., Piotto, G., Salaris, M., Anderson, J. et al., 2010. The end of the white dwarf cooling sequence in M 67. *A&A*, **513**, A50.

Belokurov, V., Zucker, D. B., Evans, N. W., Gilmore, G., Vidrih, S. et al., 2006. The Field of Streams: Sagittarius and Its Siblings. *ApJL*, **642**, L137–L140.

Bensby, T., 2014. Characterisation of the Galactic thick disk. In S. Feltzing, G. Zhao, N. A. Walton & P. Whitelock, eds., *Setting the scene for Gaia and LAMOST*, vol. 298 of *IAU Symposium*, 17–27.

Benvenuto, O. G. & Althaus, L. G., 1997. DB white dwarf evolution in the frame of the full spectrum turbulence theory. *MNRAS*, **288**, 1004–1014.

Benz, W., Ida, S., Alibert, Y., Lin, D. & Mordasini, C., 2014. Planet Population Synthesis. *Protostars and Planets VI*, 691–713.

Bergemann, M., Ruchti, G. R., Serenelli, A., Feltzing, S., Alves-Brito, A. et al., 2014. The Gaia-ESO Survey: radial metallicity gradients and age-metallicity relation of stars in the Milky Way disk. *A&A*, **565**, A89.

Bergeron, P., Ruiz, M. T. & Leggett, S. K., 1997. The Chemical Evolution of Cool White Dwarfs and the Age of the Local Galactic Disk. *ApJS*, **108**, 339–387.

Bergeron, P., Wesemael, F., Dufour, P., Beauchamp, A., Hunter, C., Saffer, R. A., Gianninas, A., Ruiz, M. T., Limoges, M.-M., Dufour, P., Fontaine, G. & Liebert, J., 2011. A Comprehensive Spectroscopic Analysis of DB White Dwarfs. *ApJ*, **737**, 28.

Bessel, F. W., 1844. On the variations of the proper motions of Procyon and Sirius. *MNRAS*, **6**, 136–141.

Biller, B. A., Kasper, M., Close, L. M., Brandner, W. & Kellner, S., 2006. Discovery of a Brown Dwarf Very Close to the Sun: A Methane-rich Brown Dwarf Companion to the Low-Mass Star SCR 1845-6357. *ApJL*, **641**, L141–L144.

Binney, J. & Tremaine, S., 1987. *Galactic dynamics*. Princeton, NJ, Princeton University Press, 1987, 747 p.

Bland-Hawthorn, J. & Gerhard, O., 2016. The Galaxy in Context: Structural, Kinematic, and Integrated Properties. *Annual Review of Astronomy and Astrophysics*, **54**(1), null.

Boyle, B. J., 1989. The space distribution of DA white dwarfs. *MNRAS*, **240**, 533–549.

Bravo, E., Isern, J. & Canal, R., 1993. The contribution of Type IA supernovae to the galactic iron abundances. *A&A*, **270**, 288–296.

Burgasser, A. J., Kirkpatrick, J. D., Cruz, K. L., Reid, I. N., Leggett, S. K., Liebert, J., Burrows, A. & Brown, M. E., 2006. Hubble Space Telescope NICMOS Observations of T Dwarfs: Brown Dwarf Multiplicity and New Probes of the L/T Transition. *ApJS*, **166**, 585–612.

Camacho, J., Torres, S., García-Berro, E., Zorotovic, M., Schreiber, M. R., Rebassa-Mansergas, A., Nebot Gómez-Morán, A. & Gänsicke, B. T., 2014. Monte Carlo simulations of post-common-envelope white dwarf + main sequence binaries: comparison with the SDSS DR7 observed sample. *A&A*, **566**, A86.

Carollo, D., Beers, T. C., Chiba, M., Norris, J. E., Freeman, K. C., Lee, Y. S., Ivezić, Ž., Rockosi, C. M. & Yanny, B., 2010. Structure and Kinematics of the Stellar Halos and Thick Disks of the Milky Way Based on Calibration Stars from Sloan Digital Sky Survey DR7. *ApJ*, **712**, 692–727.

Carquillat, J.-M. & Prieur, J.-L., 2007. Contribution to the search for binaries among Am stars - VIII. New spectroscopic orbits of eight systems and statistical study of a sample of 91 Am stars. *MNRAS*, **380**, 1064–1078.

Carrier, F., North, P., Udry, S. & Babel, J., 2002. Multiplicity among chemically peculiar stars. II. Cool magnetic Ap stars. *A&A*, **394**, 151–169.

Carroll, B. W. & Ostlie, D. A., 2007. *An introduction to modern astrophysics and cosmology*. Pearson Education.

Casagrande, L., Schönrich, R., Asplund, M., Cassisi, S., Ramírez, I., Meléndez, J., Bensby, T. & Feltzing, S., 2011. New constraints on the chemical evolution of the solar neighbourhood and Galactic disc(s). *A&A*, **530**, A138.

Catalán, S., Isern, J., García-Berro, E. & Ribas, I., 2008. The initial-final mass relationship of white dwarfs revisited: effect on the luminosity function and mass distribution. *MNRAS*, **387**, 1693.

Chandrasekhar, S., 1931. The Maximum Mass of Ideal White Dwarfs. *ApJ*, **74**, 81.

Chandrasekhar, S., 1933. The equilibrium of distorted polytropes. I. The rotational problem. *MNRAS*, **93**, 390–406.

Chayer, P., Fontaine, G. & Wesemael, F., 1994. Radiative Levitation in Hot White Dwarfs. In *American Astronomical Society Meeting Abstracts*, vol. 26 of *Bulletin of the American Astronomical Society*, 1383.

Chen, B.-Q., Liu, X.-W., Yuan, H.-B., Zhang, H.-H., Schultheis, M., Jiang, B.-W., Huang, Y., Xiang, M.-S., Zhao, H.-B., Yao, J.-S. & Lu, H., 2014. A three-dimensional extinction map of the Galactic anticentre from multiband photometry. *MNRAS*, **443**, 1192–1210.

Cojocaru, R., Torres, S., Althaus, L. G., Isern, J. & García-Berro, E., 2015. Revisiting the luminosity function of single halo white dwarfs. *A&A*, **581**, A108.

Cojocaru, R., Torres, S., Isern, J. & García-Berro, E., 2014. The effects of metallicity on the Galactic disk population of white dwarfs. *A&A*, **566**, A81.

Cui, X.-Q., Zhao, Y.-H., Chu, Y.-Q., Li, G.-P., Li, Q. et al., 2012. The Large Sky Area Multi-Object Fiber Spectroscopic Telescope (LAMOST). *Research in Astronomy and Astrophysics*, **12**, 1197–1242.

Cummings, J. D., Kalirai, J. S., Tremblay, P.-E. & Ramirez-Ruiz, E., 2016. Two Massive White Dwarfs from NGC 2323 and the Initial-Final Mass Relation for Progenitors of 4 to 6.5 M. *ApJ*, **818**, 84.

Dabbowski, J. P. & Beardsley, W. R., 1977. The Estimation of the Frequency of Binary Stars in Open Cluster s-A Comparison of Methods. *Pub. Ast. Soc. Pacific*, **89**, 225.

Das, U. & Mukhopadhyay, B., 2013. New Mass Limit for White Dwarfs: Super-Chandrasekhar Type Ia Supernova as a New Standard Candle. *Physical Review Letters*, **110**(7), 071102.

Davis, M., Efstathiou, G., Frenk, C. S. & White, S. D. M., 1985. The evolution of large-scale structure in a universe dominated by cold dark matter. *ApJ*, **292**, 371–394.

Davis, P. J., Kolb, U. & Willems, B., 2010. A comprehensive population synthesis study of post-common envelope binaries. *MNRAS*, **403**, 179–195.

Davis, P. J., Kolb, U., Willems, B. & Gänsicke, B. T., 2008. How many cataclysmic variables are crossing the period gap? A test for the disruption of magnetic braking. *MNRAS*, **389**, 1563–1576.

Dawson, K. S., Schlegel, D. J., Ahn, C. P., Anderson, S. F., Aubourg, É. et al., 2013. The Baryon Oscillation Spectroscopic Survey of SDSS-III. *AJ*, **145**, 10.

De Gennaro, S., von Hippel, T., Winget, D. E., Kepler, S. O., Nitta, A., Koester, D. & Althaus, L., 2008. White Dwarf Luminosity and Mass Functions from Sloan Digital Sky Survey Spectra. *AJ*, **135**, 1–9.

Delfosse, X., Beuzit, J.-L., Marchal, L., Bonfils, X., Perrier, C., Ségransan, D., Udry, S., Mayor, M. & Forveille, T., 2004. M dwarfs binaries: Results from accurate radial velocities and high angular resolution observations. In R. W. Hilditch, H. Hensberge & K. Pavlovski, eds., *Spectroscopically and Spatially Resolving the Components of the Close Binary Stars*, vol. 318 of *Astronomical Society of the Pacific Conference Series*, 166–174.

Diaz-Pinto, A., Garcia-Berro, E., Hernanz, M., Isern, J. & Mochkovitch, R., 1994. The luminosity function of massive white dwarfs. *A&A*, **282**, 86–92.

Dreiner, H. K., Fortin, J.-F., Isern, J. & Ubaldi, L., 2013. White dwarfs constrain dark forces. *Phys. Rev. D*, **88**(4).

Ducati, J. R., Penteado, E. M. & Turcati, R., 2011. The mass ratio and initial mass functions in spectroscopic binaries. *A&A*, **525**, A26.

Duchêne, G. & Kraus, A., 2013. Stellar Multiplicity. *ARA&A*, **51**, 269–310.

Dufour, P., Kilic, M., Fontaine, G., Bergeron, P., Lachapelle, F.-R., Kleinman, S. J. & Leggett, S. K., 2010. The Discovery of the Most Metal-rich White Dwarf: Composition of a Tidally Disrupted Extrasolar Dwarf Planet. *ApJ*, **719**, 803–809.

Duran, Ş., Ak, S., Bilir, S., Karaali, S., Ak, T., Bostanci, Z. F. & Coşkunoğlu, B., 2013. Local Stellar Kinematics from RAVE Data: IV. Solar Neighbourhood Age-Metallicity Relation. *Publ. Astron. Soc. Australia*, **30**, 43.

Durisen, R. H., 1975. Upper mass limits for stable rotating white dwarfs. *ApJ*, **199**, 179–183.

Dye, S., Warren, S. J., Hambly, N. C., Cross, N. J. G., Hodgkin, S. T. et al., 2006. The UKIRT Infrared Deep Sky Survey Early Data Release. *MNRAS*, **372**, 1227–1252.

Eddington, A., 1926. *The Internal Constitution of the Stars*. Cambridge University Press.

Eggen, O. J., Lynden-Bell, D. & Sandage, A. R., 1962. Evidence from the motions of old stars that the Galaxy collapsed. *ApJ*, **136**, 748.

Eisenstein, D. J., Liebert, J., Harris, H. C., Kleinman, S. J., Nitta, A., Silvestri, N., Anderson, S. A., Barentine, J. C., Brewington, H. J., Brinkmann, J., Harvanek, M., Krzesiński, J., Neilsen, Jr., E. H., Long, D., Schneider, D. P. & Snedden, S. A., 2006a. A Catalog of Spectroscopically Confirmed White Dwarfs from the Sloan Digital Sky Survey Data Release 4. *ApJS*, **167**, 40–58.

Eisenstein, D. J., Liebert, J., Koester, D., Kleinmann, S. J., Nitta, A., Smith, P. S., Barentine, J. C., Brewington, H. J., Brinkmann, J., Harvanek, M., Krzesiński, J., Neilsen, Jr., E. H., Long, D., Schneider, D. P. & Snedden, S. A., 2006b. Hot DB White Dwarfs from the Sloan Digital Sky Survey. *AJ*, **132**, 676–691.

Farihi, J., Barstow, M. A., Redfield, S., Dufour, P. & Hambly, N. C., 2010. Rocky planetesimals as the origin of metals in DZ stars. *MNRAS*, **404**, 2123–2135.

Felten, J. E., 1976. On Schmidt's Vm estimator and other estimators of luminosity functions. *ApJ*, **207**, 700–709.

Feltzing, S. & Bensby, T., 2009. The age of the Galaxy's thick disk. In E. E. Mamajek, D. R. Soderblom & R. F. G. Wyse, eds., *The Ages of Stars*, vol. 258 of *IAU Symposium*, 23–30.

Ferrario, L., 2012. Constraints on the pairing properties of main-sequence stars from observations of white dwarfs in binary systems. *MNRAS*, **426**, 2500–2506.

Ferrario, L., Wickramasinghe, D., Liebert, J. & Williams, K. A., 2005. The open-cluster initial-final mass relationship and the high-mass tail of the white dwarf distribution. *MNRAS*, **361**, 1131–1135.

Fleming, T. A., Liebert, J. & Green, R. F., 1986. The luminosity function of DA white dwarfs. *ApJ*, **308**, 176–189.

Fontaine, G., Brassard, P. & Bergeron, P., 2001. The Potential of White Dwarf Cosmochronology. *Pub. Ast. Soc. Pacific*, **113**(782), 409–435.

Fowler, R. H., 1926. On dense matter. *MNRAS*, **87**, 114–122.

Frebel, A. & Norris, J. E., 2013. Metal-Poor Stars and the Chemical Enrichment of the Universe. In T. D. Oswalt & G. Gilmore, eds., *Planets, Stars and Stellar Systems. Volume 5: Galactic Structure and Stellar Populations*, 55–144. Springer Netherlands. ISBN 978-94-007-5611-3.

Frew, D. J., 2008. *Planetary Nebulae in the Solar Neighbourhood: Statistics, Distance Scale and Luminosity Function*. Ph.D. thesis, Department of Physics, Macquarie University, NSW 2109, Australia.

Fujimoto, M. Y., 1977. On the Origin of R-Type Carbon Stars: Possibility of Hydrogen Mixing during Helium Flicker. *PASJ*, **29**, 331–350.

Fukugita, M., Ichikawa, T., Gunn, J. E., Doi, M., Shimasaku, K. & Schneider, D. P., 1996. The Sloan Digital Sky Survey Photometric System. *AJ*, **111**, 1748.

García-Berro, E., Torres, S., Isern, J. & Burkert, A., 1999. Monte Carlo simulations of the disc white dwarf population. *MNRAS*, **302**, 173–188.

García-Berro, E., Hernanz, M., Isern, J. & Mochkovitch, R., 1988. Properties of high-density binary mixtures and the age of the universe from white dwarf stars. *Nature*, **333**, 642–644.

Garcia-Berro, E., Hernanz, M., Isern, J. & Mochkovitch, R., 1995. The rate of change of the gravitational constant and the cooling of white dwarfs. *MNRAS*, **277**, 801–810.

Garcia-Berro, E., Isern, J. & Hernanz, M., 1997. The cooling of oxygen-neon white dwarfs. *MNRAS*, **289**, 973–978.

García-Berro, E., Lorén-Aguilar, P., Aznar-Siguán, G., Torres, S., Camacho, J., Althaus, L. G., Córsico, A. H., Külebi, B. & Isern, J., 2012. Double Degenerate Mergers as Progenitors of High-field Magnetic White Dwarfs. *ApJ*, **749**, 25.

García-Berro, E., Lorén-Aguilar, P., Isern, J., Pedemonte, A. G., Guerrero, J. & Lobo, J. A., 2005. Gravitational wave emission from the coalescence of white dwarfs. *Classical and Quantum Gravity*, **22**, S453–S456.

García-Berro, E. & Oswalt, T. D., 2016. The white dwarf luminosity function. *ArXiv e-prints*.

García-Berro, E., Ritossa, C. & Iben, Jr., I., 1997. On the Evolution of Stars that Form Electron-Degenerate Cores Processed by Carbon Burning. III. The Inward Propagation of a Carbon-Burning Flame and Other Properties of a 9 $M_{\odot}$; Model Star. *ApJ*, **485**, 765–784.

García-Berro, E., Torres, S., Althaus, L. G. & Miller Bertolami, M. M., 2014. The white dwarf cooling sequence of 47 Tucanae. *A&A*, **571**, A56.

García-Berro, E., Torres, S., Althaus, L. G., Renedo, I., Lorén-Aguilar, P., Córsico, A. H., Rohrmann, R. D., Salaris, M. & Isern, J., 2010. A white dwarf cooling age of 8 Gyr for NGC 6791 from physical separation processes. *Nature*, **465**, 194–196.

García-Berro, E., Torres, S., Isern, J. & Burkert, A., 2004. Monte Carlo simulations of the halo white dwarf population. *å*, **418**, 53–65.

García-Berro, E., Torres, S., Renedo, I., Camacho, J., Althaus, L. G., Córsico, A. H., Salaris, M. & Isern, J., 2011. The white-dwarf cooling sequence of NGC 6791: a unique tool for stellar evolution. *A&A*, **533**, A31.

Geijo, E. M., Torres, S., Isern, J. & García-Berro, E., 2006. The white dwarf luminosity function - I. Statistical errors and alternatives. *MNRAS*, **369**, 1654–1666.

Gentile Fusillo, N. P., Rebassa-Mansergas, A., Gänsicke, B. T., Liu, X.-W., Ren, J. J., Koester, D., Zhan, Y., Hou, Y., Wang, Y. & Yang, M., 2015. An independent test of the photometric selection of white dwarf candidates using LAMOST DR3. *MNRAS*, **452**, 765–773.

Gesicki, K., Zijlstra, A. A., Hajduk, M. & Szyszka, C., 2014. Accelerated post-AGB evolution, initial-final mass relations, and the star-formation history of the Galactic bulge. *A&A*, **566**, A48.

Giammichele, N., Bergeron, P. & Dufour, P., 2012. Know Your Neighborhood: A Detailed Model Atmosphere Analysis of Nearby White Dwarfs. *ApJS*, **199**, 29.

Gilmore, G. & Reid, N., 1983. New light on faint stars. III - Galactic structure towards the South Pole and the Galactic thick disc. *MNRAS*, **202**, 1025–1047.

Girven, J., Gänsicke, B. T., Steeghs, D. & Koester, D., 2011. DA white dwarfs in Sloan Digital Sky Survey Data Release 7 and a search for infrared excess emission. *MNRAS*, **417**, 1210–1235.

Green, R. F., 1980. The luminosity function of hot white dwarfs. *ApJ*, **238**, 685–698.

Greenstein, J. L., 1971. New Spectroscopic Results on Subluminous Stars, V. In W. J. Luyten, ed., *White Dwarfs*, vol. 42 of *IAU Symposium*, 46.

Gullikson, K., Kraus, A. & Dodson-Robinson, S., 2016. The Close Companion Mass-ratio Distribution of Intermediate-mass Stars. *AJ*, **152**, 40.

Gunn, J. E., Carr, M., Rockosi, C., Sekiguchi, M., Berry, K. et al., 1998. The Sloan Digital Sky Survey Photometric Camera. *AJ*, **116**, 3040–3081.

Gunn, J. E., Siegmund, W. A., Mannery, E. J., Owen, R. E., Hull, C. L. et al., 2006. The 2.5 m Telescope of the Sloan Digital Sky Survey. *AJ*, **131**, 2332–2359.

Hakkila, J., Myers, J. M., Stidham, B. J. & Hartmann, D. H., 1997. A Computerized Model of Large-Scale Visual Interstellar Extinction. *AJ*, **114**, 2043.

Hambly, N. C., MacGillivray, H. T., Read, M. A., Tritton, S. B., Thomson, E. B., Kelly, B. D., Morgan, D. H., Smith, R. E., Driver, S. P., Williamson, J., Parker, Q. A., Hawkins, M. R. S., Williams, P. M. & Lawrence, A., 2001. The SuperCOSMOS Sky Survey - I. Introduction and description. *MNRAS*, **326**, 1279–1294.

Han, Z., 1998. The formation of double degenerates and related objects. *MNRAS*, **296**, 1019–1040.

Han, Z., Podsiadlowski, P. & Eggleton, P. P., 1994. A Possible Criterion for Envelope Ejection in Asymptotic Giant Branch or First Giant Branch Stars. *MNRAS*, **270**, 121.

Han, Z., Podsiadlowski, P. & Eggleton, P. P., 1995. The formation of bipolar planetary nebulae and close white dwarf binaries. *MNRAS*, **272**, 800–820.

Hansen, B. M. S., Brewer, J., Fahlman, G. G., Gibson, B. K., Ibata, R., Limongi, M., Rich, R. M., Richer, H. B., Shara, M. M. & Stetson, P. B., 2002. The White Dwarf Cooling Sequence of the Globular Cluster Messier 4. *ApJL*, **574**, L155–L158.

Hansen, B. M. S., Kalirai, J. S., Anderson, J., Dotter, A., Richer, H. B., Rich, R. M., Shara, M. M., Fahlman, G. G., Hurley, J. R., King, I. R., Reitzel, D. & Stetson, P. B., 2013. An age difference of two billion years between a metal-rich and a metal-poor globular cluster. *Nature*, **500**, 51–53.

Harris, H. C., Munn, J. A., Kilic, M., Liebert, J., Williams, K. A. et al., 2006. The White Dwarf Luminosity Function from Sloan Digital Sky Survey Imaging Data. *AJ*, **131**, 571–581.

Haywood, M., 2008. Radial mixing and the transition between the thick and thin Galactic discs. *MNRAS*, **388**, 1175–1184.

Haywood, M., 2014. Galactic stellar populations: current and new perspectives. In *EAS Publications Series*, vol. 65 of *EAS Publications Series*, 349–407.

Haywood, M., Di Matteo, P., Lehnert, M. D., Katz, D. & Gómez, A., 2013. The age structure of stellar populations in the solar vicinity. Clues of a two-phase formation history of the Milky Way disk. *A&A*, **560**, A109.

Haywood, M., Di Matteo, P., Snaith, O. & Lehnert, M. D., 2015. Clues to the formation of the Milky Way's thick disk. *A&A*, **579**, A5.

Heggie, D. C., 1975. Binary evolution in stellar dynamics. *MNRAS*, **173**, 729–787.

Helmi, A., 2004. Is the dark halo of our Galaxy spherical? *MNRAS*, **351**, 643–648.

Herschel, W., 1785. Catalogue of Double Stars. By William Herschel, Esq. F. R. S. *Philosophical Transactions of the Royal Society of London Series I*, **75**, 40–126.

Herwig, F., Blöcker, T., Langer, N. & Driebe, T., 1999. On the formation of hydrogen-deficient post-AGB stars. *A&A*, **349**, L5–L8.

Holberg, J. B., Barstow, M. A., Bruhweiler, F. C., Cruise, A. M. & Penny, A. J., 1998. Sirius B: A New, More Accurate View. *ApJ*, **497**(2), 935.

Holberg, J. B., Oswalt, T. D. & Sion, E. M., 2002. A Determination of the Local Density of White Dwarf Stars. *ApJ*, **571**, 512–518.

Holberg, J. B., Oswalt, T. D. & Sion, E. M., 2015. The Local Population of White Dwarfs within 25 pc. In *American Astronomical Society Meeting Abstracts*, vol. 225 of *American Astronomical Society Meeting Abstracts*, 343.13.

Holmberg, J. & Flynn, C., 2000. The local density of matter mapped by Hipparcos. *MNRAS*, **313**, 209–216.

Hu, Q., Wu, C. & Wu, X.-B., 2007. The mass and luminosity functions and the formation rate of DA white dwarfs in the Sloan Digital Sky Survey. *A&A*, **466**, 627–639.

Hurley, J. R., Tout, C. A. & Pols, O. R., 2002. Evolution of binary stars and the effect of tides on binary populations. *MNRAS*, **329**, 897–928.

Ibata, R. A., Wyse, R. F. G., Gilmore, G., Irwin, M. J. & Suntzeff, N. B., 1997. The Kinematics, Orbit, and Survival of the Sagittarius Dwarf Spheroidal Galaxy. *AJ*, **113**, 634–655.

Iben, Jr., I., Kaler, J. B., Truran, J. W. & Renzini, A., 1983. On the evolution of those nuclei of planetary nebulae that experience a final helium shell flash. *ApJ*, **264**, 605–612.

Iben, Jr., I. & Livio, M., 1993. Common envelopes in binary star evolution. *Pub. Ast. Soc. Pacific*, **105**, 1373–1406.

Iben, Jr., I., Ritossa, C. & García-Berro, E., 1997. On the Evolution of Stars that Form Electron-degenerate Cores Processed by Carbon Burning. IV. Outward Mixing During the Second Dredge-up Phase and Other Properties of a 10.5 $M_{\odot}$; Model Star. *ApJ*, **489**, 772–790.

Ida, S. & Lin, D. N. C., 2004. Toward a Deterministic Model of Planetary Formation. II. The Formation and Retention of Gas Giant Planets around Stars with a Range of Metallicities. *ApJ*, **616**, 567–572.

Isern, J., García-Berro, E., Domíguez, I., Salaris, M. & Straniero, O., 2005. White Dwarfs and Metal Abundances. In D. Koester & S. Moehler, eds., *14th European Workshop on White Dwarfs*, vol. 334 of *Astronomical Society of the Pacific Conference Series*, 43.

Isern, J., García-Berro, E., Hernanz, M. & Chabrier, G., 2000. The Energetics of Crystallizing White Dwarfs Revisited Again. *ApJ*, **528**, 397–400.

Isern, J., García-Berro, E., Hernanz, M., Mochkovitch, R. & Burkert, A., 1995. The Stellar Formation Rate and the White Dwarf Luminosity Function. In D. Koester & K. Werner, eds., *White Dwarfs*, vol. 443 of *Lecture Notes in Physics, Berlin Springer Verlag*, 19.

Isern, J., García-Berro, E., Hernanz, M., Mochkovitch, R. & Torres, S., 1998. The Halo White Dwarf Population. *ApJ*, **503**, 239.

Isern, J., García-Berro, E., Torres, S. & Catalán, S., 2008. Axions and the Cooling of White Dwarf Stars. *ApJL*, **682**, L109–L112.

Isern, J., Hernanz, M., Mochkovitch, R. & García-Berro, E., 1991. The role of the minor chemical species in the cooling of white dwarfs. *å*, **241**, L29–L32.

Isern, J., Mochkovitch, R., Garcia-Berro, E. & Hernanz, M., 1997. The Physics of Crystallizing White Dwarfs. *ApJ*, **485**, 308.

Ishida, K. & Weinberger, R., 1987. Two senile nearby planetary nebulae and the local PN population. *A&A*, **178**, 227–236.

Ivanova, N., Justham, S., Chen, X., De Marco, O., Fryer, C. L. et al., 2013. Common envelope evolution: where we stand and how we can move forward. *A&A Rev.*, **21**, 59.

Ivezić, Ž., Sesar, B., Jurić, M., Bond, N., Dalcanton, J. et al., 2008. The Milky Way Tomography with SDSS. II. Stellar Metallicity. *ApJ*, **684**, 287–325.

James, F., 1990. A review of pseudorandom number generators. *Computer Physics Communications*, **60**, 329–344.

Jaschek, C. & Ferrer, O., 1972. The Mass Function in Spectroscopic Binaries. *Pub. Ast. Soc. Pacific*, **84**, 292.

Jeffery, E. J., von Hippel, T., DeGennaro, S., van Dyk, D. A., Stein, N. & Jefferys, W. H., 2011. The White Dwarf Age of NGC 2477. *ApJ*, **730**, 35.

Jordi, K., Grebel, E. K. & Ammon, K., 2006. Empirical color transformations between SDSS photometry and other photometric systems. *A&A*, **460**, 339–347.

Jura, M., 2008. Pollution of Single White Dwarfs by Accretion of Many Small Asteroids. *AJ*, **135**, 1785–1792.

Kalirai, J. S., Richer, H. B., Reitzel, D., Hansen, B. M. S., Rich, R. M., Fahlman, G. G., Gibson, B. K. & von Hippel, T., 2005. The Initial-Final Mass Relationship: Spectroscopy of White Dwarfs in NGC 2099 (M37). *ApJL*, **618**, L123–L127.

Kalirai, J. S., Ventura, P., Richer, H. B., Fahlman, G. G., Durrell, P. R., D'Antona, F. & Marconi, G., 2001. The CFHT Open Star Cluster Survey. III. The White Dwarf Cooling Age of the Rich Open Star Cluster NGC 2099 (M37). *AJ*, **122**, 3239–3257.

Kauffmann, G. & Haehnelt, M., 2000. A unified model for the evolution of galaxies and quasars. *MNRAS*, **311**, 576–588.

Kawaler, S. D., 1996. Limits on the Halo White Dwarf Component of Baryonic Dark Matter from the Hubble Deep Field. *ApJL*, **467**, L61.

Kepler, S. O., Kleinman, S. J., Nitta, A., Koester, D., Castanheira, B. G., Giovannini, O., Costa, A. F. M. & Althaus, L., 2007. White dwarf mass distribution in the SDSS. *MNRAS*, **375**, 1315–1324.

Kilic, M., Brown, W. R., Allende Prieto, C., Kenyon, S. J., Heinke, C. O., Agüeros, M. A. & Kleinman, S. J., 2012. The ELM Survey. IV. 24 White Dwarf Merger Systems. *ApJ*, **751**, 141.

Kleinman, S. J., Kepler, S. O., Koester, D., Pelisoli, I., Peçanha, V., Nitta, A., Costa, J. E. S., Krzesinski, J., Dufour, P., Lachapelle, F.-R., Bergeron, P., Yip, C.-W., Harris, H. C., Eisenstein, D. J., Althaus, L. & Córsico, A., 2013. SDSS DR7 White Dwarf Catalog. *ApJS*, **204**, 5.

Koester, D., 2010. White dwarf spectra and atmosphere models . *Memorie della Societa Astronomica Italiana*, **81**, 921–931.

Koester, D., Gänsicke, B. T. & Farihi, J., 2014. The frequency of planetary debris around young white dwarfs. *A&A*, **566**, A34.

Koester, D., Rollenhagen, K., Napiwotzki, R., Voss, B., Christlieb, N., Homeier, D. & Reimers, D., 2005. Metal traces in white dwarfs of the SPY (ESO Supernova Ia Progenitor Survey) sample. *A&A*, **432**, 1025–1032.

Kroupa, P., 1995. Inverse dynamical population synthesis and star formation. *MNRAS*, **277**.

Kroupa, P., 2001. On the variation of the initial mass function. *MNRAS*, **322**, 231–246.

Kroupa, P. & Weidner, C., 2003. Galactic-Field Initial Mass Functions of Massive Stars. *ApJ*, **598**, 1076–1078.

Krzesinski, J., Kleinman, S. J., Nitta, A., Hügelmeyer, S., Dreizler, S., Liebert, J. & Harris, H., 2009. A hot white dwarf luminosity function fromthe Sloan Digital Sky Survey. *å*, **508**, 471–566.

Kudritzki, R. P. & Reimers, D., 1978. On the absolute scale of mass-loss in red giants. II. Circumstellar absorption lines in the spectrum of alpha Sco B and mass-loss of alpha Sco A. *A&A*, **70**, 227–239.

Laughlin, G., Bodenheimer, P. & Adams, F. C., 1997. The End of the Main Sequence. *ApJ*, **482**, 420–432.

Leggett, S. K., Ruiz, M. T. & Bergeron, P., 1998. The Cool White Dwarf Luminosity Function and the Age of the Galactic Disk. *ApJ*, **497**, 294–302.

Liebert, J., Bergeron, P. & Holberg, J. B., 2005a. The Formation Rate and Mass and Luminosity Functions of DA White Dwarfs from the Palomar Green Survey. *ApJS*, **156**, 47–68.

Liebert, J., Dahn, C. C. & Monet, D. G., 1988. The luminosity function of white dwarfs. *ApJ*, **332**, 891–909.

Liebert, J., Dahn, C. C. & Monet, D. G., 1989. The luminosity function of white dwarfs in the local disk and halo. In G. Wegner, ed., *IAU Colloq. 114: White Dwarfs*, vol. 328 of *Lecture Notes in Physics, Berlin Springer Verlag*, 15–23.

Liebert, J., Young, P. A., Arnett, D., Holberg, J. B. & Williams, K. A., 2005b. The Age and Progenitor Mass of Sirius B. *ApJL*, **630**, L69–L72.

Limoges, M.-M. & Bergeron, P., 2010. A Spectroscopic Analysis of White Dwarfs in the Kiso Survey. *ApJ*, **714**, 1037–1051.

Limoges, M.-M., Bergeron, P. & Lépine, S., 2015. Physical Properties of the Current Census of Northern White Dwarfs within 40 pc of the Sun. *ApJS*, **219**, 19.

Liu, C., Li, L., Zhang, F., Zhang, Y., Jiang, D. & Liu, J., 2012. White dwarf-main sequence binaries identified within SDSS DR7 and UKIDSS DR5. *MNRAS*, **424**, 1841–1851.

Liu, X.-W., Yuan, H.-B., Huo, Z.-Y., Deng, L.-C., Hou, J.-L., Zhao, Y.-H., Zhao, G., Shi, J.-R., Luo, A.-L., Xiang, M.-S., Zhang, H.-H., Huang, Y. & Zhang, H.-W., 2014. LSS-GAC - A LAMOST Spectroscopic Survey of the Galactic Anti-center. In S. Feltzing, G. Zhao, N. A. Walton & P. Whitelock, eds., *IAU Symposium*, vol. 298 of *IAU Symposium*, 310–321.

Lorén-Aguilar, P., Guerrero, J., Isern, J., Lobo, J. A. & García-Berro, E., 2005. Gravitational wave radiation from the coalescence of white dwarfs. *MNRAS*, **356**, 627–636.

Luyten, W. J., 1922. Note on Some Faint Early Type Stars with Large Proper Motions. *Pub. Ast. Soc. Pacific*, **34**, 54.

Luyten, W. J., 1950. The search for white dwarfs. *AJ*, **55**, 86.

Maoz, D., Mannucci, F. & Nelemans, G., 2014. Observational Clues to the Progenitors of Type Ia Supernovae. *ARA&A*, **52**, 107–170.

Markovic, D. & Sommer-Larsen, J., 1997. Microlensing, structure of the Galactic halo and determination of the mass function of dark objects. *MNRAS*, **288**, 733–748.

Marsh, M. C., Barstow, M. A., Buckley, D. A., Burleigh, M. R., Holberg, J. B., Koester, D., O'Donoghue, D., Penny, A. J. & Sansom, A. E., 1997. An EUV-selected sample of DA white dwarfs from the ROSAT All-Sky Survey - II. EUV and soft X-ray properties. *MNRAS*, **287**, 705–721.

Marsh, T. R., Dhillon, V. S. & Duck, S. R., 1995. Low-Mass White Dwarfs Need Friends - Five New Double-Degenerate Close Binary Stars. *MNRAS*, **275**, 828.

McCook, G. P. & Sion, E. M., 1999. A Catalog of Spectroscopically Identified White Dwarfs. *ApJS*, **121**, 1–130.

Meng, X., Chen, X. & Han, Z., 2008. Initial-final mass relationship for stars of different metallicities. *A&A*, **487**, 625–635.

Mestel, L., 1952. On the theory of white dwarf stars. I. The energy sources of white dwarfs. *MNRAS*, **112**, 583.

Meusinger, H., Stecklum, B. & Reimann, H.-G., 1991. The age-metallicity-velocity dispersion relation in the solar neighborhood and a simple evolution model. *A&A*, **245**, 57–74.

Mihalas, D. & Binney, J., 1981. *Galactic astronomy: Structure and kinematics*. W. H. Freeman and Co.

Miller Bertolami, M. M., Althaus, L. G. & García-Berro, E., 2013. Quiescent Nuclear Burning in Low-metallicity White Dwarfs. *ApJL*, **775**, L22.

Miller Bertolami, M. M., Althaus, L. G., Serenelli, A. M. & Panei, J. A., 2006. New evolutionary calculations for the born again scenario. *A&A*, **449**, 313–326.

Miyaji, S., Nomoto, K., Yokoi, K. & Sugimoto, D., 1980. Supernova Triggered by Electron Captures. *PASJ*, **32**, 303.

Mochkovitch, R., 1983. Freezing of a carbon-oxygen white dwarf. *A&A*, **122**, 212–218.

Mochkovitch, R., Garcia-Berro, E., Hernanz, M., Isern, J. & Panis, J. F., 1990. Theoretical luminosity functions for halo white dwarfs. *A&A*, **233**, 456–461.

Munn, J. A., Monet, D. G., Levine, S. E., Canzian, B., Pier, J. R., Harris, H. C., Lupton, R. H., Ivezić, Ž., Hindsley, R. B., Hennessy, G. S., Schneider, D. P. & Brinkmann, J., 2004. An Improved Proper-Motion Catalog Combining USNO-B and the Sloan Digital Sky Survey. *AJ*, **127**, 3034–3042.

Navarro, J. F., Frenk, C. S. & White, S. D. M., 1996. The Structure of Cold Dark Matter Halos. *ApJ*, **462**, 563.

Nebot Gómez-Morán, A., Gänsicke, B. T., Schreiber, M. R., Rebassa-Mansergas, A., Schwope, A. D. et al., 2011. Post common envelope binaries from SDSS. XII. The orbital period distribution. *A&A*, **536**, A43.

Nelemans, G., 2013. Galactic Binaries with eLISA. In G. Auger, P. Binétruy & E. Plagnol, eds., *9th LISA Symposium*, vol. 467 of *Astronomical Society of the Pacific Conference Series*, 27.

Noh, H.-R. & Scalo, J., 1990. History of the Milky Way star formation rate from the white dwarf luminosity function. *ApJ*, **352**, 605–614.

Nomoto, K., 1984. Evolution of 8-10 solar mass stars toward electron capture supernovae. I - Formation of electron-degenerate O + NE + MG cores. *ApJ*, **277**, 791–805.

Nordström, B., Mayor, M., Andersen, J., Holmberg, J., Pont, F., Jørgensen, B. R., Olsen, E. H., Udry, S. & Mowlavi, N., 2004. The Geneva-Copenhagen survey of the Solar neighbourhood. Ages, metallicities, and kinematic properties of ∼14 000 F and G dwarfs. *A&A*, **418**, 989–1019.

Ogorodnikov, K. F., 1965. *Dynamics of stellar systems*. Oxford: Pergamon.

Olsen, E. H., 1983. Four-colour UVBY and H-beta photometry of A5 to G0 stars brighter than 8.3 M. *A&AS*, **54**, 55–134.

Oppenheimer, B. R., Hambly, N. C., Digby, A. P., Hodgkin, S. T. & Saumon, D., 2001. Direct Detection of Galactic Halo Dark Matter. *Science*, **292**, 698–702.

Paczynski, B., 1976. Common Envelope Binaries. In P. Eggleton, S. Mitton & J. Whelan, eds., *Structure and Evolution of Close Binary Systems*, vol. 73 of *IAU Symposium*, 75.

Parsons, S. G., Rebassa-Mansergas, A., Schreiber, M. R., Gansicke, B. T., Zorotovic, M. & Ren, J. J., 2016 submitted. The White Dwarf Binary Pathways Survey I: A sample of FGK stars with white dwarf companions. *MNRAS*.

Pauli, E.-M., Napiwotzki, R., Altmann, M., Heber, U., Odenkirchen, M. & Kerber, F., 2003. 3D kinematics of white dwarfs from the SPY project. *A&A*, **400**, 877–890.

Phillips, J. P., 2002. The Distances of Planetary Nebulae: A Scale Based upon Nearby Sources. *ApJS*, **139**, 199–217.

Pickles, A. J., 1998. A Stellar Spectral Flux Library: 1150-25000 Å. *Pub. Ast. Soc. Pacific*, **110**, 863–878.

Pietrinferni, A., Cassisi, S., Salaris, M. & Castelli, F., 2004. A Large Stellar Evolution Database for Population Synthesis Studies. I. Scaled Solar Models and Isochrones. *ApJ*, **612**, 168–190.

Pietrinferni, A., Cassisi, S., Salaris, M. & Castelli, F., 2006. A Large Stellar Evolution Database for Population Synthesis Studies. II. Stellar Models and Isochrones for an α-enhanced Metal Distribution. *ApJ*, **642**, 797–812.

Planck Collaboration, Ade, P. A. R., Aghanim, N., Arnaud, M., Ashdown, M., Aumont, J., Baccigalupi, C., Banday, A. J., Barreiro, R. B., Bartlett, J. G. & et al., in press 2016. Planck 2015 results. XIII. Cosmological parameters. *A&A*.

Poelarends, A. J. T., Herwig, F., Langer, N. & Heger, A., 2008. The Supernova Channel of Super-AGB Stars. *ApJ*, **675**, 614–625.

Pols, O. R., Schröder, K.-P., Hurley, J. R., Tout, C. A. & Eggleton, P. P., 1998. Stellar evolution models for Z = 0.0001 to 0.03. *MNRAS*, **298**, 525–536.

Pourbaix, D., Tokovinin, A. A., Batten, A. H., Fekel, F. C., Hartkopf, W. I., Levato, H., Morrell, N. I., Torres, G. & Udry, S., 2004. S$_{B⁹}$: The ninth catalogue of spectroscopic binary orbits. *A&A*, **424**, 727–732.

Press, W. H., Flannery, B. P. & Teukolsky, S. A., 1986. *Numerical Recipes. The art of scientific computing*. Cambridge: University Press, 1986.

Raghavan, D., McAlister, H. A., Henry, T. J., Latham, D. W., Marcy, G. W., Mason, B. D., Gies, D. R., White, R. J. & ten Brummelaar, T. A., 2010. A Survey of Stellar Families: Multiplicity of Solar-type Stars. *ApJS*, **190**, 1–42.

Rebassa-Mansergas, A., Agurto-Gangas, C., Schreiber, M. R., Gänsicke, B. T. & Koester, D., 2013a. White dwarf main-sequence binaries from SDSS DR 8: unveiling the cool white dwarf population. *MNRAS*, **433**, 3398–3410.

Rebassa-Mansergas, A., Anguiano, B., García-Berro, E., C., F. K., Cojocaru, R., Manser, C. J., Pala, A. F., Gänsicke, B. T. & Liu, X.-W., in press 2016. The age-metallicity relation in the solar neighbourhood from a pilot sample of white dwarf-main sequence binaries. *MNRAS*.

Rebassa-Mansergas, A., Anguiano, B., García-Berro, E., Freeman, K. C., Cojocaru, R., Manser, C. J., Pala, A. F., Gänsicke, B. T. & Liu, X.-W., 2016a. The age-metallicity relation in the solar neighbourhood from a pilot sample of white dwarf-main sequence binaries. *MNRAS*.

Rebassa-Mansergas, A., Gänsicke, B. T., Rodríguez-Gil, P., Schreiber, M. R. & Koester, D., 2007. Post-common-envelope binaries from SDSS - I. 101 white dwarf main-sequence binaries with multiple Sloan Digital Sky Survey spectroscopy. *MNRAS*, **382**, 1377–1393.

Rebassa-Mansergas, A., Gänsicke, B. T., Schreiber, M. R., Koester, D. & Rodríguez-Gil, P., 2010. Post-common envelope binaries from SDSS - VII. A catalogue of white dwarf-main sequence binaries. *MNRAS*, **402**, 620–640.

Rebassa-Mansergas, A., Liu, X.-W., Cojocaru, R., Yuan, H.-B., Torres, S., García-Berro, E., Xiang, M.-X., Huang, Y., Koester, D., Hou, Y., Li, G. & Zhang, Y., 2015. DA white dwarfs from the LSS-GAC survey DR1: the preliminary luminosity and mass functions and formation rate. *MNRAS*, **450**, 743–762.

Rebassa-Mansergas, A., Nebot Gómez-Morán, A., Schreiber, M. R., Gänsicke, B. T., Schwope, A., Gallardo, J. & Koester, D., 2012a. Post-common envelope binaries from SDSS - XIV. The DR7 white dwarf-main-sequence binary catalogue. *MNRAS*, **419**, 806–816.

Rebassa-Mansergas, A., Nebot Gómez-Morán, A., Schreiber, M. R., Girven, J. & Gänsicke, B. T., 2011. Post-common envelope binaries from SDSS-X: the origin of low-mass white dwarfs. *MNRAS*, **413**, 1121–1131.

Rebassa-Mansergas, A., Ren, J. J., Parsons, S. G., Gänsicke, B. T., Schreiber, M. R., García-Berro, E., Liu, X.-W. & Koester, D., 2016b. The SDSS spectroscopic catalogue of white dwarf-main-sequence binaries: new identifications from DR 9-12. *MNRAS*, **458**, 3808–3819.

Rebassa-Mansergas, A., Schreiber, M. R. & Gänsicke, B. T., 2013b. M dwarf companions to white dwarfs - I. Relating magnetic activity, rotation and age. *MNRAS*, **429**, 3570–3577.

Rebassa-Mansergas, A., Zorotovic, M., Schreiber, M. R., Gänsicke, B. T., Southworth, J., Nebot Gómez-Morán, A., Tappert, C., Koester, D., Pyrzas, S., Papadaki, C., Schmidtobreick, L., Schwope, A. & Toloza, O., 2012b. Post-common envelope binaries from SDSS - XVI. Long orbital period systems and the energy budget of common envelope evolution. *MNRAS*, **423**, 320–327.

Reggiani, M. & Meyer, M. R., 2013. Universality of the companion mass-ratio distribution. *A&A*, **553**, A124.

Reid, I. N., 2005. High-Velocity White Dwarfs and Galactic Structure. *ARA&A*, **43**, 247–292.

Ren, J. J., Rebassa-Mansergas, A., Luo, A. L., Zhao, Y. H., Xiang, M. S., Liu, X. W., Zhao, G., Jin, G. & Zhang, Y., 2014. White dwarf-main sequence binaries from LAMOST: the DR1 catalogue. *A&A*, **570**, A107.

Renedo, I., Althaus, L. G., Miller Bertolami, M. M., Romero, A. D., Córsico, A. H., Rohrmann, R. D. & García-Berro, E., 2010. New Cooling Sequences for Old White Dwarfs. *ApJ*, **717**, 183–195.

Renzini, A. & Voli, M., 1981. Advanced evolutionary stages of intermediate-mass stars. I - Evolution of surface compositions. *A&A*, **94**, 175–193.

Richards, G. T., Fan, X., Newberg, H. J., Strauss, M. A., Vanden Berk, D. E. et al., 2002. Spectroscopic Target Selection in the Sloan Digital Sky Survey: The Quasar Sample. *AJ*, **123**, 2945–2975.

Ritossa, C., García-Berro, E. & Iben, Jr., I., 1999. On the Evolution of Stars that Form Electron-degenerate Cores Processed by Carbon Burning. V. Shell Convection Sustained by Helium Burning, Transient Neon Burning, Dredge-out, Urca Cooling, and Other Properties of an 11 M_{solar} Population I Model Star. *ApJ*, **515**, 381–397.

Robin, A. C., Reylé, C., Derrière, S. & Picaud, S., 2003. A synthetic view on structure and evolution of the Milky Way. *A&A*, **409**, 523–540.

Rohrmann, R. D., Althaus, L. G., García-Berro, E., Córsico, A. H. & Miller Bertolami, M. M., 2012. Outer boundary conditions for evolving cool white dwarfs. *A&A*, **546**, A119.

Ross, N. P., Myers, A. D., Sheldon, E. S., Yèche, C., Strauss, M. A. et al., 2012. The SDSS-III Baryon Oscillation Spectroscopic Survey: Quasar Target Selection for Data Release Nine. *ApJS*, **199**, 3.

Rowell, N., 2013. The star formation history of the solar neighbourhood from the white dwarf luminosity function. *MNRAS*, **434**, 1549–1564.

Rowell, N. & Hambly, N. C., 2011. White dwarfs in the SuperCOSMOS Sky Survey: the thin disc, thick disc and spheroid luminosity functions. *MNRAS*, **417**, 93–113.

Russell, H. N., 1914. Relations Between the Spectra and other Characteristics of the Stars. II. Brightness and Spectral Class. *Nature*, **93**, 252–258.

Salaris, M., Althaus, L. G. & García-Berro, E., 2013. Comparison of theoretical white dwarf cooling timescales. *A&A*, **555**, A96.

Salaris, M., Cassisi, S., Pietrinferni, A., Kowalski, P. M. & Isern, J., 2010. A Large Stellar Evolution Database for Population Synthesis Studies. VI. White Dwarf Cooling Sequences. *ApJ*, **716**(2), 1241.

Salpeter, E. E., 1955. The Luminosity Function and Stellar Evolution. *ApJ*, **121**, 161.

Sana, H., de Mink, S. E., de Koter, A., Langer, N., Evans, C. J., Gieles, M., Gosset, E., Izzard, R. G., Le Bouquin, J.-B. & Schneider, F. R. N., 2012. Binary Interaction Dominates the Evolution of Massive Stars. *Science*, **337**, 444.

Schlafly, E. F., Finkbeiner, D. P., Schlegel, D. J., Jurić, M., Ivezić, Ž., Gibson, R. R., Knapp, G. R. & Weaver, B. A., 2010. The Blue Tip of the Stellar Locus: Measuring Reddening with the Sloan Digital Sky Survey. *ApJ*, **725**, 1175–1191.

Schlaufman, K. C., Rockosi, C. M., Allende Prieto, C., Beers, T. C., Bizyaev, D., Brewington, H., Lee, Y. S., Malanushenko, V., Malanushenko, E., Oravetz, D., Pan, K., Simmons, A., Snedden, S. & Yanny, B., 2009. Insight into the Formation of the Milky Way Through Cold Halo Substructure. I. The ECHOS of Milky Way Formation. *ApJ*, **703**, 2177–2204.

Schmidt, M., 1959. The Rate of Star Formation. *ApJ*, **129**, 243.

Schmidt, M., 1968. Space Distribution and Luminosity Functions of Quasi-Stellar Radio Sources. *ApJ*, **151**, 393.

Schmidt, M., 1975. The mass of the galactic halo derived from the luminosity function of high-velocity stars. *ApJ*, **202**, 22–29.

Schönrich, R., Binney, J. & Dehnen, W., 2010. Local kinematics and the local standard of rest. *MNRAS*, **403**, 1829–1833.

Schreiber, M. R., Gänsicke, B. T., Rebassa-Mansergas, A., Nebot Gomez-Moran, A., Southworth, J., Schwope, A. D., Müller, M., Papadaki, C., Pyrzas, S., Rabitz, A., Rodríguez-Gil, P., Schmidtobreick, L., Schwarz, R., Tappert, C., Toloza, O., Vogel, J. & Zorotovic, M., 2010. Post common envelope binaries from SDSS. VIII. Evidence for disrupted magnetic braking. *A&A*, **513**, L7.

Searle, L. & Zinn, R., 1978. Compositions of halo clusters and the formation of the galactic halo. *ApJ*, **225**, 357–379.

Segretain, L., Chabrier, G., Hernanz, M., Garcia-Berro, E., Isern, J. & Mochkovitch, R., 1994. Cooling theory of crystallized white dwarfs. *ApJ*, **434**, 641–651.

Sellwood, J. A. & Binney, J. J., 2002. Radial mixing in galactic discs. *MNRAS*, **336**, 785–796.

Serenelli, A. M., Althaus, L. G., Rohrmann, R. D. & Benvenuto, O. G., 2001. The ages and colours of cool helium-core white dwarf stars. *MNRAS*, **325**, 607–616.

Shaviv, G. & Kovetz, A., 1976. The cooling of carbon-oxygen white dwarfs. *A&A*, **51**, 383–391.

Siess, L., 2007. Evolution of massive AGB stars. II. model properties at non-solar metallicity and the fate of Super-AGB stars. *A&A*, **476**, 893–909.

Sion, E. M., Greenstein, J. L., Landstreet, J. D., Liebert, J., Shipman, H. L. & Wegner, G. A., 1983. A proposed new white dwarf spectral classification system. *ApJ*, **269**, 253–257.

Sion, E. M., Holberg, J. B., Oswalt, T. D., McCook, G. P. & Wasatonic, R., 2009. The White Dwarfs Within 20 Parsecs of the Sun: Kinematics and Statistics. *AJ*, **138**, 1681–1689.

Sion, E. M., Holberg, J. B., Oswalt, T. D., McCook, G. P., Wasatonic, R. & Myszka, J., 2014. The White Dwarfs within 25 pc of the Sun: Kinematics and Spectroscopic Subtypes. *AJ*, **147**, 129.

Strauss, M. A., Weinberg, D. H., Lupton, R. H., Narayanan, V. K., Annis, J. et al., 2002. Spectroscopic Target Selection in the Sloan Digital Sky Survey: The Main Galaxy Sample. *AJ*, **124**, 1810–1824.

Strömgren, B., 1987. An investigation of the relations between age, chemical composition and parameters of velocity distribution based on uvby-beta photometry of F stars within 100 parsec. In G. Gilmore & B. Carswell, eds., *NATO ASIC Proc. 207: The Galaxy*, 229–246.

Suda, T., Komiya, Y., Yamada, S., Katsuta, Y., Aoki, W., Gil-Pons, P., Doherty, C. L., Campbell, S. W., Wood, P. R. & Fujimoto, M. Y., 2013. Transition of the stellar initial mass function explored using binary population synthesis. *MNRAS*, **432**, L46.

Takeuchi, T. T., Yoshikawa, K. & Ishii, T. T., 2000. Tests of Statistical Methods for Estimating Galaxy Luminosity Function and Applications to the Hubble Deep Field. *ApJS*, **129**, 1–31.

Tantalo, R. & Chiosi, C., 2004. Measuring age, metallicity and abundance ratios from absorption-line indices. *MNRAS*, **353**, 917–940.

Tinsley, B. M., 1968. Evolution of the Stars and Gas in Galaxies. *ApJ*, **151**, 547.

Tokovinin, A., 2011. Low-mass Visual Companions to Nearby G-dwarfs. *AJ*, **141**, 52.

Toonen, S. & Nelemans, G., 2013. The effect of common-envelope evolution on the visible population of post-common-envelope binaries. *A&A*, **557**, A87.

Toonen, S., Nelemans, G. & Portegies Zwart, S., 2012. Supernova Type Ia progenitors from merging double white dwarfs. Using a new population synthesis model. *A&A*, **546**, A70.

Torres, S. & García-Berro, E., 2016. The white dwarf population within 40 pc of the Sun. *A&A*, **588**, A35.

Torres, S., García-Berro, E., Althaus, L. G. & Camisassa, M. E., 2015. The white dwarf population of NGC 6397. *A&A*, **581**, A90.

Torres, S., García-Berro, E., Burkert, A. & Isern, J., 2001. The impact of a merger episode in the galactic disc white dwarf population. *Monthly Notices of the Royal Astronomical Society*, **328**, 492–500.

Torres, S., García-Berro, E., Burkert, A. & Isern, J., 2002. High-proper-motion white dwarfs and halo dark matter. *MNRAS*, **336**, 971–978.

Torres, S., García-Berro, E. & Isern, J., 2007. The white dwarf luminosity function - II. The effect of the measurement errors and other biases. *MNRAS*, **378**, 1461–1470.

Torres, S., García-Berro, E., Isern, J. & Figueras, F., 2005. Simulating Gaia performances on white dwarfs. *MNRAS*, **360**, 1381–1392.

Torres, S., García-Berro, E., Krzesinski, J. & Kleinman, S. J., 2014. A population synthesis study of the luminosity function of hot white dwarfs. *A&A*, **563**, A47.

Tout, C. A., Aarseth, S. J., Pols, O. R. & Eggleton, P. P., 1997. Rapid binary star evolution for N-body simulations and population synthesis. *MNRAS*, **291**, 732.

Tremblay, P.-E. & Bergeron, P., 2008. The Ratio of Helium- to Hydrogen-Atmosphere White Dwarfs: Direct Evidence for Convective Mixing. *ApJ*, **672**, 1144–1152.

Tremblay, P.-E., Kalirai, J. S., Soderblom, D. R., Cignoni, M. & Cummings, J., 2014. White Dwarf Cosmochronology in the Solar Neighborhood. *ApJ*, **791**, 92.

Tremblay, P.-E., Ludwig, H.-G., Steffen, M. & Freytag, B., 2013. Spectroscopic analysis of DA white dwarfs with 3D model atmospheres. *A&A*, **559**, A104.

Trimble, V., 1974. On the distribution of binary system mass ratios. *AJ*, **79**, 967.

Twarog, B. A., 1980. The chemical evolution of the solar neighborhood. II - The age-metallicity relation and the history of star formation in the galactic disk. *ApJ*, **242**, 242–259.

van Oirschot, P., Nelemans, G., Toonen, S., Pols, O., Brown, A. G. A., Helmi, A. & Portegies Zwart, S., 2014. Binary white dwarfs in the halo of the Milky Way. *A&A*, **569**, A42.

Vennes, S., 1999. Properties of Hot White Dwarfs in Extreme-Ultraviolet/Soft X-Ray Surveys. *ApJ*, **525**, 995–1008.

Vennes, S., Thejll, P. A., Galvan, R. G. & Dupuis, J., 1997. Hot White Dwarfs in the Extreme Ultraviolet Explorer Survey. II. Mass Distribution, Space Density, and Population Age. *ApJ*, **480**, 714–734.

Verbeek, K., Groot, P. J., Nelemans, G., Scaringi, S., Napiwotzki, R., Drew, J. E., Steeghs, D., Casares, J., Corral-Santana, J. M., Gänsicke, B. T., González-Solares, E., Greimel, R., Heber, U., Irwin, M. J., Knigge, C., Wright, N. J. & Zijlstra, A. A., 2013. A determination of the space density and birth rate of hydrogen-line (DA) white dwarfs in the Galactic plane, based on the UVEX survey. *MNRAS*, **434**, 2727–2741.

Vergely, J.-L., Lançon, A. & Mouhcine, 2002. An inverse method to recover the SFR and reddening properties from spectra of galaxies. *A&A*, **394**, 807–822.

Wallerstein, G., 1962. Motions and Compositions of G Dwarfs. *AJ*, **67**, 123.

Webbink, R. F., 2008. Common Envelope Evolution Redux. In E. F. Milone, D. A. Leahy & D. W. Hobill, eds., *Astrophysics and Space Science Library*, vol. 352 of *Astrophysics and Space Science Library*, 233.

Weidemann, V., 1991. White dwarf space densities and birth rates reconsidered. In G. Vauclair & E. Sion, eds., *NATO ASIC Proc. 336: White Dwarfs*, 67.

Weidemann, V., 2005. On Supermassive White Dwarfs. In D. Koester & S. Moehler, eds., *14th European Workshop on White Dwarfs*, vol. 334 of *Astronomical Society of the Pacific Conference Series*, 15.

Werner, K. & Rauch, T., 2015. Analysis of HST/COS spectra of the bare C-O stellar core ¡ASTROBJ¿H1504+65¡/ASTROBJ¿ and a high-velocity twin in the Galactic halo. *A&A*, **584**, A19.

Willems, B. & Kolb, U., 2004. Detached white dwarf main-sequence star binaries. *A&A*, **419**, 1057–1076.

Williams, K. A., Bolte, M. & Koester, D., 2004. An Empirical Initial-Final Mass Relation from Hot, Massive White Dwarfs in NGC 2168 (M35). *ApJL*, **615**, L49–L52.

Williams, K. A., Bolte, M. & Koester, D., 2009. Probing the Lower Mass Limit for Supernova Progenitors and the High-Mass End of the Initial-Final Mass Relation from White Dwarfs in the Open Cluster M35 (NGC 2168). *ApJ*, **693**, 355–369.

Winget, D. E., Hansen, C. J., Liebert, J., van Horn, H. M., Fontaine, G., Nather, R. E., Kepler, S. O. & Lamb, D. Q., 1987. An independent method for determining the age of the universe. *ApJ*, **315**, L77–L81.

Xu, Y., Deng, L. C. & Hu, J. Y., 2007. The structure of the Galactic halo: SDSS versus SuperCOSMOS. *MNRAS*, **379**, 1373–1389.

Yanny, B., Rockosi, C., Newberg, H. J., Knapp, G. R., Adelman-McCarthy, J. K. et al., 2009. SEGUE: A Spectroscopic Survey of 240,000 Stars with g = 14-20. *AJ*, **137**, 4377–4399.

York, D. G., Adelman, J., Anderson, Jr., J. E., Anderson, S. F., Annis, J. et al., 2000. The Sloan Digital Sky Survey: Technical Summary. *AJ*, **120**, 1579–1587.

Yuan, H. B., Liu, X. W. & Xiang, M. S., 2013. Empirical extinction coefficients for the GALEX, SDSS, 2MASS and WISE passbands. *MNRAS*, **430**, 2188–2199.

Zhao, G., Zhao, Y.-H., Chu, Y.-Q., Jing, Y.-P. & Deng, L.-C., 2012. LAMOST spectral survey – An overview. *Research in Astronomy and Astrophysics*, **12**, 723–734.

Zhao, J. K., Oswalt, T. D., Rudkin, M., Zhao, G. & Chen, Y. Q., 2011. The Chromospheric Activity, Age, Metallicity, and Space Motions of 36 Wide Binaries. *AJ*, **141**, 107.

Zorotovic, M., Schreiber, M. R., Gänsicke, B. T. & Nebot Gómez-Morán, A., 2010. Post-common-envelope binaries from SDSS. IX: Constraining the common-envelope efficiency. *A&A*, **520**, A86.

Zorotovic, M., Schreiber, M. R., Gänsicke, B. T., Rebassa-Mansergas, A., Nebot Gómez-Morán, A., Southworth, J., Schwope, A. D., Pyrzas, S., Rodríguez-Gil, P., Schmidtobreick, L., Schwarz, R., Tappert, C., Toloza, O. & Vogt, N., 2011. Post common envelope binaries from SDSS. XIII. Mass dependencies of the orbital period distribution. *A&A*, **536**, L3.

Zorotovic, M., Schreiber, M. R., García-Berro, E., Camacho, J., Torres, S., Rebassa-Mansergas, A. & Gänsicke, B. T., 2014. Monte Carlo simulations of post-common-envelope white dwarf + main sequence binaries: The effects of including recombination energy. *A&A*, **568**, A68.

Zorotovic, M., Schreiber, M. R., Parsons, S. G., Gänsicke, B. T., Hardy, A., Agurto-Gangas, C., Nebot Gómez-Morán, A., Rebassa-Mansergas, A. & Schwope, A. D., 2016. Detached cataclysmic variables are crossing the orbital period gap. *MNRAS*, **457**, 3867–3877.